

AD A 076124

DDC FILE COPY

6 FLAMEOUT AND ACOUSTIC DAMPING  
IN PULSED CHEMICAL LASERS

9 FINAL TECHNICAL REPORT

10 R. Limpacher

12  
LEVEL H

AVCO EVERETT RESEARCH LABORATORY, INC.

a Subsidiary of Avco Corporation

2385 Revere Beach Parkway

Everett, Massachusetts 02149

11 June 1979

12 149

15 Contract No. N00173-76-C-0162

sponsored by

DEFENSE ADVANCED RESEARCH PROJECTS AGENCY

✓ DARPA Order 3016

and

monitored by

NAVAL RESEARCH LABORATORY

Washington, D. C. 20376

DDC  
RECEIVED  
NOV 5 1979  
A

48450  
79

11 05 095

UNCLASSIFIED

SECURITY CLASSIFICATION OF THIS PAGE (When Data Entered)

REPORT DOCUMENTATION PAGE		READ INSTRUCTIONS BEFORE COMPLETING FORM
1. REPORT NUMBER	2. GOVT ACCESSION NO.	3. RECIPIENT'S CATALOG NUMBER
4. TITLE (and Subtitle) FLAMEOUT AND ACOUSTIC DAMPING IN PULSED CHEMICAL LASERS		5. TYPE OF REPORT & PERIOD COVERED Final Technical Report
		6. PERFORMING ORG. REPORT NUMBER
7. AUTHOR(s) Avco Everett Research Laboratory, Inc.		8. CONTRACT OR GRANT NUMBER(s) N00173-76-C-0162 <sup>NEW</sup>
9. PERFORMING ORGANIZATION NAME AND ADDRESS Avco Everett Research Laboratory, Inc. 2385 Revere Beach Parkway Everett, Massachusetts 02149		10. PROGRAM ELEMENT, PROJECT, TASK AREA & WORK UNIT NUMBERS
11. CONTROLLING OFFICE NAME AND ADDRESS Defense Advanced Research Projects Agency DARPA Order No. 3016		12. REPORT DATE June 1979
		13. NUMBER OF PAGES 145
14. MONITORING AGENCY NAME & ADDRESS (if different from Controlling Office) Naval Research Laboratory Washington, D.C. 20376		15. SECURITY CLASS. (of this report) Unclassified
		15a. DECLASSIFICATION/DOWNGRADING SCHEDULE
16. DISTRIBUTION STATEMENT (of this Report) Approved for public release; distribution unlimited.		
17. DISTRIBUTION STATEMENT (of the abstract entered in Block 20, if different from Report)		
18. SUPPLEMENTARY NOTES		
19. KEY WORDS (Continue on reverse side if necessary and identify by block number) Pulsed Chemical Laser Pulsed DF Laser Laser Acoustics Laser Flameup		
20. ABSTRACT (Continue on reverse side if necessary and identify by block number) The objective of this program was to address the acoustic damping issue of a repetitively-pulsed atmospheric pressure pulsed chemical laser. For this purpose a device, one meter in size parallel to the optical axis, was designed and constructed. To achieve flame-out 80 fluidic devices were used to control the hydrogen flow. A new mixer was fabricated to obtain the required medium quality using a photochemical machining technique. For the acoustic		



UNCLASSIFIED

SECURITY CLASSIFICATION OF THIS PAGE(When Data Entered)

(20)

quieting a heat exchanger was used to reduce the acoustic reflection of the hot-cold gas interfaces, and a muffler type acoustic absorber was constructed for acoustic energy attenuation. The results of a limited test period have been described.

Accession For	
NTIS GRA&I	<input checked="checked" type="checkbox"/>
DDC TAB	<input type="checkbox"/>
Unannounced	<input type="checkbox"/>
Justification	
By	
Distribution/	
Availability Codes	
Dist.	Avail and/or special
A	

UNCLASSIFIED

SECURITY CLASSIFICATION OF THIS PAGE(When Data Entered)

## TABLE OF CONTENTS

<u>Section</u>	<u>Page</u>
List of Illustrations	3
I. INTRODUCTION	7
1. Mixing and Flameout	7
2. Initiation	12
3. Initiation Uniformity	13
4. Acoustic Damping	14
5. Selection of Experimental Scale	14
II. OVERALL DEVICE DESIGN CONSIDERATIONS	17
1. Medium Homogeneity Requirements	17
2. Base Flow Homogeneity Requirements (Ordered)	21
3. Base Flow Homogeneity Requirements (Spatially Disordered)	23
4. Acoustic Damping Requirements	26
III. HEAT EXCHANGER CONCEPT TO REDUCE THE EFFECT OF HOT/COLD GAS INTERFACES	37
1. Low Mach Number Model of Transient Heat Transfer	37
2. Numerical Solution Procedure	40
3. Linearized Heat Exchanger Problem	42
4. Nonlinear Heat Exchanger Results	45
5. Homogeneity Degradation in Laser Cavity Due to the Heat Exchanger	50
6. Blockage and Area Variation Considerations	53
IV. ACOUSTIC SUPPRESSOR CONSIDERATION	57
1. Introduction	57
2. Heat Exchanger Acoustics	58
a. Viscous Interaction	59
b. Shock Attenuation in the Heat Exchanger	61



<u>Section</u>	<u>Page</u>
3. Muffler Acoustics	62
4. Muffler Shock Attenuation	62
a. Muffler Shock Attenuation	63
b. Transverse Gas Expansion in the Muffler	65
5. Muffler Wave Attenuation	67
6. Acoustic Design Summary	70
V. EXPERIMENT DESIGN AND FABRICATION	75
1. Introduction	75
2. Design Consideration	75
3. General Experimental Configuration	76
4. Laser Cavity Size and Configuration	78
5. Fluidics Amplifier Design	80
6. Mixer Design and Fabrication	85
7. Heat Exchanger	92
8. Acoustic Attenuator	99
9. Gas Supply System	100
10. Mixture Initiation	104
11. Gas Scrubbing System	105
12. Control and Timing	110
13. Diagnostics	113
a. Interferometry	113
14. Flameout Diagnostics	116
VI. EXPERIMENTAL RESULTS	121
1. Mixer Flow Tests	121
2. Fluidics Tests	123
3. Flameout Tests	125
4. Acoustic Damping Test	131
VII. CONCLUSION	145

## LIST OF ILLUSTRATIONS

<u>Figure</u>		<u>Page</u>
1	Second and Third Explosion Limits Observed in H <sub>2</sub> :F <sub>2</sub> Laser Mixture	9
2	Small-Scale Fluidic Control Schematic	11
3	Farfield Axial Intensity Degradation (Strehl Ratio) vs Nearfield Phase Front Aberration	18
4	Schematic of Mixing and Flowfield Development	24
5	Cavity Temperature Transient for Constant Volume Combustion	28
6	Schematic of Typical Laser Device Design	29
7	Mollier Diagram for the HF Reaction System	30
8	Acoustic Energy Release for Various HF/DF Reaction Mixtures	32
9	Early Wave History $V_c \approx 36$ m/sec PRF = 60 pps	33
10	Reflection Coefficient for First Reflection from Mixing Plates (Non-Linear Analysis)	34
11	Solution of Heat Exchanger Problem for Small $\Delta T/T_c$	44
12	Effect of Initial Wall Temperature Condition on Pressure at Heat Exchanger Inlet	46
13	Effect of Plate Spacing on Pressure at Heat Exchanger Inlet ( $T_o = 1300$ K)	47
14	Gas Temperature Distribution in Heat Exchanger at End of Interpulse Time (60 pps)	48
15	Density Perturbation at End of Interpulse Time ( $T_o = 1300$ K)	52
16	Schematic of Heat Exchanger Design for Decreased Net Reflection of Compression Waves	55



<u>Figure</u>		<u>Page</u>
17	Tube Axial Variation of Shock Mach Number for Various Open Area Rates	64
18	Notation for Transverse Gas Expansion in the Muffler	66
19	Final Pressure Ratio in the Muffler due to Lateral Gas Expansion as Related to Initial Pressure Ratio and Side Volume Ratio	68
20	Muffler Wall Design	71
21	Acoustic Absorber Performance: Required Admittance = $0.007 \text{ Impedance db } 1.343 [R(1/2) \text{ pc} \cdot 2 (L/H)]$	72
22	Schematic of Basic Experimental Layout	77
23	Schematics of Large Scale Laser	79
24	Master Fluidic Amplifier Design	81
25	Fluidics Control Schematic	83
26	Photograph of Assembled Fluidics Module for Large Scale Device	84
27	Fluidics Tests at 3.3 kHz with Hydrogen	86
28	Photographs of the "A" Type Mixing Plate	88
29	Photograph of the "C" Type Mixing Plate	89
30	Photograph of the "B" Type Mixing Plate	90
31	Front Surface of Mixing Plate Type "A"	91
32	Photograph of 2" Mixing Module Shown Mounted on Test Fixture	93
33	Photograph of Laser Cavity Showing Mixing Module Exit	94
34	Photograph of One Heat Exchanger Module	96
35	Photograph of Heat Exchanger Entrance	97
36	Photograph of Heat Exchanger Exit	98

<u>Figure</u>		<u>Page</u>
37	Schematic of Gas Supply System	102
38	Schematic of Flashlamp Circuit	106
39	Photograph of Spark Gap and Capacitor Housing Components	107
40	Polaroid Trace of Photomultiplier Signal Measuring the Flashlamp Output at a Sweep Rate of 0.5 $\mu$ sec per Division	108
41	Photograph Showing 24 Low Inductance Capacitors and Spark Gaps in Housing Assemblies	109
42	Electrical Schematic of Flashlamp Initiation System	111
43	Automatic Sequencing Panel	112
44	Schematic of Twyman-Green Interferometer	115
45	Schematics of Flame-Out Diagnostics	117
46	X-T Diagram with Flame Standing in the Mixing Module	118
47	X-T Diagram for Flame-Out Condition	119
48	Hot Wire Diagnostics of Mixer	122
49	Schematic of Fluidics Device for Characteristics	124
50	Fluidics Pressure Rise (Fall) vs Time for Discharge (Suction) to a Closed Volume	126
51	Hydrogen Dump Line Pressure vs Time	127
52	Fluorine Absorption Signals Indicating Successful Flame-Out	129
53	Fluorine Absorption Signals Indicating Pre-Ignition	130
54	Oscillograph Record of System Pressures vs Time	132
55	Pressure Transduces Signal with Nitrogen Downstream of Laser Cavity	133
56	Computer Simulation of Cavity Pressure vs Time	134



<u>Figure</u>		<u>Page</u>
57	Pressure Transduces Signal with <u>Helium</u> Downstream of Laser Cavity	136
58	Flow with 8% H <sub>2</sub> , 10% F <sub>2</sub> , 82% He	138
59	Flow Test with He in H <sub>2</sub> Mixture and N <sub>2</sub> in F <sub>2</sub> Mixture	139
60	He in F <sub>2</sub> and H <sub>2</sub> Mix, 40% N <sub>2</sub> , 60% He Mix in Boundary and End Flow (Shows Effect of End Flow/ Main Gas Flow Interface	140
61	Flow with Nearly Index Matched Gases $V \approx 2 \times 10^3$ cm/sec	141
62	Fraction of He Cavity Gas in the H <sub>2</sub> + He Mixture Necessary to Match Index of Refraction of the F <sub>2</sub> + He Mixture	142

## SECTION I

### INTRODUCTION

The advantages of DF wavelengths ( $\sim 3.8 \mu\text{m}$ ) in terms of low atmospheric absorption and smaller mirror diameter as compared to the  $\text{CO}_2$  or CO wavelength is well documented. As a result considerable emphasis has been placed upon cw chemical laser development. However, cw chemical lasers operate at subatmospheric pressures, hence, large chemical pumps or ejector pumps are required. In addition, with the proper selection of laser system parameters the thermal blooming effects encountered with the cw laser do not exist with the pulsed chemical laser. Pulsed damage effects give the pulsed chemical laser a large overall system advantage over the cw chemical and a somewhat smaller advantage over other pulsed lasers.

The basic energy source for the pulsed chemical laser is the chemical energy released as a result of the formation of excited HF/DF molecules. Outside energy is required only to dissociate atomic fluorine from the molecular species, since the chemical reaction proceeds from that point. A reasonably efficient scheme for dissociated molecular fluorine can lead to a high overall laser efficiency. However, the type of initiation is restricted to be scalable to large volumes, to yield a uniformly initiated laser volume, and to be suitable for long run time repetitive operations.

#### 1. MIXING AND FLAMEOUT

The mixture composition of a pulsed chemical laser is selected such that it will be possible to operate at atmospheric pressure. This eliminates the requirements of pumps and allows the exhaust gas to be discharged to the atmosphere through low pressure drop scrubbers. Helium is normally added to the basic  $\text{H}_2(\text{D}_2)$  plus  $\text{F}_2$  mixture to bring the total gas pressure to slightly over 1 atm. Other diluent gases such as argon or nitrogen may be substituted for helium, however this will reduce the laser performance.

The concentration of  $\text{H}_2(\text{D}_2)$  and  $\text{F}_2$  in the laser mixture is determined as a tradeoff including the mass utilization, initiation techniques, initiation level, laser pulse duration and laser energy output density. Mixture compositions containing by volume  $\sim 8\% \text{H}_2(\text{D}_2)$  and 8% to 30% of fluorine are in the range of



interest for high performance. Other trace gases such as  $\text{SF}_6$ ,  $\text{MnF}_6$ ,  $\text{CF}_4$ , etc. have been investigated as additives, either to increase the initiation level (initial F atom concentration) or to aid the kinetics. Partial success has been achieved with such additives to increase both the initiation efficiency and the chemical efficiency at laser energy densities of 10 J/liter or less, however no documented improvement has been recorded at higher laser energy densities. In most cases strongly initiated mixture with additives have yielded a reduction of the laser energy output. The only additive to the basic  $\text{H}_2(\text{D}_2)$ ,  $\text{F}_2$ , He is  $\text{O}_2$  with a typical concentration of  $\text{O}_2/\text{F}_2 \approx 1/25$ . Oxygen is added as a long term mixture stabilizer. This allows the mixture to be stable sufficiently long to be mixed on the "fly" and injected into the active laser region. The operating laser mixture is below the third mixture stability limit and above the second stability limit as shown in Figure 1. Increasing either pressure or temperature or reducing the pressure will spontaneously ignite the mixture, while reducing the temperature will reduce the laser performance. The use of oxygen allows to some degree the shift of the stability limits shown in Figure 1. The nature of the long term laser stability therefore dictates that the principal gases have to be mixed on the "fly" at or near atmospheric pressure. The amount of gas in the mixing region must be minimized since after each laser initiation the 5 atm overpressure optically destroys this gas. It is further experimentally found that any gas containing in excess of 2.5% of  $\text{H}_2$ , with  $\text{F}_2 > \text{H}_2$ , was ignited by such overpressures and could not in the short term be stabilized with additional oxygen.<sup>(1)</sup> Since mixtures of interest contain about 8%  $\text{H}_2(\text{D}_2)$  it is necessary to momentarily turn off either the  $\text{H}_2(\text{D}_2)$  or fluorine. Since the hydrogen mass flow constitutes about 2% of the total laser mass flow it is the obvious choice to be controlled. Turning the hydrogen flow off, while the He and  $\text{F}_2$  flow continues, creates an uncombustible buffer zone between the burned mixture and the incoming laser gas. Furthermore, any hydrogen containing gas in the mixer would be ignited by the overpressure, which would unnecessary cause heating of both the mixer and the downstream located acoustic absorber structure.

To narrow down the type of method for controlling the hydrogen flow, it must be remembered that a good optical medium homogeneity (uniform index of refraction) throughout the laser region is required at the time of initiation. It was determined

1. Final Technical Report "HF:DF Pulsed Chemical Laser", AFWL-TR-75-120, April 1976.

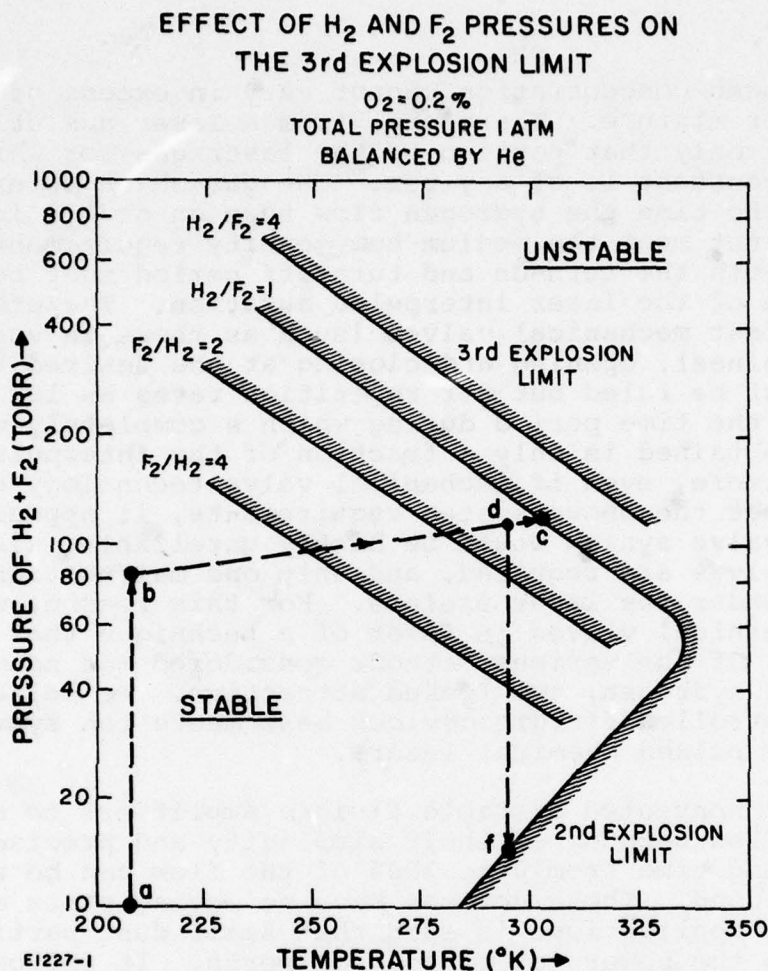


Figure 1

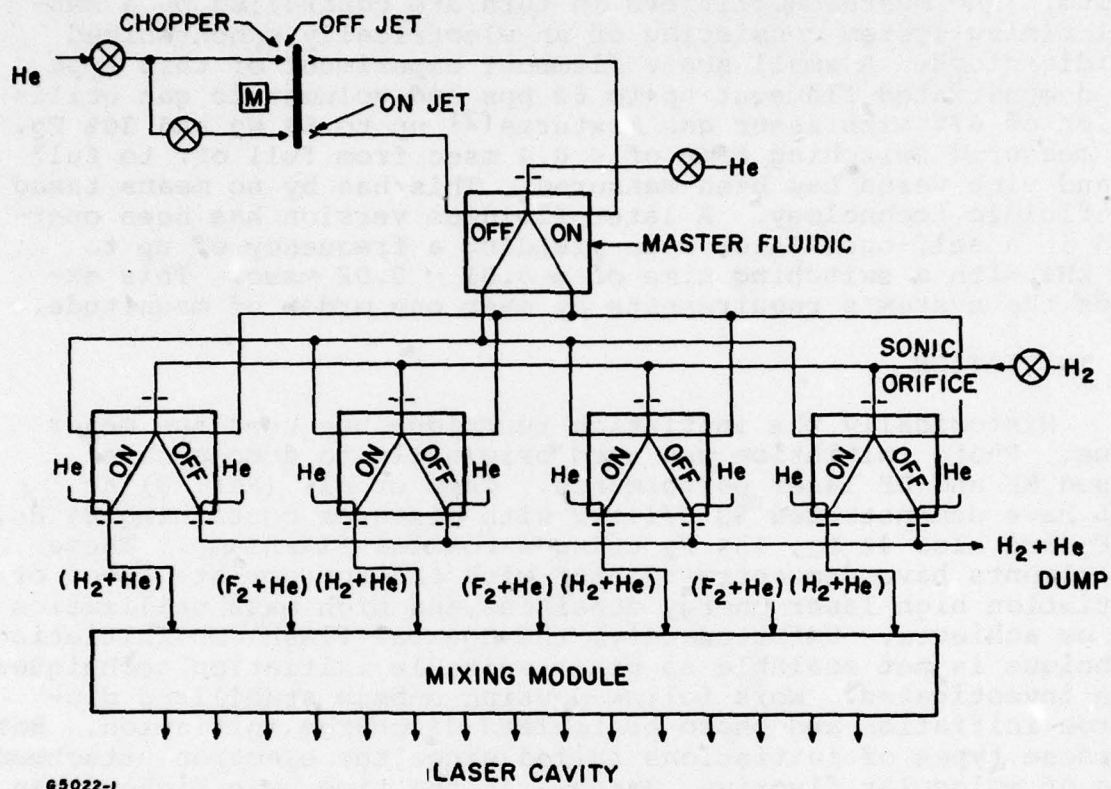
Second and Third Explosion Limits Observed in  $H_2:F_2$  Laser Mixture. The oxygen concentration was kept at 0.5%. The total pressure was 1 atm balanced by He. The reaction vessel was a fully passivated stainless steel 8-liter sphere. For determination of the third explosion limit for  $H_2:F_2$  mixtures of stoichiometric  $H_2:F_2$  ratio, the precooled  $H_2:He$  and  $F_2:O_2:He$  gases were firstly admitted into the vessel of same temperature (shown as line a  $\rightarrow$  b). The vessel was then allowed to ward up slowly until the explosion commenced (b  $\rightarrow$  c). For determination of the second explosion limit, an identical mixture was prepared and warmed up to point d. The reactant was then pumped down to lower pressure until explosion commenced (shown as line d  $\rightarrow$  f).



that the hydrogen concentration cannot vary in excess of 1% of the total laser mixture. Therefore, from a laser gas utilization point of view, only that portion of the laser gas for which the flow rate is constant is of any use. The gas which enters the laser during the time the hydrogen flow turn on or off is useless, since it does not meet the medium homogeneity requirements. It follows that both the turn-on and turn-off period must be a small fraction of the laser interpulse duration. Therefore, it appears that fast mechanical valves (such as those in use for combustion engines), opening and closing at the desired repetition rate, must be ruled out for repetition rates as low as 50 pps, since the time period during which a completely uniform mass flow is obtained is only a fraction of the interpulse duration. Furthermore, even if mechanical valve technology could be improved to meet the above system requirements, it appears that a mechanical valve system would be highly unreliable, since hundreds of valves are required, and only one malfunctioning valve would render the laser useless. For this reason, we abandoned mechanical valves in favor of a technique that has no moving parts. Of the various methods considered for nonmechanical control of hydrogen, two looked attractive. We believe that the use of controlled fluidic devices best meets the system requirements for pulsed chemical lasers.

We chose nonvented bistable fluidic amplifiers to control the hydrogen flow because of their simplicity and precise control. Switching time from 0 to 100% of the flow can be much less than a millisecond. These devices have no moving parts and their size for these applications is such that small dust particles cannot plug up the power jet or control ports. It follows that they should be extremely reliable, while their lifetime should be practically infinite.

The hydrogen flow control is shown schematically in Figure 2 as used in a small scale demonstration experiment. Unvented bistable fluidic amplifiers control the hydrogen flow. When the fluidic amplifiers are on, hydrogen is injected into the mixer, yielding a combustible laser gas composition with 8%  $H_2$ . With the fluidic amplifiers switched to the other bistable position (off) the hydrogen is dumped, yielding an uncombustible gas mixture. The precise hydrogen mass flow of each fluidic device can be controlled independently of the laser cavity pressure with the use of matched sonic orifices, one for each fluidic device. They are located upstream of the hydrogen fluidic power jet. The power jets are usually operated with  $H_2$ . A set of helium orifices is located in the hydrogen on port. The amount of injected helium gas is such that usually a  $H_2:He$  mixture of 16:84 is obtained. This constitutes the hydrogen gas mixture. The fluorine gas mixture of  $F_2:He:O_2$  of equal volumetric flow rate, is continuously injected into the mixer.



65022-1

Figure 2 Small-Scale Fluidic Control Schematic



The master fluidic amplifier(s) are identical in construction to the hydrogen fluidic amplifiers and are operated with helium. The master amplifiers in turn are controlled by a central timing system consisting of an electrically synchronized fluidic clock. A small scale flameout experiment of this type has demonstrated flameout up to 60 pps and volumetric gas utilization of 67% with laser gas mixtures(2) up to 8% H<sub>2</sub> and 30% F<sub>2</sub>. The measured switching time of < 0.4 msec from full off to full on and vice versa has been measured. This has by no means taxed the fluidic technology. A later fluidics version has been operated in a self-oscillator mode yielding a frequency of up to 3.3 kHz with a switching time of  $\approx$  0.01 - 0.02 msec. This exceeds the system's requirements by over one order of magnitude.

## 2. INITIATION

Historically the initiation technique has been the major issue. Photo initiation was used originally to demonstrate pulsed HF and DF laser performance. Chen et al. (Ref. 3) at AERL have demonstrated 80 J/liter with mixtures containing 8% H<sub>2</sub>, 8% F<sub>2</sub> and also 4% H<sub>2</sub>, 16% F<sub>2</sub> using a coaxial flashlamp. These experiments have demonstrated that with the appropriate level of initiation high laser energy densities and high mass utilization can be achieved. Unfortunately, the coaxial flashlamp initiation technique is not scalable so other suitable initiation techniques were investigated. Work followed using e-beam stabilized discharge initiation and photo preionized discharge initiation. Both of these types of initiations failed since the electron attachment rate of molecular fluorine, unknown at the time, was higher than expected. This resulted in ineffective initiation and arcing. Subsequently, straight e-beam initiation using nonstoichiometric mixtures was much more successful. A subsequent experiment using a cold cathode e-beam has demonstrated high volumetric laser efficiency.(4) This type of initiation is scalable to large dimensions and is compatible with all aspects of a high power repetitively pulsed chemical laser. It yielded a laser output of 50 J/liter and an intrinsic electrical efficiency of 900%. Operating with the same conditions a scale up device would yield a wall plug efficiency in the range of 100% to 200%. This high laser output was obtained using a mixture of 8% H<sub>2</sub> and 30% F<sub>2</sub>. For lower fluorine containing mixtures a higher level of initiation is required to yield the same laser output. The efficient nonstoichiometric fluorine rich mixture prompted the assembly with

2. Limpaecher, R. and Woodroffe, J., "Flameout in Repetitively-Pulsed Chemical Lasers," AIAA 15th Aerospace Sciences Meeting, Los Angeles, 24-26, 1977.
3. Wilson, J., Chen, H.L., Taylor, R.L., Fyfe, W., Little, R. and Cowell, R., J. Appl. Phys., 44 5447 (1973).
4. Mangano, J.A., Limpaecher, R., Daugherty, J.D., and Russell, F., "Efficient Electrical Initiation of an H.F. Chemical Laser," Appl. Phys. Letters, 27, 293, (1975).

Internal Research and Development (IRAD) funds of a 32 flashlamp 4 liter photo initiation experiment in a scalable configuration. (5) Although this short term experiment fell about 30% to 40% short of the predicted performance, it yielded the information that such a device could operate at an overall electrical efficiency as high as 50%. The maximum efficiency would be strongly influenced by the maximum tolerance level of the initiations nonuniformity. The interest in the photo initiation stems from the fact that for other programs the repetitively pulsed flashlamp technology was much further advanced than the repetitively pulsed high current e-beam technology. However, the repetitively pulsed e-beam gun technology has recently received significant attention as part of the visible laser program. Therefore, within a year, the selection of the type of initiation will not be determined by the available technology status, but on the basis of performance advantages.

### 3. INITIATION UNIFORMITY

No significant amount of attention has been given to non-uniformity of initiation, since historically the traditional e-beam stabilized CO<sub>2</sub> discharge laser can tolerate large e-beam deposition variations. However, the performance of a pulsed chemical laser can be significantly degraded by initiation non-uniformity, and the tolerable level has not been determined as yet. Indications are that the required initiation nonuniformity must be below 10% throughout the active laser volume.

Nonuniformity of initiation causes nonuniformity of rate of burning. Pulsed chemical laser energy is extracted out of about 20 lines, which do not lase simultaneously but come on during a specific period of the laser mixture combustion period. Gain for a specific line is obtained at different times for different initiation levels. Thus part of the lasing medium may have gain on a specific line, while some other region which is at a different state of burning may have absorption. This degrades laser performance. The degradation of output of a line lasing during the earlier burning period is less than a line turning on during later time, since lower state populations and attendant absorption increase with time. The quantitative effect is not known at this time, since presently existing kinetics codes cannot treat the pulsed chemical laser medium in its non-equilibrium rotational states in sufficient detail to yield an output in agreement with even limited experimental results.

In summary, the initiation technique which will be finally used will most likely be straight e-beam initiation. Since the repetitively pulsed e-beam gun technology is being addressed by

5. Friedman, H.W., Limpacher, R., (unpublished).



the visible laser program, it was therefore AERL's position that the remaining key technical issue of acoustic damping should be addressed next.

#### 4. ACOUSTIC DAMPING

The remaining key technical issue is to establish the minimum time necessary to damp the acoustic disturbances to a level commensurate with good medium homogeneity. This must be performed with an acoustic quieting system constructed out of materials compatible with the corrosive nature of the laser gas mixture which precludes use of materials normally found in repetitively pulsed CO<sub>2</sub> type EDL lasers, such as Humdinger. On the other hand, the strong overpressure, a factor of 3 higher than in the Humdinger laser, means that the task of reducing the strength of the acoustic disturbance to an acceptable level may be more difficult. We have started to address this problem during this contract period.

#### 5. SELECTION OF EXPERIMENTAL SCALE

The questions of selecting the appropriate scale size to demonstrate the acoustic damping technology have been raised in the past year by various parties and justifies some explanation.

During the proposal state, we addressed the question of whether to modify the small scale (4 liter) flameout demonstration apparatus by attaching a downstream acoustic damping system or to construct a new experiment. If a new experiment would be constructed what should its scale and configuration be? The modification of the small scale experiment looked attractive since a minimum of construction time and cost would be involved and modification would be less costly than constructing a new device. However, it was concluded that the information obtained from such a small scale experiment would be of little value to predict the acoustic damping performance of a meaningful large scale device. In addition the data collection would require special time consuming data reduction. During the Humdinger and ABEL flow and acoustic damping development AERL arrived at the same conclusion and a device, one-half of the full size, was constructed for this purpose.

From a data reduction point-of-view it is necessary to resolve 1/10 of one fringe on an optical laser interferogram (in the visible) to determine a density inhomogeneity of  $\delta\rho/\rho \approx 10^{-3}$  in a small scale 10 cm experiment. For such a small acoustics experiment special data reduction is required while for a device with a dimension of 100 cm the interferogram can be analyzed by inspecting the polaroid picture. An adjustment for the next run can be immediately performed and the result analyzed quickly. A second powerful diagnostic used for pulsed EDL lasers is the movie interferogram

with typically 10,000 frames per second or 100 to 150 interferograms per pulse. With this tool the acoustic performance can be diagnosed very effectively, and problems may be isolated immediately if the disturbances are visible.

When analyzing medium homogeneity of a pulsed chemical laser it is necessary to look through two gas shear layers between the end flow and the laser gas regardless of the length of the laser dimension. Experimental data on such shear layers indicate that the disturbance of two shear layers is larger than a tenth of fringe so that the laser medium homogeneity of a tenth of a fringe can only be extracted with great difficulty.

Finally, it is well known in the acoustics state-of-the-art that the longest wavelength (lowest frequency) is the hardest one to attenuate. Experience with the pulsed EDL has shown us that wave components transverse to the flow direction and especially those parallel to optical axis are the hardest to damp. This, specifically, is true for the wave parallel to the optical axis due to its long wavelength, which, in addition, has to refract out of the laser cavity. We concluded that any acoustic damping experiment much less than one meter in dimension parallel to the optical axis would not address the real problem since this major disturbance cannot be duplicated in a small scale device. We, therefore, concluded to construct a larger device one meter in the flow direction which will require a greater effort and cost but ultimately will yield the desired acoustic damping information.



## SECTION II

### OVERALL DEVICE DESIGN CONSIDERATIONS

#### 1. MEDIUM HOMOGENEITY REQUIREMENTS

In order to specify acoustic damping requirements, it is necessary to define the inhomogeneity level of the flowing gaseous medium which can be tolerated. The medium density homogeneity, of course, is first that established in the base flow itself. This is modified by the acoustic disturbances left in the cavity from previous pulsed energy deposition events.

The effect of density inhomogeneities in the laser medium is measured by its influence on the laser farfield irradiance pattern. One measure of this influence is the ratio of the peak laser flux at the center of the laser spot to that achieved if the cavity gas medium were perfectly homogeneous. This ratio is called the Strehl ratio. More precisely, the Strehl ratio  $S$  is defined as the ratio of the farfield axial intensity normalized to the farfield axial intensity for uniform phase and amplitude across the output aperture.

The Strehl ratios  $S$  for ordered (Case I), arbitrary (Case II) and random (Case III) phase aberrations  $\phi(x,y)$  transverse to the optical axis are shown in Figure 3 and are given below<sup>(6)</sup> in the following analytical representations:

Sinusoidal Phase Distribution	Case I: $S = [J_0(\sqrt{2} \phi_{rms})]^2$
Arbitrary Phase Distribution	Case II: $S = 1 - \phi_{rms}^2, \phi_{rms} \ll 1$
Gaussian Probability Distribution	Case III: $S = \exp(-\phi_{rms}^2)$

It is clear that for  $\phi_{rms} \ll 1$ , Cases I and III reduce to Case II.

The number of IR fringes or waves aberration  $F$  is related to the phase aberration  $\phi$  by

$$F(\text{waves}) = \frac{\phi(\text{radians})}{2\pi(\text{radians per wave})} \quad (1)$$

<sup>(6)</sup>M.M. Weiner, Opt, Eng. 13 87 (1974)

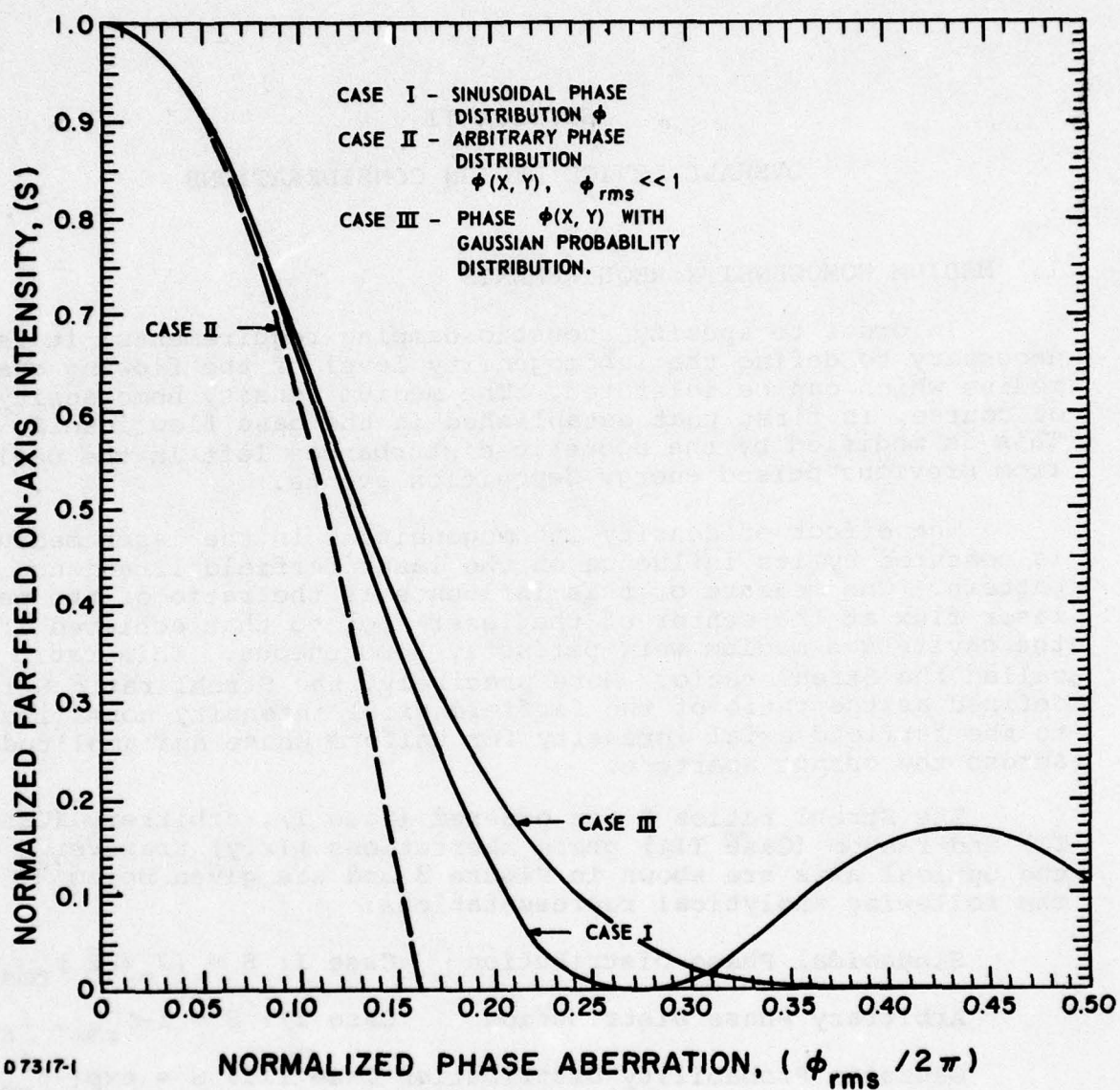


Figure 3 Far Field Axial Intensity Degredation (Strehl Ratio) vs Near Field Phase Front Abberation



The requirement of a Strehl ratio  $S = 0.83$ , in Figure 3, corresponds to an rms aberration  $F_{rms}$  of

$$\text{Case I} \quad F_{rms} = 0.0680$$

$$\text{Case II} \quad F_{rms} = 0.0656$$

$$\text{Case III} \quad F_{rms} = 0.0687$$

Hence, for small phase aberration (i.e., high Strehl ratios) the statistical nature of the phase aberration is of second order in determining the magnitude of allowed phase aberration amplitude. To one significant figure, the medium requirement for a Strehl ratio  $S \geq 0.83$  is  $F_{rms} \leq 0.07$  rms fringes at the wavelength of the IR laser.

The above requirement on requisite phase uniformity is, of course, temporally averaged over the duration of the laser pulse. The total phase aberration would of course be due to three important sources:

- 1) steady or quasi-steady state phase inhomogeneities in the base flow
- 2) residual, decaying, acoustic disturbances from previous pulses
- 3) time-dependent acoustic disturbances induced during the laser pulse itself (e.g., self-focusing)\*

We exclude self-focusing effects by reason of very short laser pulse duration, mixing uniformity and energy deposition uniformity. If we take the steady state inhomogeneity and the decaying acoustic inhomogeneity levels to be comparable, we obtain (for a desired Strehl ratio  $S \approx 0.83$ ) a requirement of

$$F_{total}^2 = F_{steady\ state}^2 + F_{acoustic}^2 = (0.07)^2 \quad (2)$$

$$\text{or} \quad \left( F_{total}^2 / 2 \right)^{1/2}_{rms} \approx F_{individual, rms} \lesssim 0.05 \text{ rms IR fringes}$$

$$\text{or} \quad \phi_{rms} \lesssim 2\pi (0.05) \approx 0.31 \text{ radians} \quad (3)$$

\* Self-focusing or defocusing due to temporal index of refraction changes are very important. This is not considered here since it is critically influenced by the initiation uniformity or scalability of initiation technique.

we now estimate the requirements on the density homogeneity of the medium as imposed by this phase homogeneity requirement.

The phase difference between any two pencil beams traversing the medium is

$$\phi_{1-2} = \frac{2\pi}{\lambda} \int_{\text{path 1}} n(x,y,z) dz - \frac{2\pi}{\lambda} \int_{\text{path 2}} n(x,y,z) dz \quad (4)$$

or, approximately

$$\Delta\phi = \frac{2\pi}{\lambda} \Delta n L \quad (5)$$

where  $n(x,y,z)$  is the spatially variable index of refraction

( $n = 1 + \beta \frac{\rho}{\rho_{\text{ref}}}$ ) and  $L$  is the length of the medium.

This phase difference is generalized to a phase aberration spatially averaged over the laser medium and temporally averaged over the duration of the (short) laser pulse, to yield

spatially ordered disturbance

$$\langle \Delta\phi \rangle = \frac{2\pi}{\lambda} \beta \frac{\rho_{\text{cav}}}{\rho_{\text{ref}}} \frac{1}{2} \left( \frac{\Delta\rho}{\rho} \right)_{\text{p-p}} L_{\text{optical}} \quad (6)$$

spatially random disturbance

$$\langle \Delta\phi_{\text{rms}} \rangle = \frac{2\pi}{\lambda} \beta \frac{\rho_{\text{cav}}}{\rho_{\text{ref}}} \frac{1}{2\sqrt{2}} \left( \frac{\Delta\rho}{\rho} \right)_{\text{p-p}} \sqrt{\Lambda} L_{\text{optical}} \quad (7)$$

where  $\langle \Delta\phi \rangle$  is the spatially and temporally rms averaged phase inhomogeneity,  $\lambda$  is the laser wavelength,  $\beta$  is the Gladstone-Dale constant of the gas mixture in the laser optical path,  $\rho_{\text{cav}}/\rho_{\text{ref}}$  is the gas number density level in the cavity referenced to the number density at 1 atm and 300°K,  $(\Delta\rho/\rho)_{\text{p-p}}$  is the (random or ordered) peak-to-peak gas number density perturbation,  $L_{\text{optical}}$  is the optical path length through the laser medium, and  $\Lambda$  is the outer (largest) scale of the distribution of random density disturbances in the medium. The numerical factors  $(1/2, 1/2\sqrt{2})$  preceding  $(\Delta\rho/\rho)_{\text{p-p}}$  serve to correct the peak-to-peak  $\Delta\rho/\rho$  into the proper form for the phase shift relationships (ordered and random, respectively).



Using  $\beta \approx 10^{-4}$  (typical of a high fluorine and helium content He/F<sub>2</sub>/H<sub>2</sub> mixture) using  $\rho_{\text{cav}}/\rho_{\text{ref}} = 1$ , a laser wavelength of 3  $\mu\text{m}$ , an optical path length of 2 passes (unstable resonator laser optical system) though 100 cm of gain medium, and an outer scale of random disturbance of 1 cm, we obtain, for a Strehl ratio of  $\geq 0.83$

spatially ordered disturbances

$$\left(\frac{\Delta\rho}{\rho}\right)_{P-P_{\text{ordered}}} \leq 1.5 \times 10^{-3} \quad (8)$$

spatially random disturbance

$$\left(\frac{\Delta\rho}{\rho}\right)_{P-P_{\text{random}}} \leq 3 \times 10^{-2} \quad (9)$$

It is clear that randomizing disturbances relieves substantially the requirement of reducing their  $\Delta\rho/\rho$ , and that ordered disturbances must, for an acceptable near field phase distribution, be reduced to the  $10^{-3}$  level.

## 2. BASE FLOW HOMOGENEITY REQUIREMENTS (ORDERED)

As seen above, ordered density inhomogeneities less than  $1.5 \times 10^{-3}$  are required. We now investigate the requirements on the base flowfield such that the steady state flow is optically satisfactory.

Conservation of energy may be written

$$C_p T + \frac{U^2}{2} = \text{constant} \quad (10)$$

or

$$C_p \frac{dT}{T} = - \frac{U^2}{T} \frac{dU}{U} \quad (11)$$

Recalling the definition of the Mach Number  $M = U/\sqrt{\gamma RT}$ , we obtain

$$\frac{dT}{T} = - (\gamma - 1) M^2 \frac{du}{u} \quad (12)$$

For constant pressure variation, the perfect gas law ( $P = \rho RT$ ) yields

$$\frac{dT}{T} = \frac{d\rho}{\rho} \quad \left(\frac{dP}{P} = 0\right) \quad (13)$$

If however, we impose the constraint of having isentropic variation ( $P/\rho^\gamma = \text{CONST}$ ) we then obtain

$$\frac{dT}{T} = (\gamma - 1) \frac{d\rho}{\rho} \quad (14)$$

Hence, for the isentropic flowfield, combining Eqs.(12) and (14) above we obtain

$$\frac{d\rho}{\rho} = -M^2 \frac{du}{u} \quad (15)$$

Therefore, for a requisite ordered density homogeneity across the flowfield of  $10^{-3}$  at a Mach number of 0.1, we require a flowfield velocity homogeneity of  $10^{-1}$  or a 10% variation about the mean cavity velocity. This level of homogeneity, then requires good engineering design of the cavity and the gas flow feed into the optical cavity, with perhaps a separation of the end of the mixing plates from the entrance to the optical cavity. As seen from Eq. (15), the cavity Mach number places severe restrictions on flowfield velocity uniformity.

However, since the Mach number of the present system is of the order of 0.1 or less, no major density perturbations are foreseen due to large scale velocity inhomogeneities in the bulk mean flow. However, for larger devices or higher repetition rates the velocity inhomogeneities may be an issue.



### 3. BASE FLOW HOMOGENEITY REQUIREMENTS (SPATIALLY DISORDERED)

Figure 4 shows a sketch of the flow pattern and mixing plate configuration of the present design. It is the purpose of this section to analyze the flow downstream of the ends of the mixing plates to determine the levels of spatially disordered density inhomogeneities which can influence the optical quality of the medium.

As shown in Eq. (4), the rms phase aberration can be written as

$$\Delta\phi_{\text{rms}} = \frac{2\pi}{\lambda} \int_{\text{path 1}} n \, dz - \frac{2\pi}{\lambda} \int_{\text{path 2}} n \, dz \quad (16)$$

which, for spatially disordered index differences can be written as

$$\Delta\phi_{\text{rms}} = \frac{2\pi}{\lambda} \Delta n \sqrt{\Lambda L} \quad (17)$$

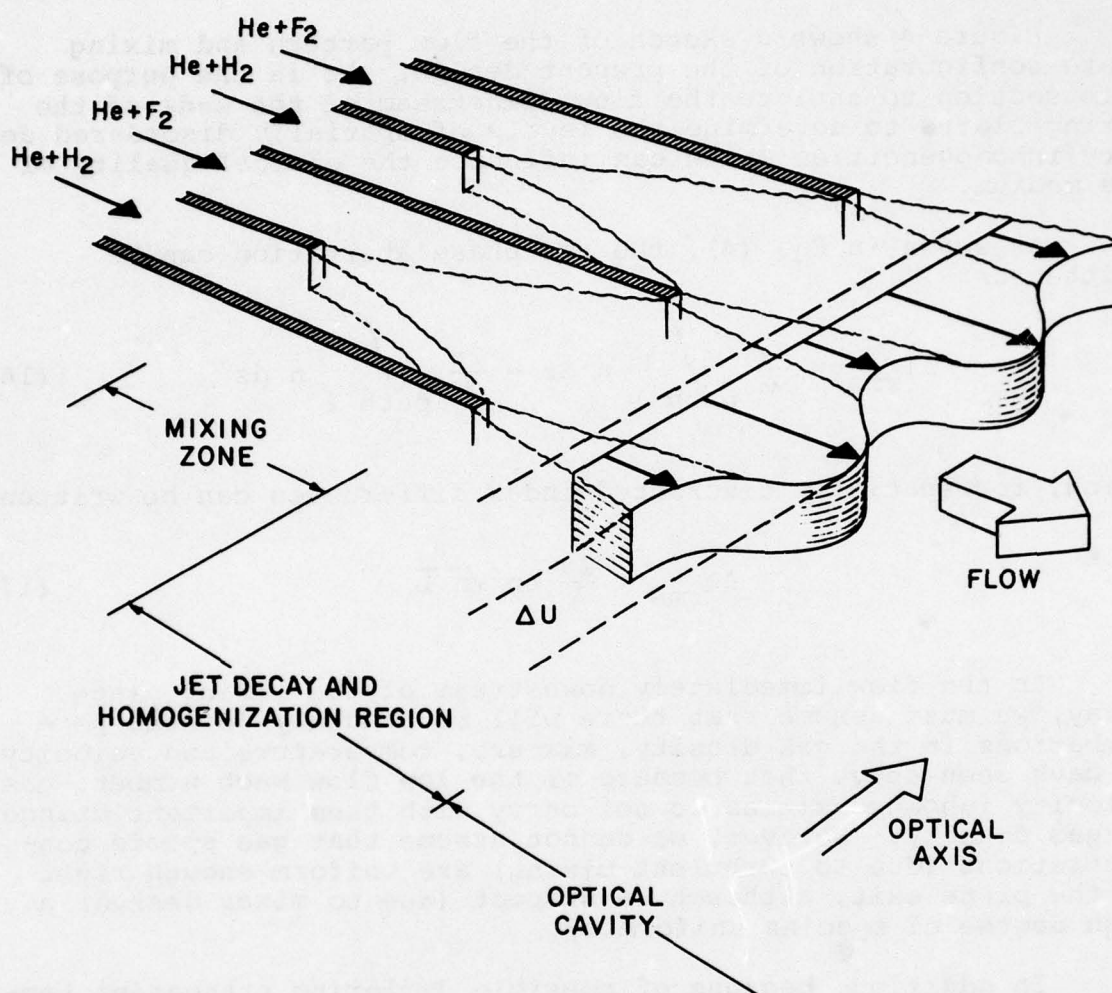
In the flow immediately downstream of the mixing plate array, we must assume that there will be randomly located perturbations in the gas density, mixture, temperature and velocity. We have seen above that because of the low flow Mach number, gas velocity inhomogeneities do not carry with them important changes in gas density. However, we cannot assume that gas specie concentrations (due to turbulent mixing) are uniform enough right at the plate exit, although we suspect (due to mixer design) a high degree of species uniformity.

In addition, because of possible differing stagnation temperature conditions and wall heat transfer, we cannot assume homogeneous density and temperature levels at the end of the mixer plates.

We therefore must estimate the levels of these possible inhomogeneities which could influence optical phase degradation in the laser medium.

A more general expression for Eq. (17) in this jet decay and flow homogenization region is

$$\Delta\phi_{\text{rms}} = \frac{2\pi}{\lambda} \bar{\beta} \frac{\rho_{\text{cav}}}{\rho_{\text{ref}}} \frac{1}{2\sqrt{2}} \left[ \left( \frac{\Delta\rho}{\rho} \right)^2 + \left( \frac{\Delta\beta}{\beta} \right)^2 + 2 \left( \frac{\Delta\beta}{\beta} \right) \left( \frac{\Delta\rho}{\rho} \right) \right]^{1/2} \sqrt{\Lambda L} \quad (18)$$



H8890

Figure 4 Schematic of Mixing and Flowfield Development



Since  $\Delta\rho/\rho$  in this region reflects the differences in the gas temperature exiting from adjacent mixing plate regions, and  $\Delta\beta/\beta$  reflects difference in the mixing achieved by two adjacent mixing plates, we assume that  $|\Delta\rho/\rho| = |\Delta\beta/\beta|$ . We conservatively take the scale size  $\Lambda$  as that of the center-to-center distance of the final mixing channels. Hence  $\Lambda \equiv 1/16$  inch  $\approx$

Defining  $\Delta x/x \equiv \left| \frac{\Delta\rho}{\rho} \right| = \left| \frac{\Delta\beta}{\beta} \right|$ , we see

$$\left| \frac{\Delta x}{x} \right|_{p-p} = \frac{(\Delta\phi_{rms}) \text{ req'd}}{2 \frac{2\pi}{\lambda} \bar{\beta} \frac{\rho_{cav}}{\rho_{ref}} \frac{1}{2\sqrt{2}} \sqrt{\Lambda L_{opt}}} \quad (19)$$

Using (as above)  $\lambda = 3 \mu\text{m}$ ,  $\bar{\beta} = 10^{-4}$ ,  $\rho_{cav}/\rho_{ref} = 1$ ,  $\Delta\phi_{rms} = 0.31$ ,  $\Lambda = 1/16$  inch = 0.16 cm,  $L_{opt} = 200$  cm, we obtain

$$\left| \frac{\Delta\rho}{\rho} \right|, \left| \frac{\Delta\beta}{\beta} \right| \leq 0.04 \text{ peak-to-peak}$$

The remaining random density and species mixing nonuniformities existing at the end of the mixing plates must be allowed to further decay to an approximately  $< 4\%$  nonuniformity level in order to support a near-diffraction-limited laser beam in the optical cavity section.

The decay of grid turbulence was used to model this decay and the additional mixing. As shown in Figure 4 the two-dimensional turbulent jets issue into the main cavity volume, downstream of the end of the mixing module. Within approximately 10 jet center-to-center distances, the major velocity profiles issuing from the mixers will smooth, leaving little shear to generate further turbulence.

With no major source of further turbulent energy, dissipation of the inhomogeneities will proceed in a fashion we expect to be close to that observed in a grid-generated turbulent flow-field. Here the fluctuating turbulent energy  $(\omega')^2$  decays relative to the bulk flow kinetic energy  $U^2$  according to a universal form

$$\left( \frac{\omega'}{U} \right)^2 \approx \frac{1}{100 \left( \frac{x}{D} - 10 \right)} \quad (20)$$

where  $x/D$  is the distance downstream of the turbulence grid normalized by the spacing between the grid elements.

In this flowfield the turbulent kinetic energy  $(\omega')^2$  is a passive scalar, acting virtually identically to density, temperature and species inhomogeneities. Hence, we expect, at  $x/D > 100$

$$\frac{u'}{v}, \frac{\delta(\Delta\rho)}{(\Delta\rho)}, \frac{\delta(\Delta\beta)}{(\Delta\beta)} \leq 10^{-2} \quad (21)$$

where  $(\Delta\rho)$  and  $\Delta\beta$  are the remaining density and species inhomogeneities at the exit of the mixer. Should large amplitude density and mixture inhomogeneities exist between adjacent mixing plate flows, we expect close to an optically acceptable flowfield at a downstream distance which is small compared to the laser cavity dimension. This, of course, must be checked experimentally, with considerable attention paid to mixture homogenization within each mixer channel, and downstream of the mixer exit.

It must be further pointed out that from a practical point-of-view the species inhomogeneities after the  $10 x/D$  turbulent energy decay must be of the order of  $10^{-2}$  or better. Should it not be the case, the continued mixing in the laser cavity will result in a burning rate which will be a function of the distance referenced to the mixer exit. It follows that the mixer must be designed so that most of the mixing is accomplished by the time the gas exits the mixer. The type of mixer selected allows a fabrication technique where the distance  $D$  can be eventually reduced to dimensions of the order of 0.25 mm or less. This will not only reduce the distance from the mixer exit to the laser cavity to a value much less than a centimeter, but also selects a mixing technique which is compatible with the overall requirements of the pulsed chemical laser system. The type of mixer will be described in the design section.

#### 4. ACOUSTIC DAMPING REQUIREMENTS

We have discussed above the flowfield homogeneity requirements for an optically acceptable laser medium at the laser wavelength.

For the first pulse, we expect therefore an output laser beam having a high degree of transverse phase homogeneity. However, the overpressure produced by the first chemical reaction in the optical region generates shock waves which rapidly disrupt this high quality flowfield. We must re-establish this flowfield before the next laser pulse.



Figure 5 indicates the pressure or temperature history of the detonated gas mixture, assuming constant volume processes. The peak pressure and temperatures reached in the pulse are 5.25 atm and 1576°K, with equilibrium values achieved in some 10  $\mu$ sec at levels of 4.38 atm and 1315°K. The drop in pressure and temperature from peak to equilibrium values is due to the production of dissociated Fluorine (F) atoms and HF (molecular) reaction products.

Needless to say, the materials and construction of the device must be compatible with these reaction products, their temperature, pressures, and flow velocities.

The resultant wave system generated by this detonation is complex, and of high acoustic intensity. We are required to rapidly re-establish the optical homogeneity of the bulk flow in a time scale consistent with transporting the combusted gas mixture out of the cavity and refilling it with a fresh combustible gas mixture.

The goal of the effort in both acoustics and flow is to accomplish the above so as to produce a near-diffraction limited pulsed chemical laser output with a pulse repetition frequency (PRF) of 60-100 PPS and with a minimum waste of flowing unburned gas between pulses.

To this end, we must now consider the physical configuration of the laser cavity, its upstream flow source and its downstream flow paths. Figure 6 shows a sketch of a typical laser device design. As a result of a combustion event (and its consequent laser output) the hot gas will rapidly expand to approximately 3 times its volume depending on the laser gas mixture. This expanded gas will be transported downstream at a velocity consistent with the cavity mass flow, geometry and fluid equilibrium gas density. However, the acoustic waves generated by the initial high overpressures will continue to reverberate throughout the cavity, through the just-combusted gas as well as the gas from previous combustion events located in the downstream sections.

The acoustic energy release will strongly depend on the gas composite. The process can be conveniently expressed utilizing a Mollier diagram - a diagram illustrating equilibrium thermodynamic states - with the enthalpy and entropy as coordinates. In Figure 7 we exhibit such a diagram schematically. The ideal gas law is not applicable since the ratio of the specific heats  $\gamma$  changes typically from 1.5 for a nonreacted gas to 1.3 for a reacted gas due to the thermal dissociation of fluorine.

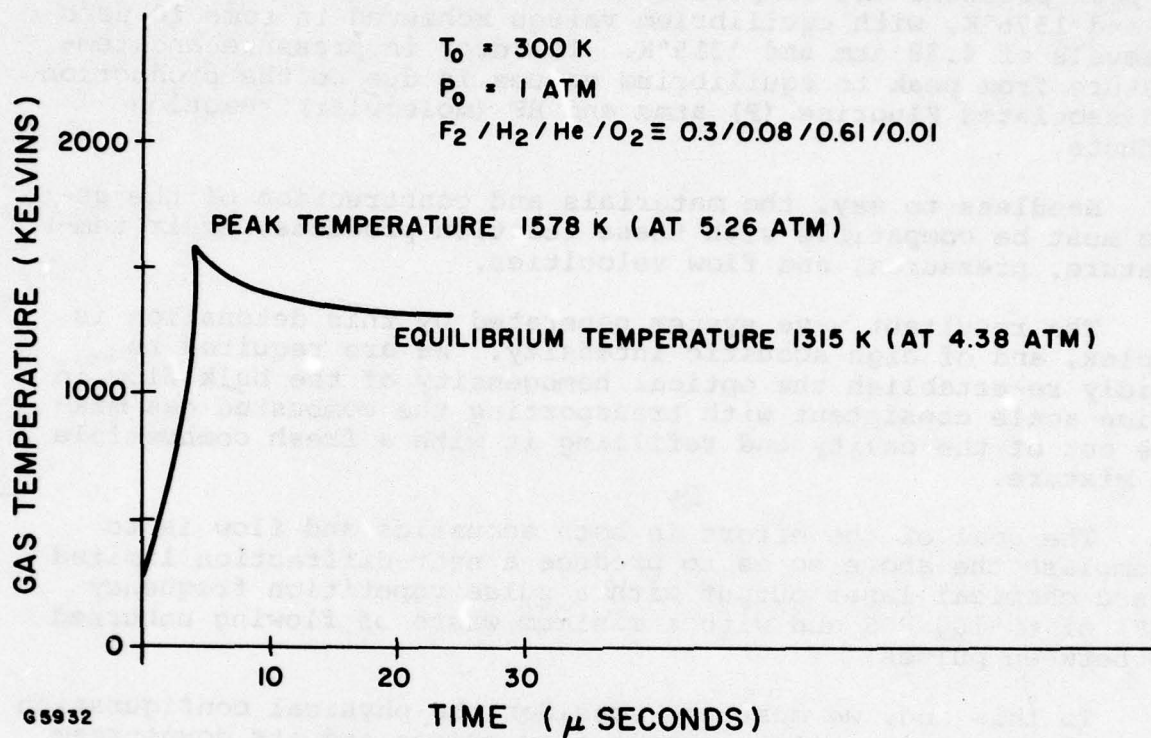


Figure 5 Cavity Temperature Transient for Constant Volume Combustion



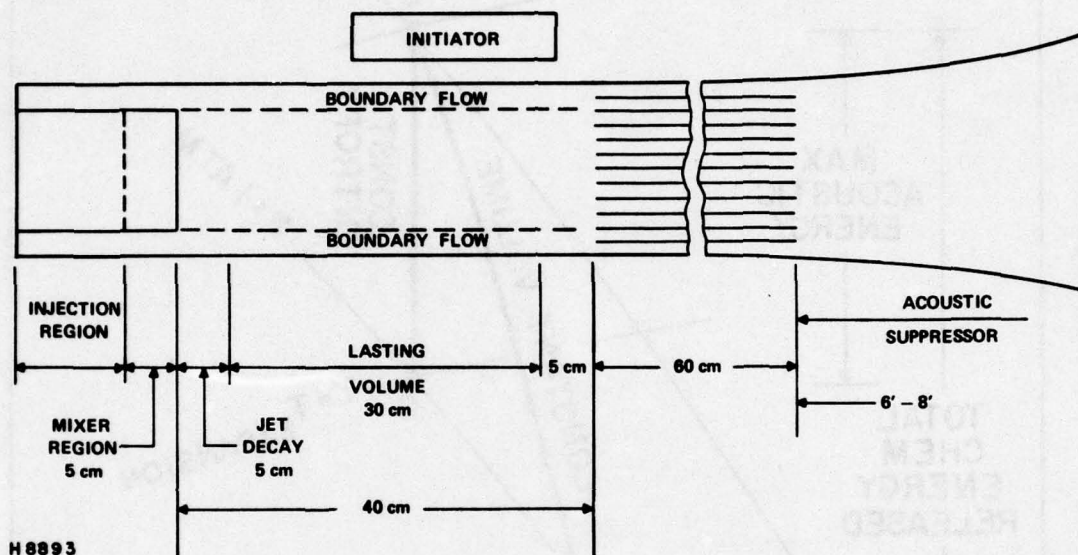
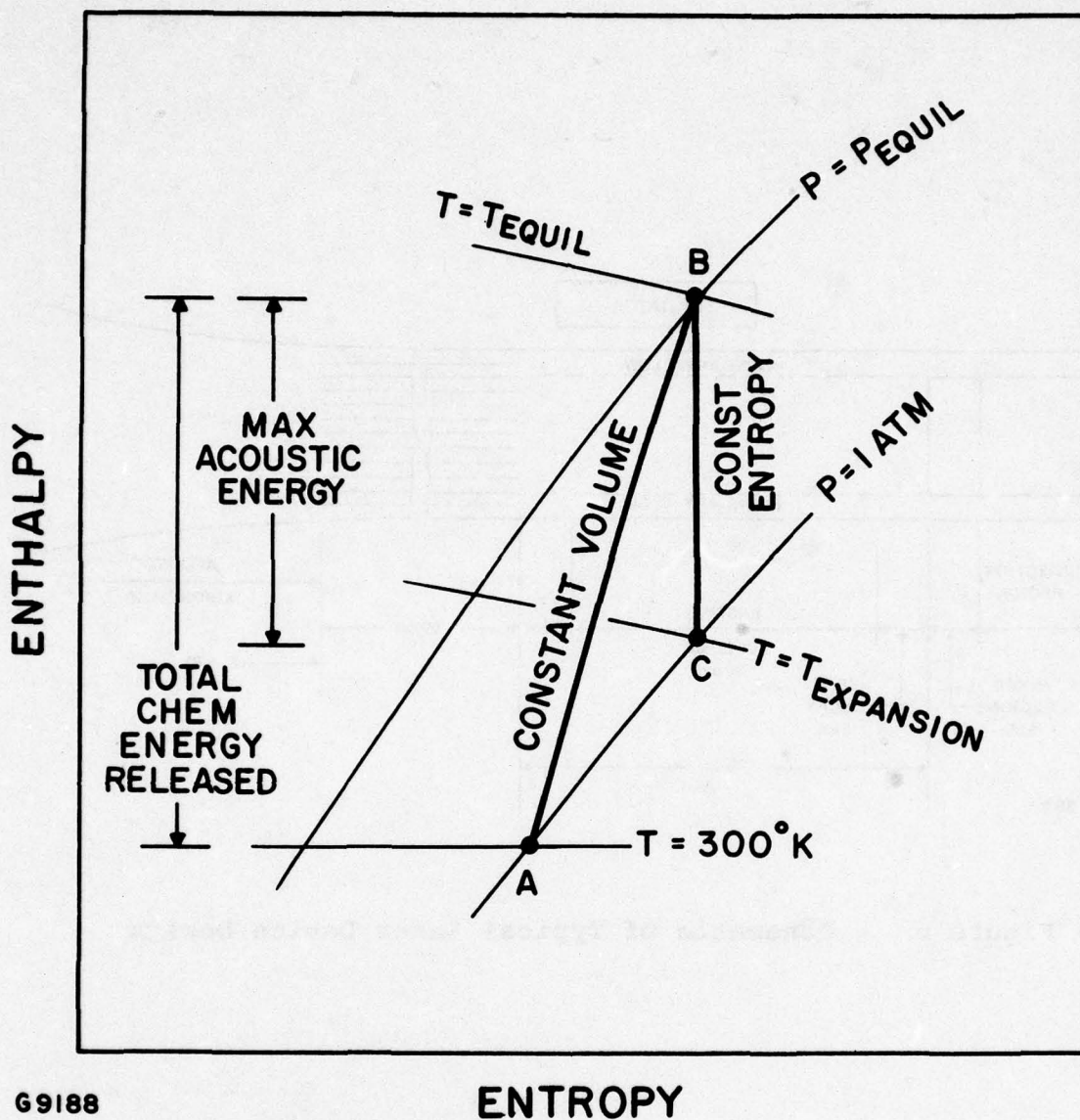


Figure 6 Schematic of Typical Laser Device Design



G9188

Figure 7 Mollier Diagram for the HF Reaction System



The variation of acoustic energy release among the gas mixes considered for HF/DF lasers are summarized in Figure 8. The acoustic energy is greatest for the stoichiometric gas mixture. The acoustic energy levels indicated are three times those for the ABEL device and is 550 J/liter for the 20% F<sub>2</sub>, 8% H<sub>2</sub> mixture. The acoustic energy in combination with the necessary acoustic attenuation establishes the acoustic suppression requirements for the attenuator.

We track the trajectory of these waves via a one-dimensional space-time (x-t) diagram. Such a x-t diagram is shown in Figure 9, based on the dimensions of the current design (normalized by the active cavity length) and a gas mixture 0.2/0.08/0.01/0.61 (F<sub>2</sub>/H<sub>2</sub>/O<sub>2</sub>/He). Other gas mixtures will be discussed later with only little differences in numerical results, but no differences in the basic physics discussed here. In this diagram, the waves are considered to propagate unattenuated and unimpeded in both the downstream and upstream directions. The reflection coefficient for the first reflection from the mixer plates is shown in Figure 10. As one can see in this diagram the initial downstream traveling wave slows down when it passes into the cool, low-sound-speed buffer gas, but has a higher velocity in the combustion products region. Upon traversing the interface between these regions, the initial downstream-traveling shock produces a reflected (upstream-traveling) expansion fan because of the mismatch in acoustic impedance between these regions. One also can see in this diagram, the initial upstream-traveling compression wave is reflected from the flow source region as a series of compression wavelets. The first of these wavelets is due to the slight blockage (area reduction) of the mixer region (see Figure 6), the second of these wavelets is due to the increase in blockage of the injection region (see Figure 6). Finally, a strong reflection occurs when the initial upstream traveling wave interacts with the closed upstream end of the injection region, where sonic orifices supply the injected gas species at externally controlled mass flow rates. The reflections of the initially upstream-traveling waves now travel downstream through the combustion products until they meet the interface between these (hot) combustion products and the (cold) buffer gas. At this interface, a strong reflection will occur, again due to the mismatch in acoustic impedance across it.

The magnitude ( $\Delta P/P$ ) of these reflections will be discussed later. It is clear, however, that to hasten the return of high optical homogeneity in the laser cavity, the magnitude of these reflected waves from the cold/hot and hot/cold interface must be minimized. It is the purpose of the interface decay module, or heat exchanger, to perform the function of both spreading the interface thickness and decreasing the impedance mismatch by dropping the gas temperature difference across the interface. Section III of this report describes the analyses used to design the heat exchanger (interface decay module) to produce such effects.

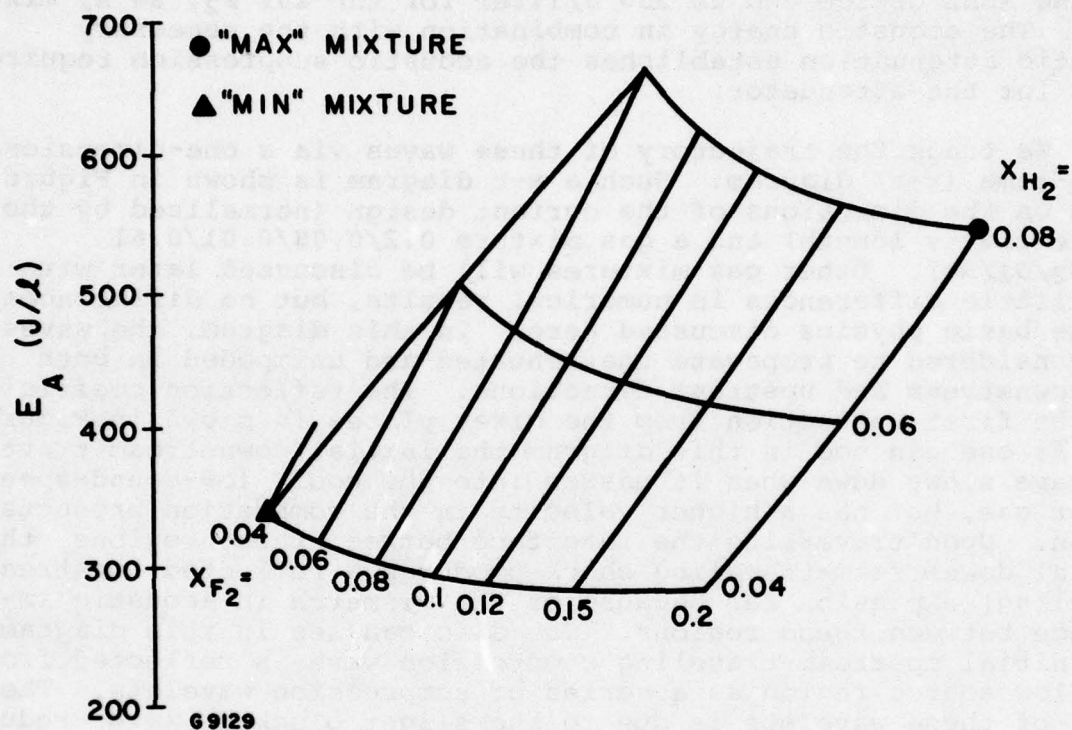


Figure 8 Acoustic Energy Release for Various HF/DF Reaction Mixtures



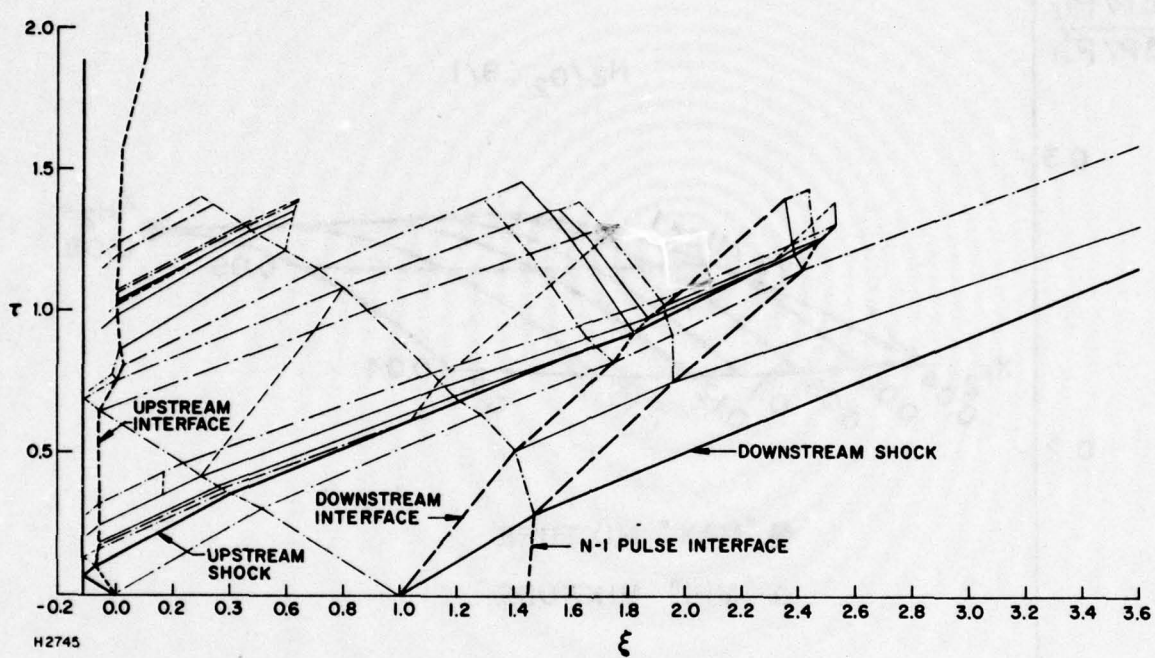


Figure 9 Early Wave History  $V_C = 36$  m/sec PRF = 60 pps

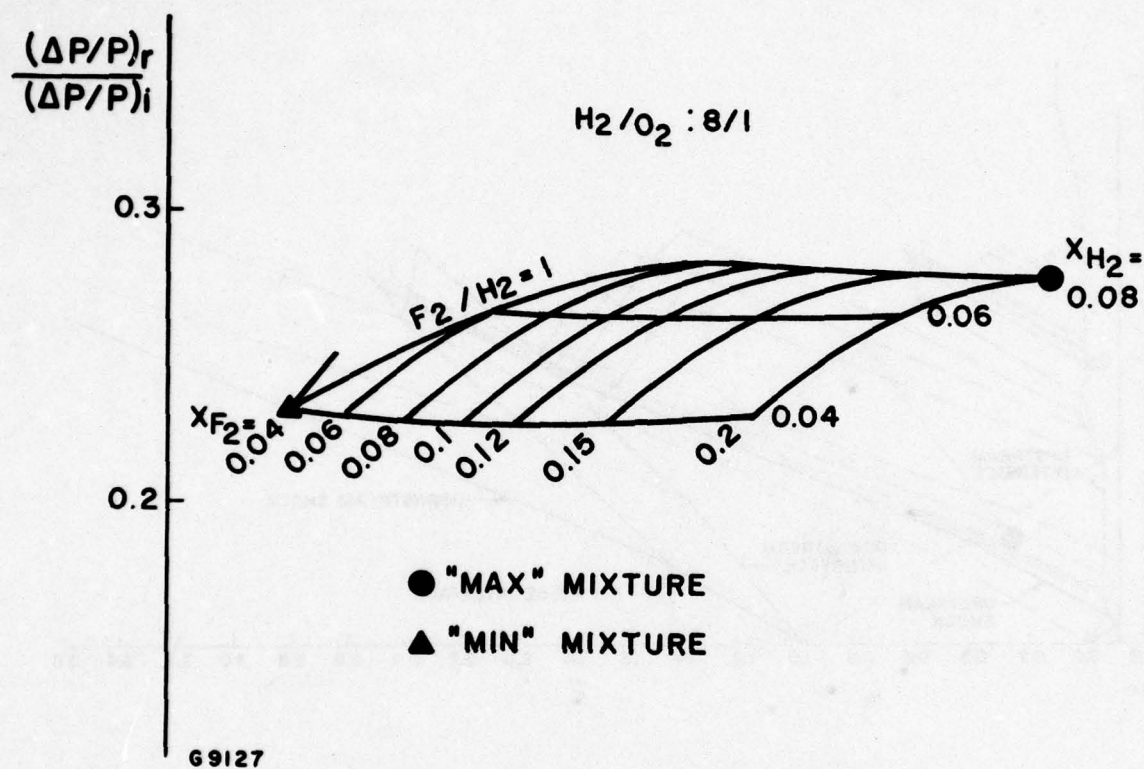


Figure 10 Reflection Coefficient for First Reflection from Mixing Plates (Non-Linear Analysis)



However, the heat exchanger parameters which minimize interface impedance mismatch also affect the overall density inhomogeneity in the cavity. Analysis is also presented below which addresses this question. Resultant heat exchanger parameters are chosen such as to minimize both acoustic reflections from the hot/cold interface as well as the density perturbations induced in the cavity due to transient flow dynamics in the heat exchanger region.

Section IV discusses the acoustic suppression scheme designed for the current device. It is located downstream of the heat exchanger module. It should be noted at this point that both Sections III and IV are analyses of constant-area flows. No explicit variation is made in open area available to the flow in the analyses presented in those sections. Discussion are included, however, within each section on design considerations affected by the inclusion of a downstream area change within the heat exchanger module (Section III) and the acoustic suppression (muffler) module (Section IV).

### SECTION III

#### HEAT EXCHANGER CONCEPT TO REDUCE THE EFFECT OF HOT/COLD GAS INTERFACES

A heat exchanger was used to reduce the effect of cold/hot interfaces in the pulsed HF laser. However, since the pressure drop across the heat exchanger depends on the mean temperature of gas in it, acoustic entropy and therefore density disturbance will be generated by the heat exchanger itself when the fresh slug of laser gas enters. These disturbances occur late in the interpulse time. Thus, we need an assessment of the medium inhomogeneity thereby induced to be sure that the heat exchanger in correcting one acoustical problem has not created another. The theory given here to make such estimates neglects phenomena occurring within acoustic transit times after the energy addition and takes advantage of the fact the flow Mach number is small ( $M \sim 0.06$  in the 60 pps device).

##### 1. LOW MACH NUMBER MODEL OF TRANSIENT HEAT TRANSFER

The following equations define a mathematical model of 1D transient flow including first order effects of friction and heat transfer.

$$\begin{aligned} \frac{\partial \rho}{\partial t} + \frac{\partial}{\partial x} (\rho u) &= 0 \\ \rho \left( \frac{\partial u}{\partial t} + u \frac{\partial u}{\partial x} \right) + \frac{\partial p}{\partial x} &= - \frac{2f}{d} \rho u^2 \\ \rho c_p \left( \frac{\partial T}{\partial t} + u \frac{\partial T}{\partial x} \right) - \left( \frac{\partial p}{\partial t} + u \frac{\partial p}{\partial x} \right) &= \frac{2f}{d} P^{-2/3} \rho u c_p (T_w - T_{aw}) \\ T_{aw} &= \left( 1 + \frac{\gamma-1}{2} r M^2 \right) T \end{aligned} \quad (22)$$

where  $d$  is the mean hydraulic diameter of passages in the heat exchanger,  $f = \tau_w / 1/2 \rho u^2$  is the friction factor,  $P = \mu c_p / k$  is the Prandtl number, and  $T_{aw}$  is the recovery or adiabatic wall temperature of the gas. Here the temperature of the solid matrix of the heat exchanger,  $T_w$  will be assumed constant in both space and time. Reynolds analogy has been used in deriving these equations.

While Eq. (22) can be treated numerically using the AERL HYBRID code, we have preferred a simpler formulation to get quick estimates which takes advantage of the fact the flow Mach number,  $M$ , is small. In this case the deviation in pressure from its



ambient value,  $P_a$ , produced by the heat exchanger is  $O(M^2)$ . The density, temperature, and velocity perturbations are all of  $O(1)$ . Since the adiabatic wall temperature  $T_{aw} = T$  within  $O(M^2)$  and  $p = p_a$  within  $O(M^2)$ , the energy equation becomes, to first order,

$$\frac{\partial T}{\partial t} + u \frac{\partial T}{\partial x} \approx \frac{2f}{d} P^{-2/3} u (T_w - T) \quad (23)$$

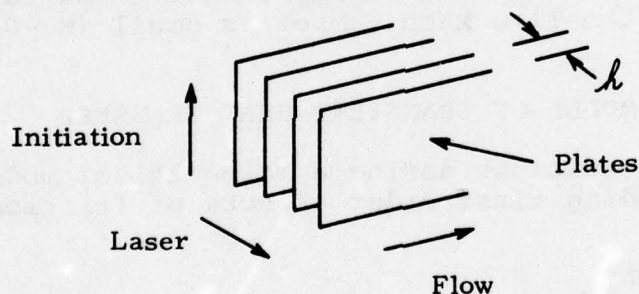
All terms in the momentum equation are of the same order of magnitude, so it is unchanged. Neglecting a term of  $O(M^2)$ , the density in the heat exchanger is given by the approximate equation of state

$$\rho \approx P_a / RT \quad (24)$$

Using this result and Eq. (23), the continuity equation becomes

$$\frac{\partial u}{\partial x} \approx \frac{2f}{d} P^{-2/3} u (T_w - T) / T \quad (25)$$

The heat exchanger consists of a large number of stainless steel plates arranged as shown below.



The plate spacing  $h = 1/8"$  to  $3/16"$  whereas the dimension transverse to the flow is of the order of 20 cm. Thus, the flow between two plates is essentially two dimensional. The effective hydraulic diameter  $d = 2h$  for a 2D flow configuration. The plate spacing is fixed, but the plates are staggered and are of variable length in the flow direction in the actual heat exchanger so that it will act as a flow scrambler. We will overlook such details in the subsequent analysis, and will also assume the side walls are flared in such a way that the effective flow area in the heat exchanger is constant and the same as upstream.

Let us turn now to boundary conditions. We take the region in front of the heat exchanger (say,  $-L < x < 0$ ) to be bounded upstream by a sonic orifice plate and overlook the presence of the mixing. The boundary conditions at a sonic orifice plate require

$$\begin{aligned} \rho u &= \dot{m} \\ \frac{\gamma RT}{\gamma - 1} + \frac{1}{2} u^2 &= \frac{\gamma RT_0}{\gamma - 1} \end{aligned} \quad (26)$$

and the mass flow and stagnation temperature are constant. For low Mach number flow it follows that  $T = T_c + O(M^2)$  and  $u = u_c + O(M^2)$  at the orifice plate, where subscript c denotes cold flow value. Acoustic waves in the region  $-L < x < 0$  produce flow perturbations satisfying  $\delta p + \rho a \delta u = 0$ , where the sign depends on the direction of propagation. Since  $\delta p = O(M^2)$  and  $u = u_c + O(M^2)$  at the sonic orifice plate, it follows that  $u = u_c + O(M)$  at the inlet to the heat exchanger. Thus by neglecting terms of  $O(M)$ , we can uncouple the analysis of the heat exchanger from the region upstream of it by adopting the boundary conditions

$$\left. \begin{aligned} u &= u_c \\ T &= \begin{cases} T_h, & 0 < t < L/u_c \\ T_c, & t > L/u_c \end{cases} \end{aligned} \right\} \text{ at } x = 0 \quad (27)$$

where  $T_h$  is the heated gas temperature after pressure equilibrium is achieved. For  $M \sim 0.06$  the relative error thereby committed shouldn't be more than 10%, which is acceptable for a first cut.

There is a muffler section downstream of the heat exchanger which is terminated by a scrubber which eventually opens to a large area. To understand the effect of the heat exchanger on cavity medium homogeneity, we can restrict attention to pressure deviations from ambient which are  $O(M^2)$  throughout the flow facility. That is, we overlook phenomena occurring within acoustic times after the laser pulse. Thus, if the muffler quickly dissipates downstream moving acoustic waves generated by the heat exchanger and if the pressure drop across the scrubber is reasonably constant in time, the pressure should be constant at the exit of the heat exchanger. On this basis we will assume

$$p = p_a \text{ at } x = H \quad (28)$$

to complete the set of required boundary conditions, where the heat exchanger lies in  $0 < x < H$ .

An initial condition on temperature is also required, and this is where the analysis becomes somewhat qualitative. There are two extreme possibilities. If the heat transfer from the hot gas to the heat exchanger is small during the acoustic damping time, the initial condition should be  $T = T_h$  at  $t = 0$ . On the other hand, if thermal equilibrium is achieved during the acoustic damping time, then the initial condition should be  $\partial T / \partial t = 0$  at  $t = 0$  and the gas temperature distribution in the heat exchanger can be inferred from Eq. (23). We will return to these two possibilities in discussing results. As it happens, the estimates of cavity homogeneity are little changed between these two initial conditions.



## 2. NUMERICAL SOLUTION PROCEDURE

Nondimensional variables are used in setting up the numerical procedure:  $\tilde{t} = u_c t / H$ ,  $\tilde{x} = x / H$ ,  $\tilde{T} = T / T_c$ ,  $\tilde{u} = u / u_c$ , and  $\tilde{p} = (p - p_a) / \rho_c u_c^2$ . The mathematical problem becomes

$$\begin{aligned} \frac{\partial \tilde{T}}{\partial \tilde{t}} + \tilde{u} \frac{\partial \tilde{T}}{\partial \tilde{x}} &= \alpha \tilde{u} (\tilde{T}_w - \tilde{T}) \\ \frac{\partial \tilde{u}}{\partial \tilde{x}} &= \alpha \left( \frac{\tilde{T}_w}{\tilde{T}} - 1 \right) \tilde{u} \\ \frac{\partial \tilde{p}}{\partial \tilde{x}} &= - \left( \frac{\partial \tilde{u}}{\partial \tilde{t}} + \tilde{u} \frac{\partial \tilde{u}}{\partial \tilde{x}} + \beta \tilde{u}^2 \right) / \tilde{T} \\ \tilde{u} = 1 \text{ and } \tilde{T} &= \begin{cases} \tilde{T}_h, & 0 < \tilde{t} < \tau \\ 1, & \tilde{t} > \tau \end{cases} \text{ at } \tilde{x} = 0 \\ \tilde{p} = 0 \text{ at } \tilde{x} &= 1 \end{aligned} \quad (29)$$

and an initial condition on  $\tilde{T}$ , where  $\alpha = (fH/h)P^{-2/3}$ ,  $\beta = fH/h$ ,  $\tau = L/H$ ,  $\tilde{T}_w = T_w/T_c$ , and  $\tilde{T}_h = T_h/T_c$ . Hereafter, we drop the tildes for notational simplicity with the understanding that all variables will be nondimensional.

The temperature field is updated using an explicit, first order accurate, upstream differencing scheme.

$$T_j^{k+1} = T_j^k + \left[ \alpha (T_w - T_j^k) - (T_j^k - T_{j-1}^k) / \delta x \right] u_j^k \delta t, 2 \leq j \leq N \quad (30)$$

where superscripts denote time step number, subscripts denote grid point number, and an equi-spaced grid is used with  $\delta x = 1/(N-1)$ . The temperature  $T_1^{k+1}$  is given by the boundary conditions. If the cold/hot interface is inside the heat exchanger ( $t > \tau$ ), the temperature on each side of the interface is determined by an explicit, first order accurate method of characteristics.

$$\begin{aligned} T_-^{k+1} &= T_-^k + \alpha (T_w - T_-^k) u_i^k \delta t \\ T_+^{k+1} &= T_+^k + \alpha (T_w - T_+^k) u_i^k \delta t \end{aligned} \quad (31)$$

where  $u_i^k$  is the interface speed at the previous time. The new interface position is taken to be given by

$$x_i^{k+1} = x_i^k + u_i^k \delta t \quad (32)$$

To avoid error in differencing across the interface, Eq. (30) is not applied at the grid point just downstream of the interface. Rather, the temperature there is determined by interpolation using  $T_+^k$  or  $T_-^k$  and the properties at the appropriate neighboring Eulerian grid point. For the same reason the time step is chosen to be

$$\delta t = 0.95 \delta x / \max \left( u_i^k, 1 \leq j \leq N (u_j^k) \right) \quad (33)$$

The finite difference scheme (Eq. (30)) would be numerically stable for

$$\delta t < 2 \delta x / \max_{1 \leq j \leq N} (u_j^k) \text{ and } u_j^k > 0 \text{ for all } j.$$

To minimize the constraint of numerical stability on  $\delta x$  and also because it entails no difficulty, the velocity field is updated with an implicit, second order accurate finite difference scheme:

$$u_j^{k+1} = \left( \frac{1+\Delta}{1-\Delta} \right) u_{j-1}^{k+1}, \Delta = \alpha \left[ 2T_w / (T_j^{k+1} + T_{j-1}^{k+1}) - 1 \right] \delta x \quad (34)$$

for  $2 \leq j \leq N$  with  $u_1^{k+1} = 1$  from the boundary conditions. If the interface is in the heat exchanger ( $t > \tau$ ) and its location  $x_i^{k+1}$  is between grid points  $j-1$  and  $j$ , the update procedure for that interval involves the two steps

$$\begin{aligned} u_i^{k+1} &= \left( \frac{1+\Delta_-}{1-\Delta_-} \right) u_{j-1}^{k+1}, \Delta_- = \alpha \left[ 2T_w / (T_-^{k+1} + T_{j-1}^{k+1}) - 1 \right] (x_i^{k+1} - x_{j-1}) \\ u_j^{k+1} &= \left( \frac{1+\Delta_+}{1-\Delta_+} \right) u_i^{k+1}, \Delta_+ = \alpha \left[ 2T_w / (T_j^{k+1} + T_+^{k+1}) - 1 \right] (x_j - x_i^{k+1}) \end{aligned} \quad (35)$$

where  $T_\pm^{k+1}$  are the updated temperatures on each side of the interface. Note that Eq. (35) defines the new interface speed,  $u_i^{k+1}$ .

The pressure field is uncoupled from the temperature and velocity fields, and all we are really interested in is the pressure at the inlet to the heat exchanger. Therefore, we need only define the integration scheme for computing  $p_0(t) = p(0,t)$ . If flow variables are defined as a continuous function of  $x$

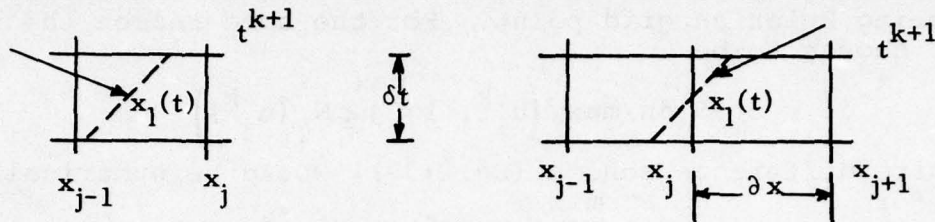
$$p_0^{k+1/2} = \int_0^1 \left\{ \frac{u^{k+1} - u^k}{\delta t} + \frac{\partial}{\partial x} \left[ \frac{1}{2} (u^{k+1/2})^2 \right] + \beta (u^{k+1/2})^2 \right\} \frac{dx}{T^{k+1/2}} \quad (36)$$

where  $u^{k+1/2} = u(x, t^{k+1/2}) = 1/2 [u(x, t^{k+1}) + u(x, t^k)]$ , etc. With a discrete definition of the flow variables, the integral is simply approximated by a mid-point rule. For example,

$$\int_{x_{j-1}}^{x_j} f^{k+1/2}(x) dx \approx \frac{1}{4} (f_j^{k+1} + f_j^k + f_{j-1}^{k+1} + f_{j-1}^k) \quad (37)$$



In the vicinity of a contact interface we modify this form in a way that depends on whether or not the interface has crossed a grid line in the time step. The two cases are illustrated below.



As an example, consider the case to the left. The rectangular region is divided into two trapezoids by the interface path, and the flow properties are known at the five corners of each trapezoid. An arithmetic mean of these properties gives a representative value over the trapezoid, and the contribution of each trapezoid to the cell  $(j-1, j)$  is weighted by its area relative to  $\delta x \delta t$ .

All this care in treating the interface may appear superfluous since both pressure and velocity are continuous across the interface. At first we implemented a simpler procedure which was expected to work. The nature of the results obtained forced the alternate treatment outlined here.

### 3. LINEARIZED HEAT EXCHANGER PROBLEM

To check out the nonlinear computer program discussed in the previous section we compared results from it to an analytic solution to the linearized heat exchanger problem. This problem results by substituting  $T = 1 + T^1 \Delta T$ ,  $u = 1 + u^1 \Delta T$ , and  $p = \beta (1 - x) + p^1 \Delta T$  into Eq. (29) and linearizing for  $\Delta T = T_h - 1$  small to find with  $T_w = 1$  that

$$\begin{aligned} \frac{\partial T^1}{\partial t} + \frac{\partial T^1}{\partial x} &= \alpha T^1 \\ \frac{\partial u^1}{\partial x} &= -\alpha T^1 \\ \frac{\partial p^1}{\partial x} &= -\beta (2u^1 - T^1) - \left( \frac{\partial u^1}{\partial t} + \frac{\partial u^1}{\partial x} \right) \end{aligned} \quad (38)$$

The boundary conditions are  $u^1 = 0$  and  $T^1 = \begin{cases} 1, & 0 < t < \tau \\ 0, & t > \tau \end{cases}$  at  $x = 0$  and  $p^1 = 0$  at  $x = 1$ . I will take  $T^1 = 1$  at  $t = 0$  as the initial condition.

A straightforward exercise with Laplace transforms leads to the following solution for the temperature perturbation:

$$T^1(x, t) = e^{-\alpha t} [1 - \mathcal{H}(t-x)] + e^{-\alpha x} [\mathcal{H}(t-x) - \mathcal{H}(t-x-\tau)] \quad (39)$$

where  $\mathcal{H}(t) = \begin{cases} 1, & t > 0 \\ 0, & t \leq 0 \end{cases}$  is the Heaviside unit function. The first term is associated with cool-down of hot gas which finds itself inside the heat exchanger at  $t=0$ , and the second term is associated with gas entering the heat exchanger inlet at  $x=0$  for  $t>0$ . The velocity perturbation is now found to be

$$u^1(x, t) = -\alpha x e^{-\alpha t} + \begin{cases} x, & t > x \\ t, & 0 < t < x \end{cases} \alpha e^{-\alpha t} \quad (40)$$

$$- \begin{cases} 1-e^{-\alpha x}, & t > x \\ 1-e^{-\alpha t}, & 0 < t < x \end{cases} + \begin{cases} 1-e^{-\alpha x}, & t > x+\tau \\ 1-e^{-\alpha(t-\tau)}, & \tau < t < x+\tau \end{cases} \mathcal{H}(t-\tau)$$

Finally, the perturbed pressure at the inlet to the heat exchanger for  $\tau < 1$  (the case of interest) is found to be equal to  $P(t)$  for  $0 < t < \tau$ ,  $P(t) + Q(t)$  for  $\tau < t < 1$ ,  $R(t)$  for  $1 < t < 1 + \tau$ , and zero for  $t > 1 + \tau$ , where

$$P(t) = \left[ \left( \frac{1}{2} \alpha^2 - \alpha \beta \right) (1-t) - (\alpha + \beta) \right] (1-t) e^{-\alpha t} - 2\beta t + \left[ \frac{\beta - \alpha}{\alpha} - 2\beta(1-t) \right] (1-e^{-\alpha t})$$

$$Q(t) = 2\beta(t-\tau) - \frac{\beta - \alpha}{\alpha} \left[ 1 - e^{-\alpha(t-\tau)} \right] + \left[ 2\beta + (\alpha - 2\beta) e^{-\alpha(t-\tau)} \right] (1+\tau-t) \quad (41)$$

$$R(t) = \frac{\beta - \alpha}{\alpha} e^{-\alpha(t-\tau)} - e^{-\alpha} - (2\beta - \alpha) (1+\tau-t) e^{-\alpha(t-\tau)}$$

The solutions for the perturbation in velocity at the exit to the heat exchanger and in pressure at the inlet to the heat exchanger are plotted in Figure 11 for  $\alpha = 2.157$ ,  $\beta = 1.701$ , and  $\tau = 0.6667$ . These parameter values correspond to  $\rho_c = 4.4 \times 10^{-4} \text{ g/cm}^3$ ,  $u_c = 3600 \text{ cm/sec}$ ,  $T_c = 300^\circ\text{K}$ ,  $P = 0.7$ ,  $h = 1/8 \text{ in}$ ,  $H = 60 \text{ cm}$ ,  $L = 40 \text{ cm}$ , and  $f = 0.009$  for fully developed turbulent pipe flow. The solid curve represents the analytical solution and the crosses are the numerical results. Note that  $p_c = p_a + \beta \rho_c u_c^2$ . Clearly, the agreement is good.

Within this model the cavity pressure increases discontinuously when the cold/hot interface first enters the heat exchanger, by amount  $\alpha$ . The source of this discontinuity is the inertia  $\partial u / \partial t$  which also increases by  $\alpha$  from  $t = \tau^-$  to  $t = \tau^+$ . This discontinuity is artifact of the assumption of small Mach number made in arriving at the approximate equations of motion used here. All we can be sure it means is that the pressure at the inlet to the heat exchanger increases by  $\alpha$  within acoustic time scales; it may do this smoothly or not

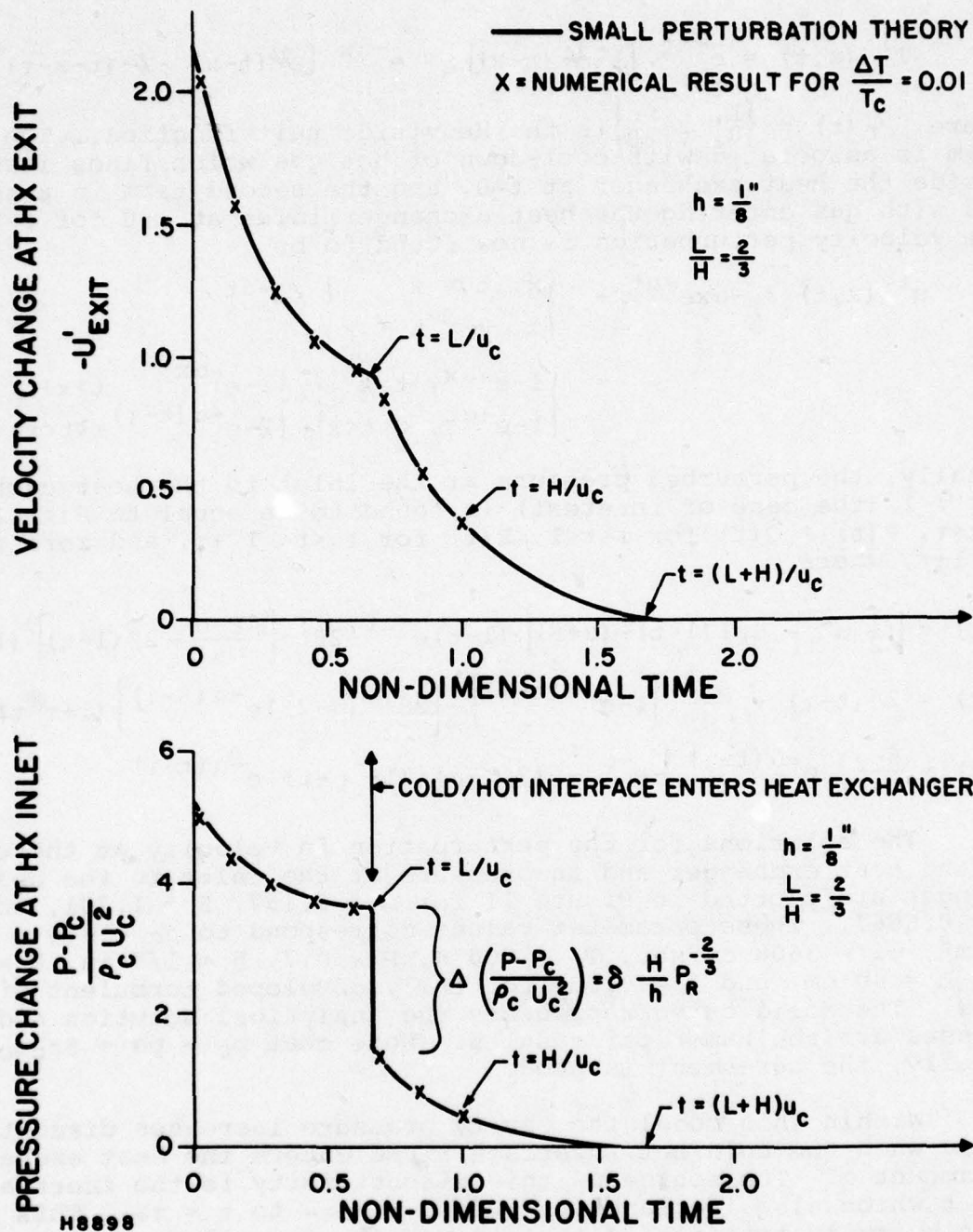


Figure 11 Solution of Heat Exchanger Problem for Small  $\Delta T/T_c$



#### 4. NONLINEAR HEAT EXCHANGER RESULTS

We now assess the effect of the initial condition assumed for temperature. We take the heated gas to be at 1300K after pressure equilibration, which is chosen to be a bit higher than the 1100K estimated from the Mollier diagram for a 20% F<sub>2</sub>, 8% H<sub>2</sub>, 71% He, and 1% O<sub>2</sub> laser mix in an effort to account for fluorine dissociation energy sink effects. The core of the heat exchanger is taken to be at either  $T_w = 300\text{K}$  or  $800\text{K}$  for these calculations, where the latter value would be the mean temperature of a passive heat exchanger core when the flush factor is two. Other parameter values are  $\rho_c = 4.4 \times 10^{-4} \text{ g/cm}^3$ ,  $u_c = 3600 \text{ cm/sec}$ ,  $T_c = 300\text{K}$ ,  $P = 0.7$ ,  $h = 1/8 \text{ in.}$ ,  $H = 60 \text{ cm}$ ,  $L = 40 \text{ cm}$ , and  $f = 0.009$  implying  $\alpha = 2.157$ ,  $\beta = 1.701$ , and  $\tau = 0.6667$ .

As explained before, there are two extreme possibilities for the initial condition. If no thermal equilibration occurs between gas and heat exchanger during the acoustic damping time, we should take the nondimensional  $T = 1300/300 \approx 4.333$  at  $t = 0$ . On the other hand, if thermal equilibrium is reached, we should take  $\partial T/\partial t = 0$  at  $t = 0$  and the gas temperature distribution is then implied by the energy equation. The numerical solutions for the pressure at the inlet to the heat exchanger obtained with these two initial conditions are shown in Figure 12. The difference is quite small for a core temperature of 800K and relatively small for a core temperature of 300K. A core temperature of 800K is of primary interest.

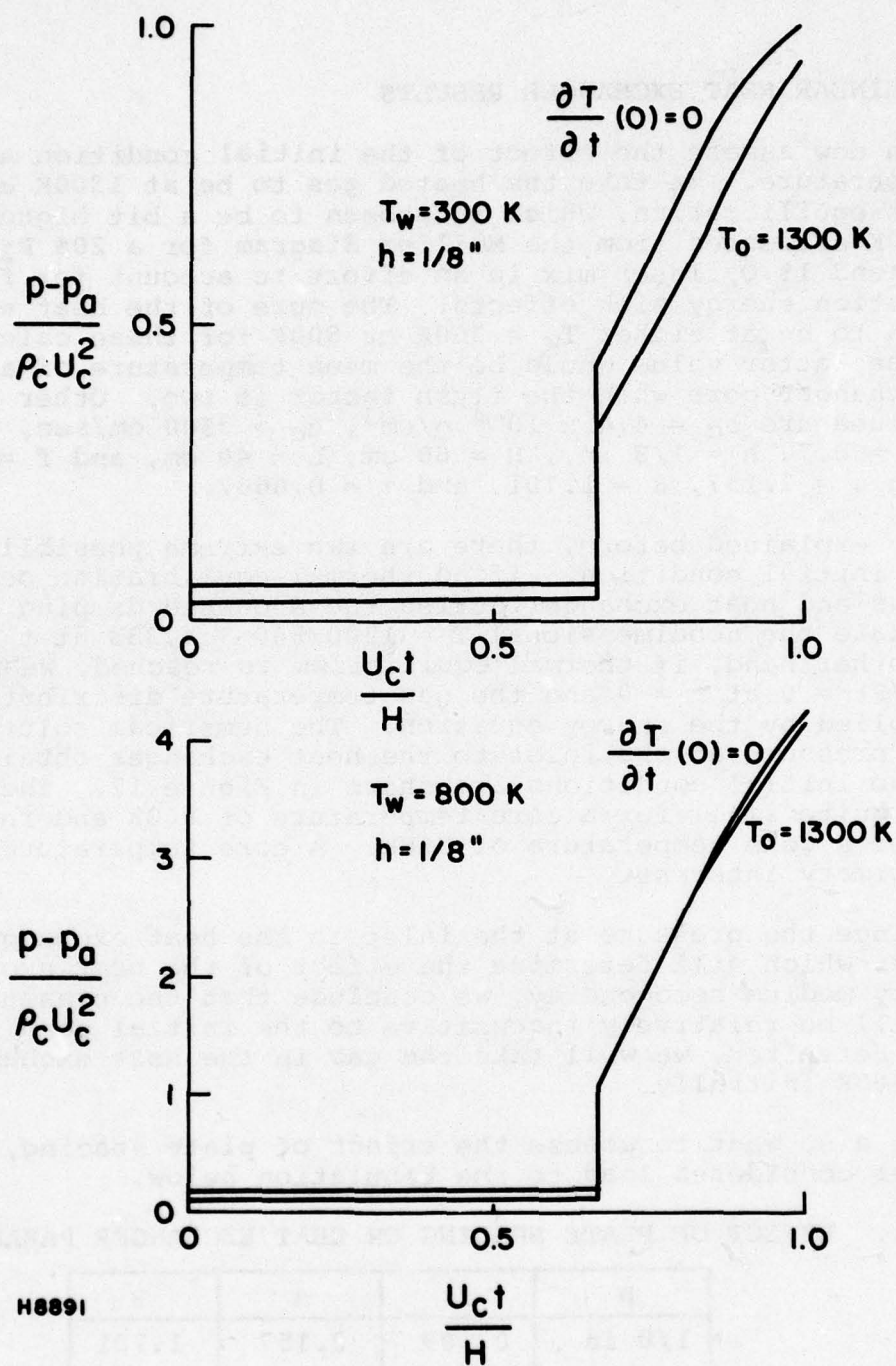
Since the pressure at the inlet to the heat exchanger is the parameter which will determine the effect of the heat exchanger on cavity medium homogeneity, we conclude that the pressure estimates will be relatively insensitive to the initial condition assumed. Hereafter, we will take the gas in the heat exchanger to be at 1300K initially.

We also want to assess the effect of plate spacing,  $h$ . The two cases considered lead to the tabulation below.

TABLE 1. EFFECT OF PLATE SPACING ON HEAT EXCHANGER PARAMETERS

$h$	$f$	$\alpha$	$\beta$
1/8 in	0.009	2.157	1.701
3/16 in	0.008	1.278	1.008

Other parameters are as noted before. The numerical predictions are shown in Figures 13 and 14. The pressure at the inlet to the heat exchanger varies, as a function of time, over a considerably larger range for the smaller plate spacing 1/8 in as should be



H8891

Figure 12 Effect of Initial Wall Temperature Condition on Pressure at Heat Exchanger Inlet

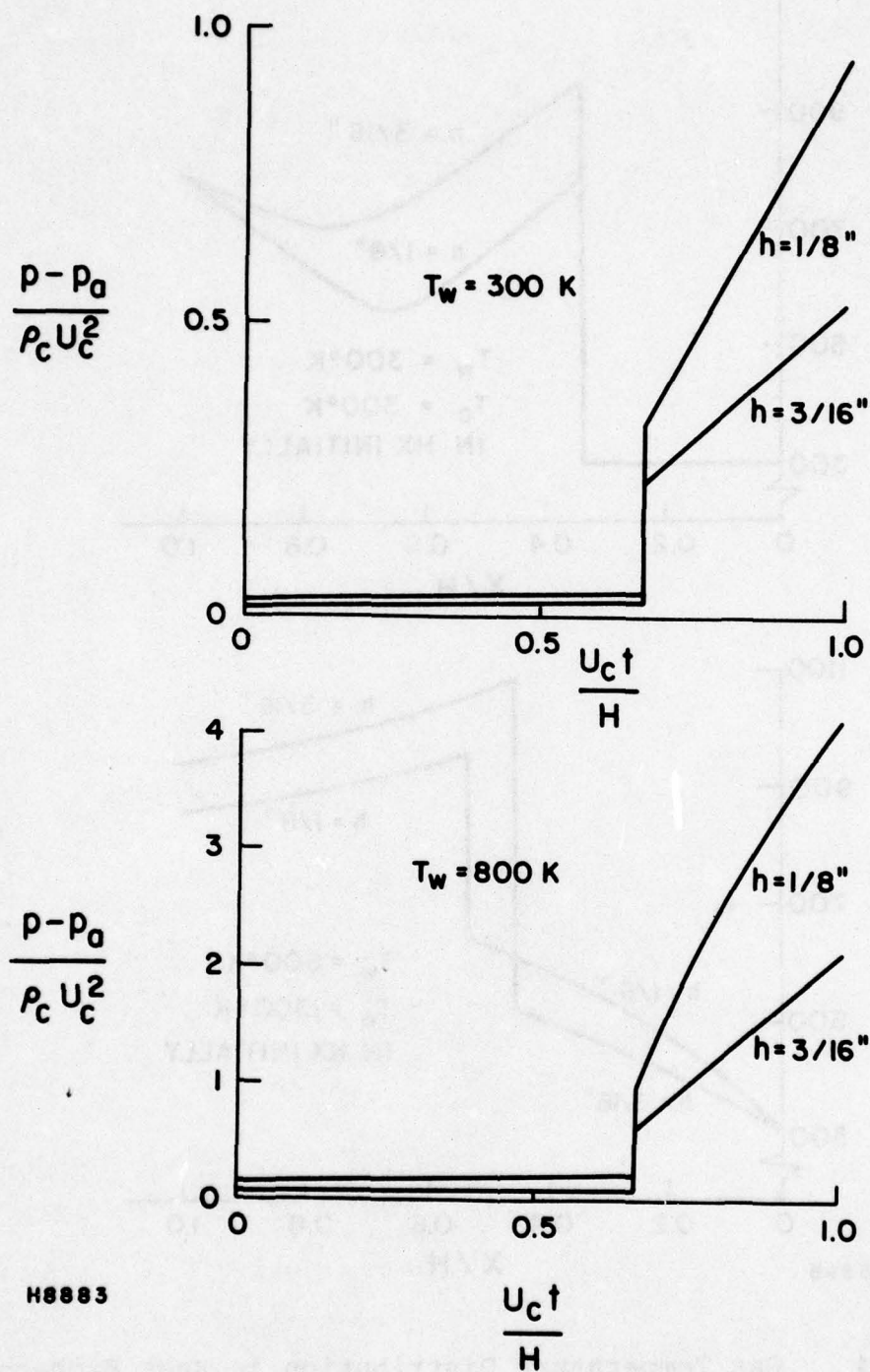
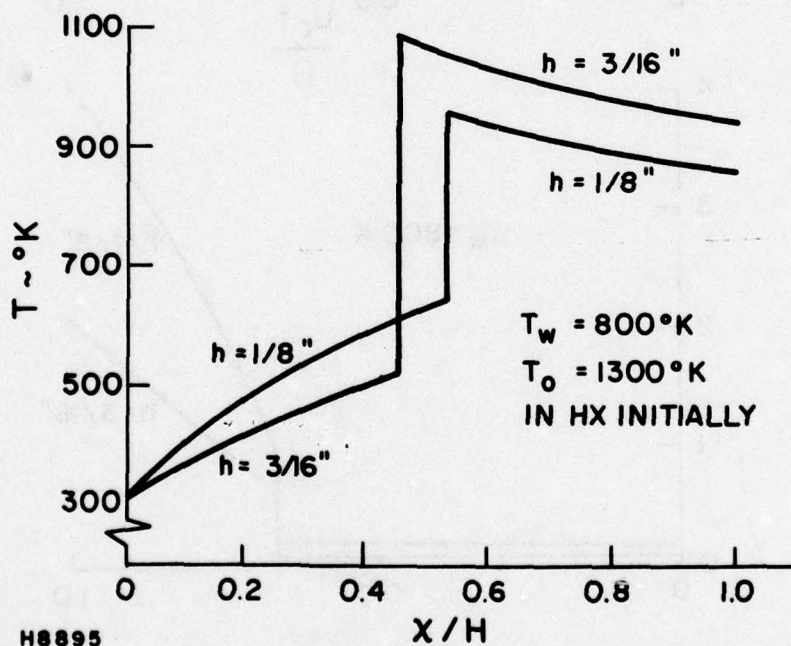
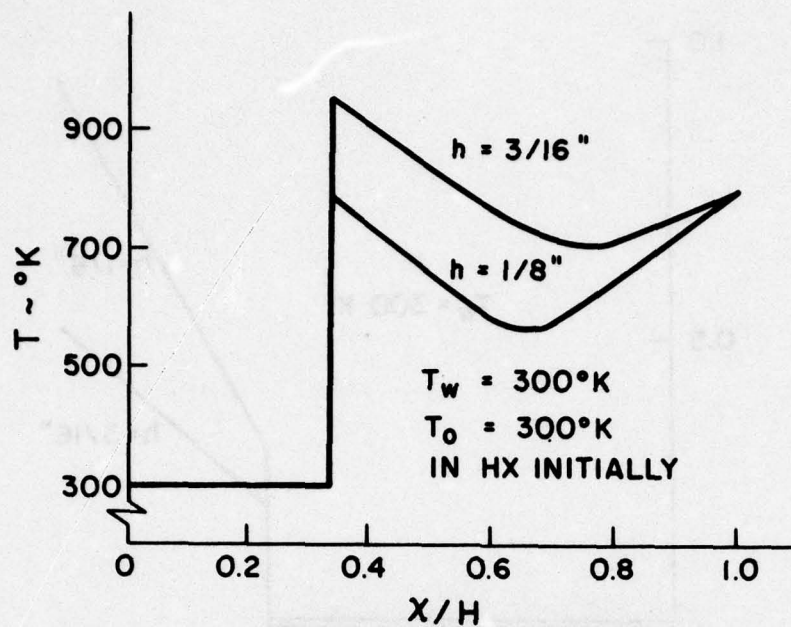


Figure 13

Effect of Plate Spacing on Pressure at Heat Exchanger Inlet ( $T_0 = 1300\text{K}$ )





H8895

Figure 14 Gas Temperature Distribution in Heat Exchanger at End of Interpulse Time (60 pps)

expected since the total wetted area is increased and this affects both the frictional losses and the momentum changes associated with heat transfer. We will return to Figure 13 in discussing optical cavity homogeneity in the next section.

The primary function of the heat exchanger is to reduce the magnitude of the discontinuous impedance mismatch across the cold/hot interface. The plots of gas temperature vs position in the heat exchanger given in Figure 14 are at the end of the interpulse time, which for the parameter values used happens to be at a non-dimensional  $t = 1$  for a 60 pps rep-rate, a laser cavity length of 30 cm, and a gas flush factor of two. The reflection coefficient  $R$  for weak acoustic waves interacting with the residual impedance mismatch discontinuity are tabulated below.

TABLE 2. CALCULATED ACOUSTIC REFLECTION COEFFICIENT FOR VARIOUS HEAT EXCHANGER DESIGN CONDITIONS

$h \quad T_w$	300K	800K
1/8 in	0.2344	0.0988
3/16 in	0.2804	0.1802

The reflection coefficient for linear interactions is

$$R = \left| (\zeta - 1) / (\zeta + 1) \right| \quad (42)$$

where  $\zeta = \sqrt{T_1/T_2}$  is the impedance ratio across the contact discontinuity and  $T_1$  and  $T_2$  are the temperatures on each side. The reflection coefficient with no heat exchanger would be  $R = 0.3510$ .

It is clear from the above that lowest acoustic reflection occurs for 1/8 in plate spacing and hot (800°K) walls.

There is a considerable loss in heat exchanger effectiveness on impedance ratio decrease if it is operated with the core at room temperature. It is likely that we will want to preheat the core in running acoustic tests because it will take a large number of pulses (~300-500) for the passive core to approach thermal equilibrium, due to its large thermal inertia. It is also evident that we want the plate spacing as small as is practical. What is practical depends not only on construction considerations, but also on the effect of the heat exchanger on medium homogeneity in the cavity.

There will also be acoustic reflections associated with the continuously varying gas temperature in the heat exchanger. These are taken to be not so serious because the reflected waves will be



spread out over length scales comparable to the cavity length. Since both compression and rarefaction waves are reflected, the time lag effect of a distributed reflection should tend to average these waves and produce a less serious effect than strong local reflection.

##### 5. HOMOGENEITY DEGRADATION IN LASER CAVITY DUE TO THE HEAT EXCHANGER

Having solved the transient heat transfer problem, which can be uncoupled from the cavity flow at low Mach number, let us go back and see what the solution implies about the effect of the heat exchanger on cavity medium homogeneity at the end of the interpulse time. Pressure equilibration in the cavity occurs within acoustic transit times, which in a low Mach number flow means almost instantaneously compared to the flow transit times relevant to pressure variation at the inlet to the heat exchanger. Thus, we take the pressure variations calculated above at the inlet to the heat exchanger to be instantaneously imposed throughout the cavity and in particular at the sonic orifice plate. The conditions thus produced will then flow into the cavity and produce a distribution across the cavity which is a reflection of the time-varying conditions at the heat exchanger inlet.

Let us return to dimensional variables. At the sonic orifice plate the boundary conditions (Eq. (26)) and the equation of state  $p = \rho RT$  imply

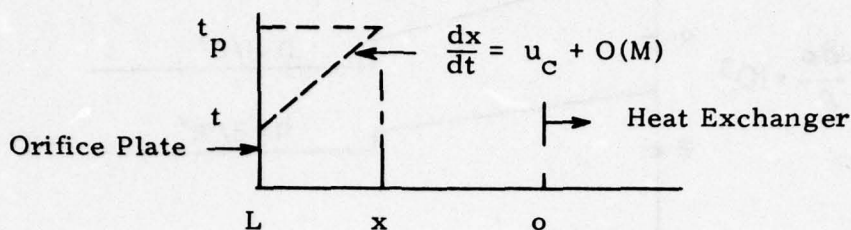
$$\begin{aligned}\frac{\delta T}{T} + (\gamma - 1) M^2 \frac{\delta u}{u} &= 0 \\ \frac{\delta \rho}{\rho} + \frac{\delta u}{u} &= 0 \\ \frac{\delta p}{p} &= \frac{\delta \rho}{\rho} + \frac{\delta T}{T}\end{aligned}\tag{43}$$

Thus, within a relative error of  $O(M^2)$ , the gas entering the cavity from the sonic orifice plate has density perturbed by amount

$$\frac{\delta \rho}{\rho}(t) \approx \frac{\delta p}{p}(t) \text{ at } x = -L\tag{44}$$

Within a relative error of  $O(M)$  this gas is swept through the cavity at the cold flow speed,  $u_c$ . A particular pathline is depicted in the sketch below.





Since entropy is preserved along the pathline, it must be true that

$$\frac{\rho(t_p)}{\rho(t)} = \left( \frac{P(t_p)}{P(t)} \right)^{1/\gamma}, \quad t \approx t_p - (x+L)/u_c \quad (45)$$

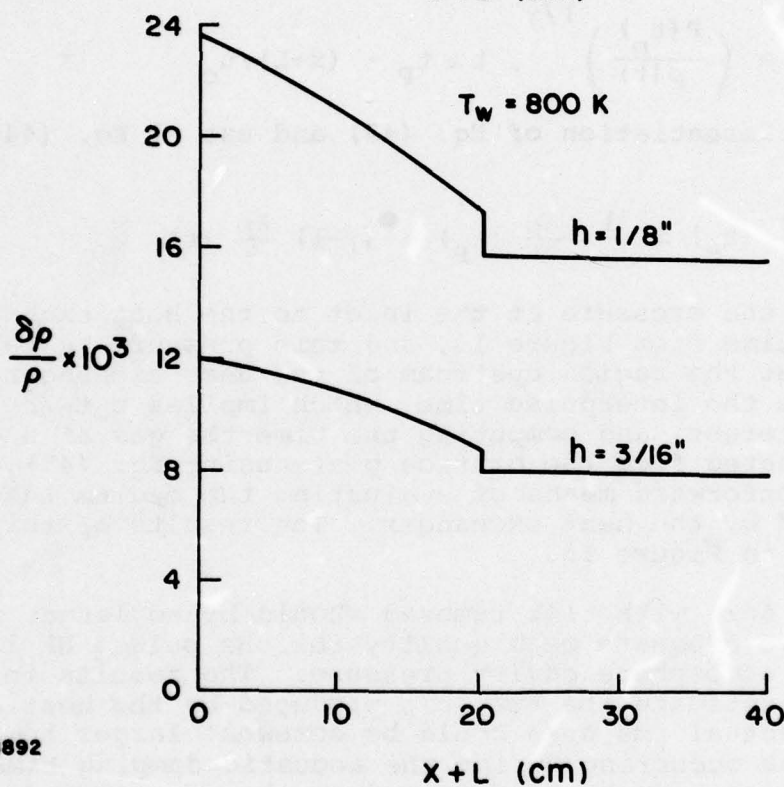
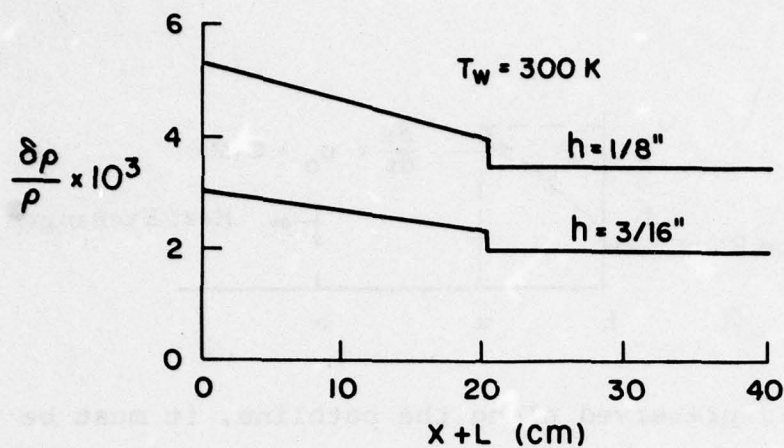
Logarithmic differentiation of Eq. (45) and use of Eq. (44) now leads to

$$\frac{\delta \rho}{\rho}(t_p) \approx \frac{1}{\gamma} \frac{\delta P}{P}(t_p) + (\gamma-1) \frac{\delta P}{P}(t) \quad (46)$$

We know the pressure at the inlet to the heat exchanger as a function of time from Figure 13, and this pressure is taken to apply throughout the region upstream of the heat exchanger. Thus, taking  $t_p$  to be the interpulse time, which implies  $u_c t_p / H = 1$  for the case of interest, and computing the time the gas at a given position originated from the orifice plate using Eq. (45), Eq. (46) gives a straightforward means of evaluating the medium inhomogeneity induced by the heat exchanger. The results of this evaluation are shown in Figure 15.

The rms  $\delta \rho / \rho$  with tilt removed should be no larger than about  $1 \times 10^{-3}$  to have adequate beam quality for the pulsed HF laser operating at one atmosphere cavity pressure. The results in Figure 15 allow us to estimate the rms  $\delta \rho / \rho$  produced by the heat exchanger. The actual rms  $\delta \rho / \rho$  could be somewhat larger however due to phenomena occurring during the acoustic damping time. Since optical corrections can be used to reduce the effective  $\delta \rho / \rho$ , estimates were made in which a series of Legendre polynomials are first subtracted from the  $\delta \rho / \rho$  distribution in Figure 15. The multipliers of these polynomials are chosen to minimize the residual rms  $\delta \rho / \rho$ . That is, we use a least-squares fitting procedure. A tabulation of the residual  $(\delta \rho / \rho)_{\text{rms}}$  is given below for the heat exchanger configurations considered.

In the third column only the zeroth order Legendre polynomial is used, in the fourth a combination of zeroth and first order polynomials is used, and in the last a combination of zeroth, first, and second order polynomials is used.



H8892

Figure 15 Density Perturbation at End of Interpulse Time  
( $T_o = 1300$ K)

TABLE 3. RESIDUAL  $\delta\rho/\rho$  RMS IN CAVITY AS AFFECTED BY HEAT EXCHANGER PARAMETERS

h	$T_w$	Constant (Zeroth Order)	Linear (Zeroth + 1st)	Quadratic (0th + 1st + 2nd)
1/8 in	300K	$0.67 \times 10^{-3}$	$0.24 \times 10^{-3}$	$0.15 \times 10^{-3}$
3/16 in	300K	$0.39 \times 10^{-3}$	$0.14 \times 10^{-3}$	$0.10 \times 10^{-3}$
1/8 in	800K	$2.93 \times 10^{-3}$	$1.08 \times 10^{-3}$	$0.54 \times 10^{-3}$
3/15 in	800K	$1.46 \times 10^{-3}$	$0.52 \times 10^{-3}$	$0.29 \times 10^{-3}$

A review of this table shows that a 60 cm heat exchanger with an 1/8 in plate spacing will cause an aberration in the cavity which is acceptable after a tilt correction. This will depend on the strength of aberrations produced by other phenomena, such as occur during the acoustic damping time. A heat exchanger with  $H = 60$  cm and  $h = 1/8$  in. seems required to adequately reduce the acoustic reflections off cold/hot interfaces in the device (see Table 2).

Table 3 shows the worst case of the heat exchanger. In practice the discontinuity in Figure 15 will be reduced by the gas volume in the laser cavity and by the staggering of the exit of the heat exchanger. This will result in the reduction of the quadratic and higher order term to an insignificant value. In any case the medium inhomogeneity disturbance caused by the heat exchanger will be identical from pulse-to-pulse and can be completely compensated for by refiguring the optics permanently. If adaptive optics are required for the laser to maximize the propagation through the atmosphere, the correction for the heat exchanger effect can be made at the same time.

#### 6. BLOCKAGE AND AREA VARIATION CONSIDERATIONS

As seen above, heat exchanger designs are expected to produce reflection coefficients at the resultant cold/hot gas interface in the range  $0.28 > R > 0.099$ , with the design recommendation ( $h = 1/8$  in,  $T_w = 800^\circ\text{K}$ ) producing a reflection coefficient calculated at 0.099.

The physical presence of this latter heat exchanger design condition is expected to produce an acceptable cavity density field when corrected optically.

However, the finite thickness of the plates of the heat exchanger fins must produce reflections of acoustic energy back into the cavity due to their blockage effect on the flow. Taking



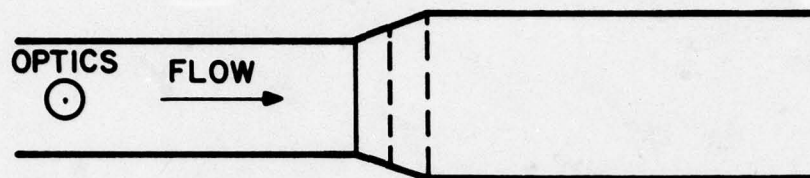
a minimum handleable thickness of the plates as 1/64 in., the blockage produced with the chosen 1/8-in. plate spacing produces a reflection roughly equal to the percent of total area which is blocked.

For the given heat exchanger plate thickness and spacing, a positive (compression) reflection coefficient of  $R = 0.11$  is calculated, which is on the order of the rarefaction reflection obtained from the cold/hot gas interface. These two reflections are displaced in time because the spatial origin of the compression reflection is at the heat exchanger inlet, while the spatial origin of the cold/hot reflection is at the location of the cold/hot gas interface (see Figure 14).

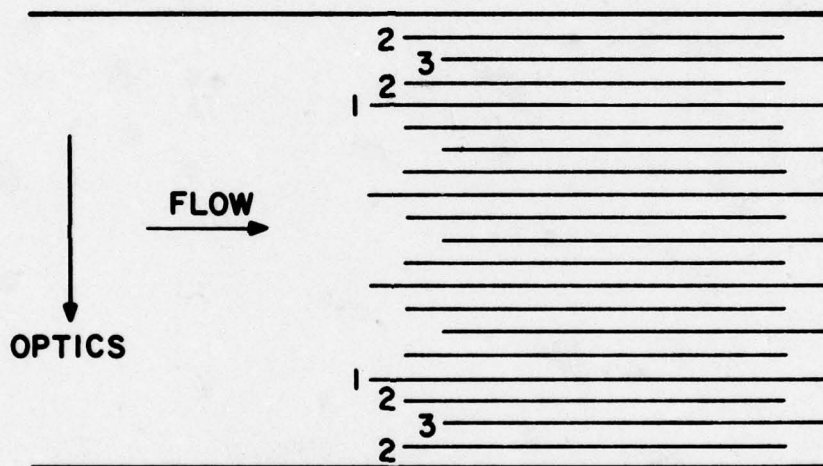
Consideration is currently being given to provide a variation in flow area within the heat exchanger to decrease the effect of the blockage-generated compression reflection on the density field in the optical cavity. Analyses (performed under AERL sponsorship) show the effect of the magnitude of the area ratio and the effect of the axial distribution of the area variation on flow properties at the inlet to the area variation. The results of these calculations indicate that the effect of downstream-expanding flow area is to send upstream-traveling rarefaction waves into the optical cavity. These can help decrease the amplitude of the upstream-traveling compression waves due to the finite thickness of the heat exchanger plates. In addition, consideration is being given to staggering the position of the leading edge of the heat exchanger plates such as to broaden the optical thickness of this upstream traveling compression wave, and also to allow the reflected rarefaction fans (due to area expansion within the heat exchanger) to act more effectively on this compression wave.

This concept is sketched (not to scale) in Figure 16. As can be seen, the compression reflections from the leading edges of the finite-thickness plates labelled (1) is followed by rarefaction reflections from the expanding flow area between the plates labelled (1). However, embedded in these rarefaction fans are the reflected compression waves from the tips of the plates labelled (2). Similar combinations of rarefaction and compression waves result for the flow channels between plates (2) and the tips of plates (3), etc.

It is clear that if substantial cancellation occurs due to this compression/rarefaction interaction, then the primary reflection (from plates (1)) results in a reflected compression wave of substantially reduced strength, perhaps as low as that due solely from the tips of plates (1) in Figure 16. For this simple case of a 3-plate pattern, the reflection coefficient could drop from its unstaggered, constant area value of  $R = 0.11$  to a value less than  $R = 0.04$ . This can be further reduced with designs for specific flow velocity, mixtures and given repetition rates.



SIDE VIEW



TOP VIEW

H8889

Figure 16 Schematic of Heat Exchanger Design for Decreased Net Reflection of Compression Waves

## SECTION IV

### ACOUSTIC SUPPRESSOR CONSIDERATION

#### 1. INTRODUCTION

We now turn our attention to the design of the acoustic suppression module, or muffler, located downstream of the heat exchanger described in Section III.

An early concept for the acoustic suppression scheme involved the use of a downstream area expansion (in the form of an exponential horn) to decrease the amplitude of the initial strong acoustic wave impinging on acoustic absorbers placed in the flow channel, but which allowed throughflow with low pressure drop (i.e., with low flow resistance). This concept was rejected subsequently for a number of reasons. It was found that any downstream area variation, regardless of its shape (exponential, hyperbolic, linear) produced strong reflections back into the cavity. Those reflections, also, appeared in the optical cavity at times sufficiently long after the initial laser pulse to compromise the desired PRF of the device design. Hence a constant-area muffler design was undertaken which would minimize reflected waves as well as rapidly decrease the amplitude of the initial downstream-traveling acoustic wave.

The initial shock Mach number generated at the chemically reacted laser cavity boundaries is 1.66 (20% F<sub>2</sub>, 8% H<sub>2</sub>/D<sub>2</sub>). Since the side and end wall flows (chemically inert) isolate this volume there is a reduction in the shock Mach number as the front fills the geometric volume and moves into the downstream heat exchanger. The Mach number at the entrance of the heat exchanger is estimated to be 1.41. There is further attenuation of the shock as it traverses the heat exchanger due to friction and heat transfer. Although the heat exchanger is passive (i.e., no active cooling) the shock increases the gas temperature locally. This incremental temperature rise causes heat transfer between the gas and the heat exchanger plates. Consequently the heat exchanger removes both momentum and energy from the gas stream through viscous effects and heat transfer respectively. The associated shock attenuation is significant and is a major contribution in the total acoustic suppression of the initial shock waves. The shock Mach number exiting the heat exchanger is 1.16.



There are two reflections of the shock from the heat exchanger. Both are due to flow blockage. The first is that due to the geometric blockage (11%) which reflects a wave with an amplitude of 6% of the incident wave. The second is an in-depth reflection associated with the boundary layer/shock interactions within the heat exchanger. The acceptable reflections are derived from the acoustic clearing time available.

The desired pulse repetition frequency of 60 Hz and cavity flow velocity of 36 m/sec result in a flow clearing time of 10.7 m/sec. This is the time of gas transit from the F<sub>2</sub>/H<sub>2</sub> injection to the downstream end of the laser cavity. The available acoustic clearing time is therefore 5.9 m/sec. Five reverberations of the acoustic waves in this period would dictate an acceptable heat exchanger reflection coefficient no greater than 0.39 (the mixer reflection is between 0.69 and 0.85 depending upon shock strength). The two sources of reflection indicated above will be shown to easily satisfy this constraint.

The acoustic attenuation requirements are established from the medium homogeneity requirement ( $\Delta p/p_{rms} = 1.1 \times 10^{-3}$ ). This requirement establishes the wave strength. Taking this requirement as a peak amplitude constraint (very conservative) gives a wave  $\Delta p/p$  of  $1.6 \times 10^{-3}$ . However, the critical requirement is imposed within the acoustic clearing time where the waves extant will be manifested in the cavity at the time of the next pulse as entropy disturbances. This wave strength requirement is  $\Delta p/p \leq 3.2 \times 10^{-3}$  at 5.9 m/sec. (compared to the  $1.6 \times 10^{-3}$  at 16.7 m/sec).

The wave, after leaving the heat exchanger, is further attenuated by the muffler which must also satisfy these requirements. Since the transit time in the muffler is long no reverberations are possible within the acoustic clearing time. The attenuation in the muffler must consider two regimes, i.e., strong shocks ( $M = 1.16$ ) and strong waves (S.P.L. = 1.53.6 db).

The characteristic frequencies that must be considered are those associated with the initial shock generated and the characteristic frequencies associated with acoustic transit times between the mixer and heat exchanger. This means that the muffler must have broadband performance over a frequency range 50 to 950 Hz. The strong wave attenuation required is 10 db which has been very conservatively taken to be that required over the frequency range of interest.

## 2. HEAT EXCHANGER ACOUSTICS

The relevant acoustic phenomena during the acoustic clearing time are those associated with the strong wave interactions and their attenuation. The first interaction is that due to the

blockage of the heat exchanger. The reflections associated with this blockage (11%) is small (~ 6%) and is within the reflection constraint.

The next interaction of concern is that due to the viscous effects within the heat exchanger. The flow behind the shock entering the heat exchanger soon after the initiation is relatively cool compared to the HX surface. As a consequence the boundary layer displacement thickness will be large, this in conjunction with the high subsonic flow behind the shock will result in a choking condition which results in a reflected shock back into the cavity. This interaction will be addressed below. The interaction with the hot gas interface from the previous pulse was discussed in Section III.3.

The attenuation of the shock as it traverses through the HX is necessary in order to establish the requirements on the muffler. Fortunately, the attenuation for strong waves is high which reduces the requirements on the muffler. This attenuation is high since both the friction and heat transfer effects in this case are additive.

#### a. Viscous Interaction

The boundary layer displacement thickness in conjunction with HX plate spacing results in an area variation, which interacts with the shock and generates reflected waves. In the analysis conducted, this interaction was considered to occur where the fully developed (turbulent) flow is established. The analysis was simplified by considering the flow bulk temperature to be constant at the cold gas temperature of 300°K whereas the wall was at a constant bulk temperature of 800°K. Since the bulk temperature of the gas is increasing with distance these results are approximate, however, they will be conservative since colder gas results in larger displacement thickness, hence, reflections.

The displacement thickness was established on the basis of relations determined by curve fitting the results of a parametric study, of compressible turbulent boundary layer with heat transfer. The computer program used was one where a two-layer model of the turbulent boundary layer was used.

In the absence of a pressure gradient, the boundary layer form factor H is given by

$$H = \frac{\delta^*}{\theta} = 0.547 \frac{T_w}{T_r} + (0.53 + 0.68 \frac{T_w}{T_r}) M_e + (0.083 + 0.106 \frac{T_w}{T_r}) M_e^2 \quad (47)$$



where  $\delta^*$  = displacement thickness,

$\theta$  = momentum thickness,

$T_w$  = wall temperature,

$T_r$  = adiabatic wall temperature, and

$M_e$  is the flow Mach number.

The adiabatic wall temperature is obtained from the relation

$$T_r = T_e \left[ 1 + \frac{\gamma-1}{2} r M_e^2 \right] \quad (48)$$

where

$T_e$  is the gas temperature behind the shock and

$r$  is the recovery factor (0.89 for turbulent flow)

The momentum thickness is also correlated as

$$\frac{h}{2\theta} = \frac{10.25}{\left(\frac{T_e}{T^*}\right)^a} \left[ \frac{\log_{10} R_{eD}^*}{\log_{10} R_{eD}} \right]^{2.58} \quad (49)$$

where

$h$  is the passage height,

$T^*$  is the reference temperature

$$a = 1 + 0.24 (1 + M_e)^{0.067}$$

$R_{eD}$  is the Reynolds' number based on hydraulic diameter ( $2h$ ) and flow behind shock, and  $R_{eD}^*$  is the Reynolds number at the reference temperature.

The reference temperature is given by

$$T^* = \frac{1}{2} T_w + \frac{1}{2} T_e (1 + 0.186 \frac{\gamma-1}{2} M_e^2) \quad (50)$$

The Mach number behind the shock entering the heat exchanger is 0.71 with a gas temperature of 473.6°K and density of  $9.47 \times 10^{-4}$  g/cm<sup>3</sup>. The viscosity evaluated for the gas mixture in the heat exchanger (a mixture of the reacted gas, the flush gas and the boundary flows) is given by



$$\mu = 6.498 \times 10^{-6} T^{0.647} \quad (51)$$

The blockage that results from this analysis is 22.3%. The reflected wave was established for this blockage combined with the HX plate thickness blockage (11.%). Unsteady one-dimensional analysis was utilized to determine the reflected wave. The corresponding reflection coefficient is 0.167 which is well within the constraint.

#### b. Shock Attenuation in the Heat Exchanger

The shock is attenuated as it passes through the HX due to wall friction and heat addition. The flow within the HX comprises the reacted gases, the flush gas and the edge and boundary flows. The shock will experience varying attenuation as it passes alternately through the various regions. The complexity of analyzing this situation was circumvented by establishing a mass average gas temperature within the HX (this should be the HX temperature after sufficient run time). This temperature was established as 679.9°K for the gas mixtures extant.

The method used was that of Whitham (Ref. 7) and gives for the rate of change of shock Mach number ( $M_s$ )

$$\begin{aligned} \frac{dM_s}{d(s/h)} = \frac{f}{h} \left\{ P_r^{-2/3} \left( \frac{T_w - T_r}{T_e} \right) - M_e + (\gamma - 1) M_e^2 \right\} \\ \times \frac{M_s^2 - 1}{M_s^2} \left( 1 + \frac{2}{\gamma - 1} \frac{1 - \eta^2}{\eta} \right)^{-1} \left( 1 + 2\eta + M_s^{-2} \right)^{-1} \end{aligned} \quad (52)$$

where the previously undefined parameters are

$f$  is the friction factor,

$P_r$  is the Prandtl number, and

$$\eta^2 = (1 + \frac{\gamma - 1}{2} M_s^2) / (M_s^2 - \frac{\gamma - 1}{2}) \quad (53)$$

The flow Mach number,  $M_e$ , is found from

$$M_e = \frac{(M_s^2 - 1 + \frac{\gamma + 1}{2} M_o M_s)}{\{(\gamma M_s^2 - \frac{\gamma - 1}{2})(1 + \frac{\gamma - 1}{2} M_s^2)\}^{1/2}} \quad (54)$$

where  $M_o$  is the flow Mach number in front of the shock.

The initial shock Mach number was determined for the gas bulk temperature of 679.8°K and is 1.407 (solution of the non-steady relations for an interaction between a shock and a hot gas interface.)

The above relations were integrated for a constant friction factor evaluated at the initial flow conditions behind the shock. The shock attenuates, thus the assumption is conservative. The shock Mach number at exit from the HX is 1.158 (an attenuation of 9.2 db in the HX).

### 3. MUFFLER ACOUSTICS

The density uniformity requirement of  $\Delta\rho/\rho = 1.1 \times 10^{-3}$  establishes the strength of the acceptable waves within the cavity at the time of the initiation,  $\Delta p/p = \gamma \Delta\rho/\rho = 1.7 \times 10^{-3}$ , as well as at the mixer within the acoustic clearing time,  $\Delta p/p = (\gamma/\gamma-1) \Delta\rho/\rho = 3.1 \times 10^{-3}$ . The latter requirement results since this disturbance appears as an entropy disturbance at the time of the next pulse initiation. The round trip time for the shock to travel through the muffler and back through the mixer is 6.5 m/sec which is slightly higher than the acoustic clearing time (5.9 m/sec). This disturbance will be in the optical cavity region at the time of the next pulse as an entropy disturbance. Thus the required attenuation (round trip) in the muffler must be greater than

$$\text{Attenuation db} = 20 \log_{10} \frac{0.412}{3.1 \times 10^{-3}} = 42.5 \text{ db}, \quad (55)$$

where  $\Delta p/p = 0.412$  leaving the HX.

The attenuation through the muffler is considered first as an attenuation of a shock and after a full reflection from the end (conservative) as the attenuation of strong waves. The latter assumption is supported in part by the small scale ABEL acoustic measurements at its muffler exit where a sinusoidal pressure variation was measured. The wave attenuation requirements are established from the shock attenuation and from the required overall attenuation.

### 4. MUFFLER SHOCK ATTENUATION

Szumowski (Ref. 8) studied the problem of the propagation of a shock wave in a constant-area porous walled tube. In this reference, a numerical scheme was constructed to compute the characteristics of the unsteady flowfield by the Method of Characteristics, and compared with Witham's method (Ref. 7). Both

8. Szumowski, A.P., "Attenuation of Shock Wave Along a Perforated Tube." Shock Tube Research Proc. Eighth Int. Shock Tube Symp., Chapman and Hall, 1971.



analyses were compared with data taken on the decay of the shock Mach number along the tube length as a function of both initial shock Mach number and tube porosity. Method of Characteristics solutions agreed well with measurements. The comparisons of these numerical results with Witham's method are shown in Figure 17. In this figure, the downstream distance  $x$  is nondimensionalized by the (circular) tube diameter and shown as  $\bar{x}$ , and the fractional open area of the tube walls is shown as  $\alpha$ . As can be seen, agreement between exact and approximate solutions improves with decreasing initial Mach number. Consequently we have used the method of Whitham (Ref. 7) to analyze shock attenuation in the muffler for our application.

#### a. Muffler Shock Attenuation

The muffler shock attenuation established by Whitham's (Ref. 7) method is similar to that described above for the HX. In this case rather than friction and heat transfer, the mechanism of attenuation is that of mass momentum and energy removal through a porous wall. The shock variation is given as

$$\frac{dM_s}{\frac{L}{H} d(x/L)} = 2\sigma F \frac{M_s^2 - 1}{M_s} \left(1 + \frac{2}{\gamma+1} \frac{1 - \eta^2}{\eta}\right)^{-1} \left(1 + 2\eta + M_s^{-2}\right)^{-1} \quad (56)$$

where  $L$  is the muffler length

$x$  is the distance into the muffler

$\sigma$  is the open area ratio of the porous wall

$H$  is the passage height (distance between porous walls)

$$F = \frac{M_j}{M_e} \left( \frac{1 + \frac{\gamma-1}{2} M_e^2}{1 + \frac{\gamma-1}{2} M_j^2} \right)^{\frac{\gamma+1}{2(\gamma-1)}} \frac{A_j}{A_p} \left\{ 1 - M_e \left[ \frac{M_j}{M_e} \left( \frac{1 + \frac{\gamma-1}{2} M_e^2}{1 + \frac{\gamma+2}{2} M_j^2} \right) \times \right. \right. \\ \left. \left. \frac{\rho_e}{\rho_p} \frac{A_j}{A_p} \cot \alpha \right] \times [1 - (\gamma-1) M_e] \right\} \quad (57)$$

where

$M_e$  is the flow Mach number behind the shock

$M_j$  is the jet Mach number through the orifice



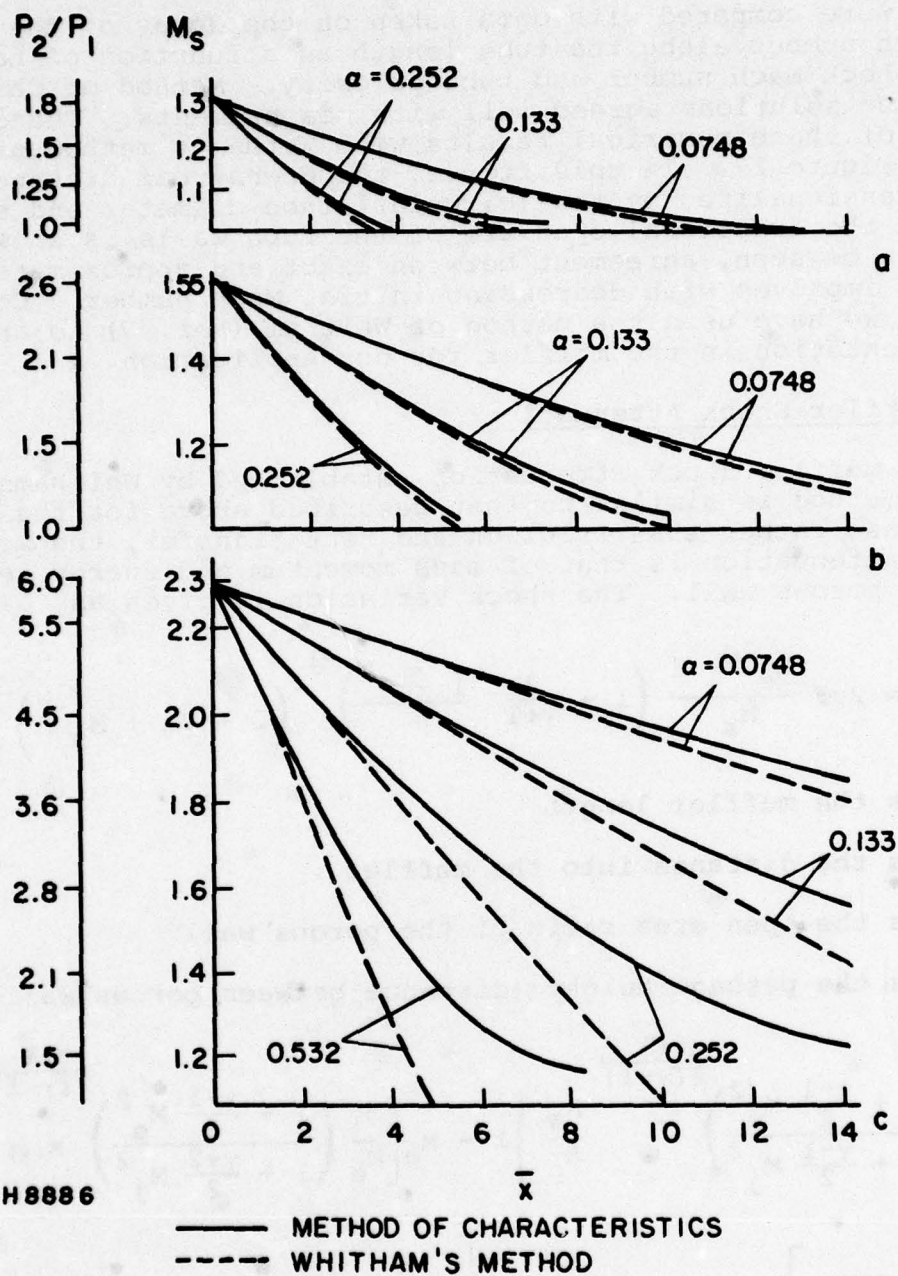


Figure 17 Tube Axial Variation of Shock Mach Number for Various Open Area Rates

$A_j/A_p$  is the jet contraction

$\alpha$  is the angle between the jet and the wall, and

$\rho_e/\rho_p$  is the ratio between the flow and porous wall gas density.

The muffler consists of steel wool sandwiched between two panels each of which are 40% open. The stainless steel wool which is approximately 98% porous is placed for wave attenuation as discussed below. The shock attenuation analysis neglects the presence of the steel wool. It is uncertain what the quantitative effect is, however qualitatively the stainless steel wool will effectively block the panel holes considerably more than inferred by its porosity because of its high resistance particularly to high speed flows.

The integration of the above relation results in a shock Mach number at the muffler exit of 1.00395 giving an attenuation of 32.7 db. There remains then a wave attenuation requirement of 10.0 db.

#### b. Transverse Gas Expansion in the Muffler

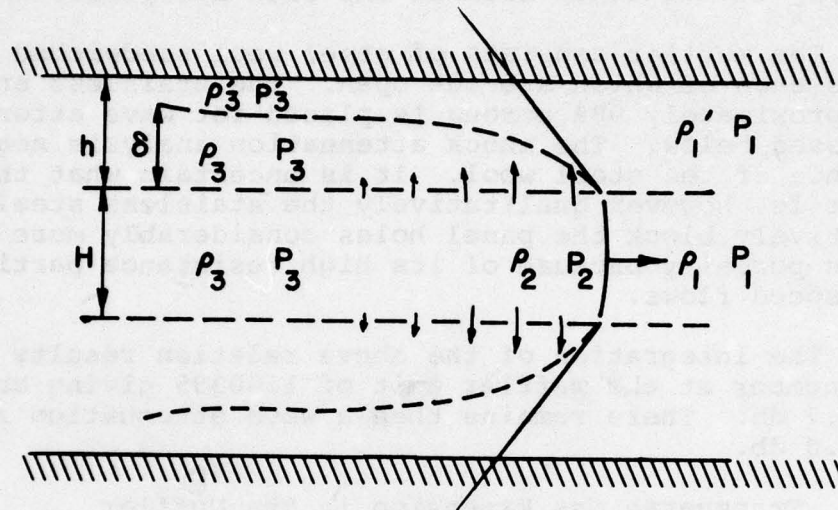
The above analysis assumes an infinite reservoir surrounding the porous-walled shock tube. This is not the situation in the present experimental design where the mass loss through the porous wall must be confined and expelled through a chemical scrubber system before release to the environment.

We expect, therefore, that some level of acoustic reflections back through the porous wall will occur in the present muffler system because of the relatively close proximity of the impermeable shroud around the porous inner wall.

The pressure level behind the initial downstream-traveling shock wave is 1.41 atm absolute. Lateral expansion of this down to close to 1 atm puts a requirement on the "empty" volume behind the porous wall.

In the notation of Figure 18, we equate the "original" mass per unit length in the flow channel  $\rho_2 H$  to the mass spread into the side volume plus the mass remaining in the flow channel. In the limit we have, then, for the gas originally in the channel

$$\frac{\rho_2}{\rho_1} = \frac{\rho_3}{\rho_1} \left( 1 + 2 \frac{\delta}{H} \right) \quad (58)$$



H8896

Figure 18 Notation for Transverse Gas Expansion in the Muffler



Across the contact interface between the original gas in the side volumes and the gas which has just entered them, we must have a pressure balance, hence, we have  $P_3 = P_3'$  far behind the shock front. Here we obtain

$$2 \rho_1' h = 2 \rho_3 (h - \delta)$$

or

(59)

$$\delta = h \left( 1 - \frac{\rho_1}{\rho_3} \right)$$

Substituting this expression into the above, we obtain a relation between the final density ratio in the muffler vs the initial density ratio

$$\frac{\rho_3}{\rho_1} = \frac{\rho_2}{\rho_1} \frac{1}{1 + 2 \frac{h}{H} \left( 1 - \frac{\rho_1}{\rho_3} \right)} \quad (60)$$

Assuming isentropic expansion from state  $\rho_2$  to state  $\rho_3$ ; assuming isentropic compression from state  $\rho_1$  to state  $\rho_3$ ; noting that  $P_3' = P_3$ ; and assuming that the specific heat ratio  $\gamma$  for the burned and the unburned gas are close in numerical value ( $\gamma = 1.2$  is assumed), we find

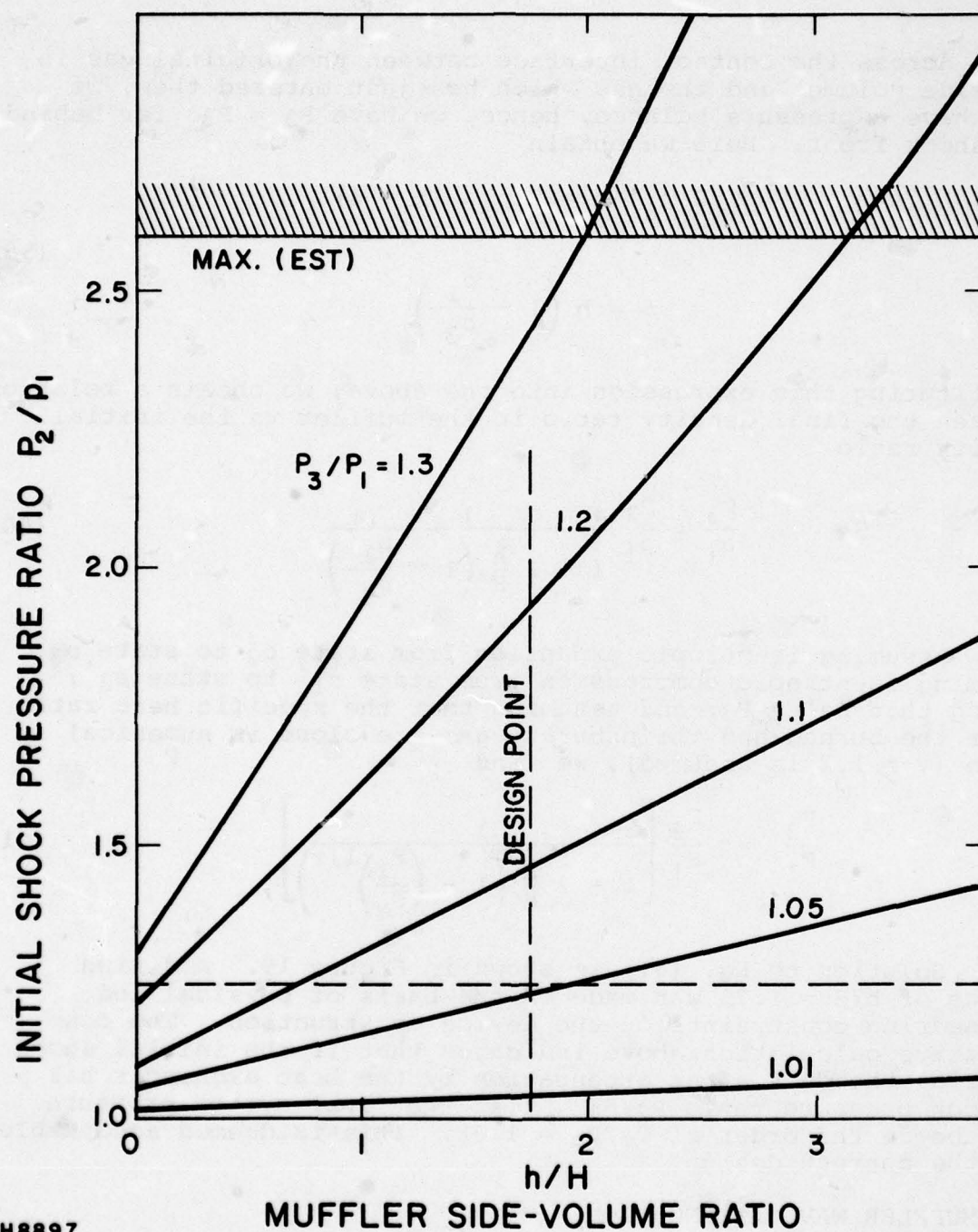
$$\frac{P_3}{P_1} = \frac{P_2}{P_1} \left[ \frac{1}{1 + 2 \frac{h}{H} \left( 1 - \left( \frac{P_1}{P_3} \right)^{1/\gamma} \right)} \right]^\gamma \quad (61)$$

Solution to Eq. (61) is shown in Figure 19. A design choice of  $h/H = 1.75$  was made on the basis of physical and engineering constraints on the device construction. The conservative calculation above indicates that if the initial shock entering the duct after attenuation by the heat exchanger has a shock pressure ratio  $P_2/P_1 = 1.41$  the final system pressure will be on the order of  $P_3/P_1 = 1.08$ . This is deemed acceptable for the current design.

## 5. MUFFLER WAVE ATTENUATION

The wave attenuation is given by the expression

$$\text{Attenuation db} = 4.343 R \left( \frac{1}{Z} \right) \rho c 2 \left( \frac{L}{H} \right)$$



H8897

Figure 19 Final Pressure Ratio in the Muffler due to Lateral Gas Expansion as Related to Initial Pressure Ratio and Side Volume Ratio

where

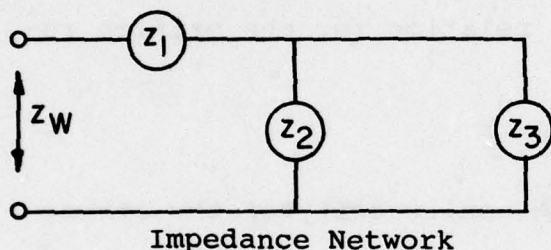
$R(1/z)$  is the real part of the complex wall impedance (RAYLS<sup>-1</sup>), and

$\rho c$  is the acoustic impedance of the gas mixture (RAYLS).

The required attenuation and the design muffler length and the height ratio (9:1) result in

$$R\left(\frac{1}{z}\right) = 1.327 \times 10^{-2} \text{ RAYLS}^{-1}$$

The complex impedance,  $z_w$ , of the wall was determined for the network illustrated below.



- $z_1$ : Front panel impedance and steel wool impedance
- $z_2$ : Impedance of space between panels
- $z_3$ : Impedance of cavity behind wall with back panel

The complex impedance  $z_w$  is found to be

$$z_w = \frac{z_1 z_2 + z_1 z_3 + z_2 z_3}{z_2 + z_3}$$

where

$$\frac{z_1}{\rho c} = \frac{1}{m} 1.18 \left(\frac{u_o}{c}\right) + j \frac{1}{m} (t + 0.85 d) \left(\frac{\omega}{c}\right) + \frac{R_{ssw}}{\rho c}$$

$$\frac{z_2}{\rho c} = -j \frac{1}{(\omega/c)L_2}, \text{ and}$$

$$\frac{z_3}{\rho c} = \frac{1}{m} 1.18 \left(\frac{u_o}{c}\right) + j \frac{1}{m} (t + 0.85 d) \left(\frac{\omega}{c}\right) - j \frac{1}{(\omega/c)L_3}$$

where  $m$  is the number of holes per cell,

$u_o$  is the orifice velocity,

$t$  is the panel thickness,



$d$  is the orifice diameter,

$\omega$  is the frequency in rad/sec,

$R_{ssw}$  is the steel wool resistance,

$L_2$  is the separation of the two panels, and

$L_3$  is the cavity height behind the back panel.

The orifice velocity is established from the relation

$$\frac{u_o}{c} = \frac{\sigma}{1 - \sigma^2} \left\{ \left[ \frac{1}{4} + \frac{2}{\gamma} \left( \frac{1 - \sigma^2}{\sigma^2} \right) \frac{\Delta p}{p} \right]^{1/2} - \frac{1}{2} \right\}$$

It is this velocity and the relation for the orifice resistance, i.e.,

$$R = 1.18 \frac{u_o}{c}$$

which takes into consideration the nonlinearity of the strong waves considered.

The steel wool contribution to the resistance was evaluated for a mean velocity between the above orifice velocity and a fully expanded flow behind the wall. The flow resistance for the steel wool was evaluated by the methods given by Beranek (Ref. 9) which account for packing density.

The required admittance,  $A$ , for the muffler configuration presented in Figure 20 is 0.007 to give an attenuation of 10 db.

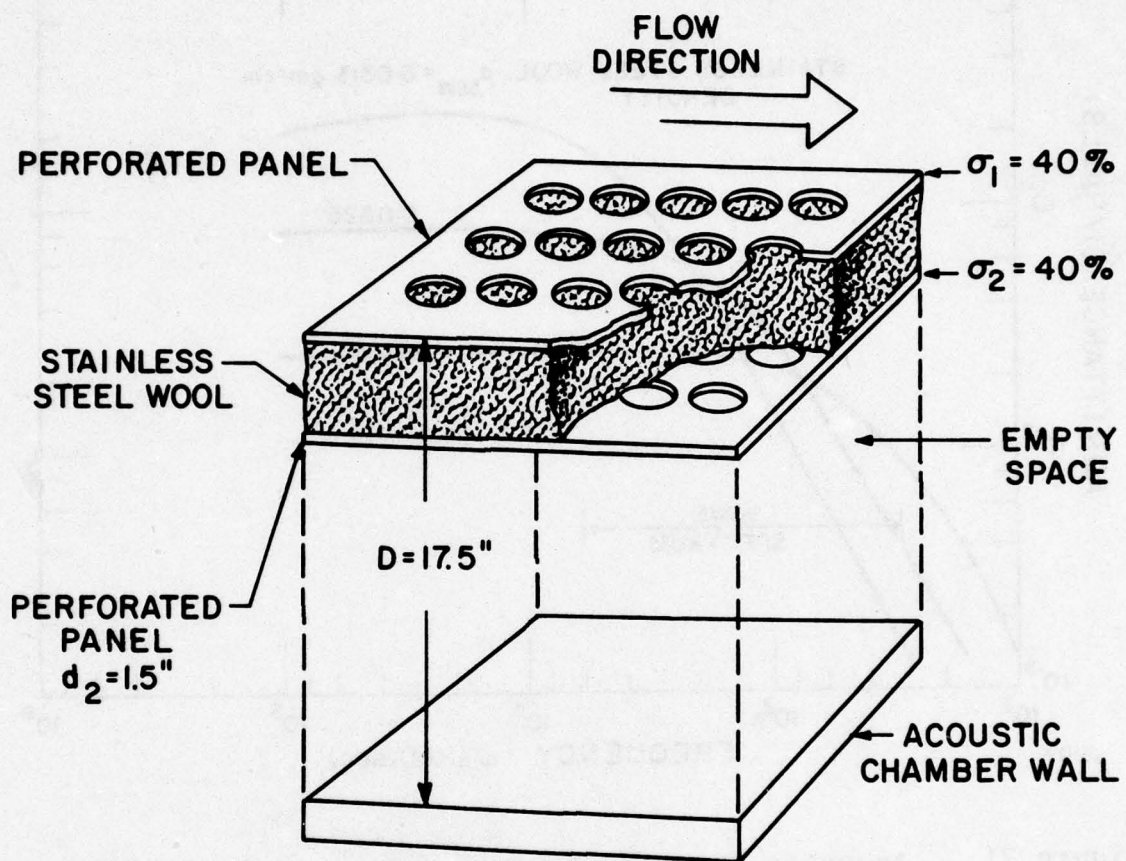
Steel wool packed between the two perforated walls with a density of 0.125 g/cm<sup>3</sup> satisfies this requirement over a broad frequency spectrum (see Figure 21). Further refinements in the acoustic design can be realized by varying the steel wool packing density. Lower densities will give greater attenuation but at narrower bands.

## 6. ACOUSTIC DESIGN SUMMARY

The acoustic suppression system consisting of a passive heat exchanger to minimize the hot gas interface interactions with the generated shocks, and a sidewall muffler of the Helmholtz resonator type to attenuate the shock and strong waves extant can provide the acoustic quieting requirements for a 60 Hz pulse

---

9. Beranek, L.L., "Noise and Vibration Control," McGraw Hill Book Co., 1971.



H4349

Figure 20 Muffler Wall Design

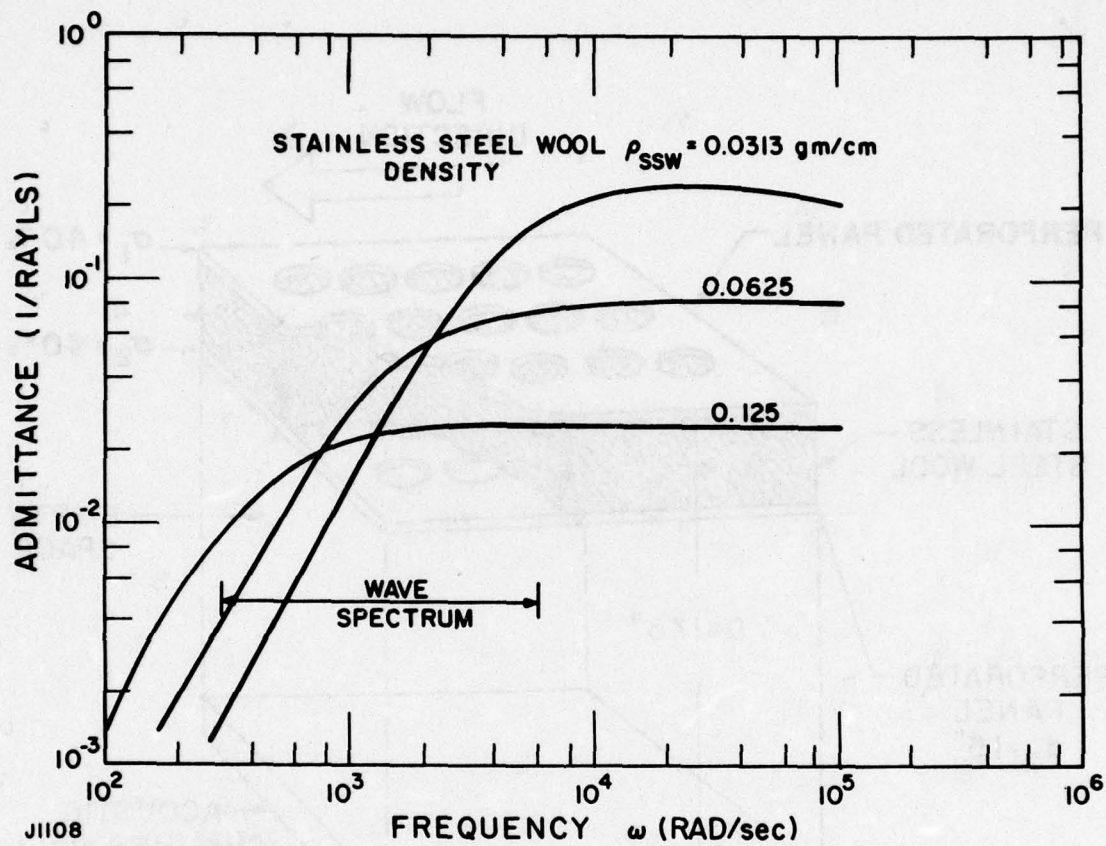


Figure 21 Acoustic Absorber Performance: Required Admittance  
 $= .007 \text{ Impedance db} \approx 1.343 [R(1/2) \rho c . 2 (L/H)]$



repetition rate and gas flush factor of two. Significant attenuation of the initial shock is provided by the heat exchanger as an additional payoff which relieves the muffler and reduces its attenuation requirement. The required attenuation is accomplished in one round trip in the muffler. The reflected waves are indepth which further diminishes their effect on the medium homogeneity (disturbances are correctable steering terms). The attenuation in the heat exchanger is such that the muffler can be more ideally optimized for the strong nonlinear waves which occur late in the intrapulse period. These waves are more difficult to attenuate and are in the low frequency end of the spectrum of interest. The design is flexible in that there are design parameters which can be easily varied to tune the system for the desired performance. These variables include the panel open areas and the steel wool packing density.

## SECTION V

### EXPERIMENT DESIGN AND FABRICATION

#### 1. INTRODUCTION

In 1977 we performed a small-scale flame-out experiment under Contract No. N00173-76-C-0215 in order to develop a scaleable flame-out technique for a repetitively-pulsed chemical laser. This technique was then to be used in order to demonstrate flame-out in a larger device. During the small-scale flame-out development period, it became apparent that scaling the fluidic flame-out technique to a larger size should not provide any major problem since the size of the small-scale device in the flow direction was already the scale desired (30 cm). Furthermore, we demonstrated flame-out with mixtures containing up to 30% F<sub>2</sub> and 8% H<sub>2</sub> at a repetition rate of 60 pps and hydrogen on to off time of two-to-one with our first generation of fluidics. In order to demonstrate flame-out on a large-scale device, it is necessary to increase the laser gas flow cross section by placing more fluidic units and mixer sections side-by-side. With this realization, the program was redirected and the size of a large-scale flow system was selected such that it can be used to experimentally address the remaining key technical issue of acoustic damping. This also required a redesign of the mixer to guarantee high level flow quality and mixture uniformity not required for flame-out. This mixer performance is necessary in order to be in the position to use optical interferometry as the main diagnostics to detect a medium homogeneity of  $\delta\rho/\rho$  better than  $10^{-3}$ . A significant effort was expended on the design and fabrication of the mixer. As it turned out the mixer became a major technological development and consumed a large amount of effort.

#### 2. DESIGN CONSIDERATION

The large-scale device scale and gas flow system parameters were selected in order to perform the acoustic damping on a scale and under conditions such that the result would be meaningful, and applicable to a full-scale device. The length of the device along the optical axis was selected in order to obtain a high sensitivity using standard optical interferometry. The two remaining cavity dimensions were selected to be within a factor-of-two of the dimensions of a full-scale device. The gas flow duration is sufficient to demonstrate acoustic damping for repetitively pulsed operation of about 40 pulses per run.



As stated earlier, the selection of one meter as the dimension along the optical axis was strongly influenced, by data reduction requirements. Furthermore, a device smaller than one meter along the optical axis would not adequately simulate a full-scale chemical laser. Since it would not address the lower frequency acoustic modes, which are the most difficult one to acoustically damp.

### 3. GENERAL EXPERIMENTAL CONFIGURATION

Figure 22 shows the basic experimental layout. The central item is the laser cavity with its optical axis parallel to the laboratory floor at a height of 80 in. This height was selected to assure a convenient access to the acoustic absorber chamber from all sides, including the bottom. The gas flow through the laser cavity, acoustic chambers, and scrubber is horizontal. The laser cavity and gas supply is stationary and permanently connected. The acoustic absorbers can be disengaged and rolled out for inspection and modification. The scrubber location is semi-permanent. Should it be necessary to increase the acoustic absorber length the scrubber can be easily moved to supply the necessary space for a longer acoustic absorber.

The experimental apparatus is installed in a large test cell. A separate control room was built into the test cell and is maintained at a positive pressure to insure that the air in the control room cannot be contaminated should a fluorine leak occur in the test cell. The entire test cell has two ventilation systems. Two large exhaust fans can be actuated to clean out the room should a large leak occur. With fluorine cylinders connected on line, a separated ventilation system exhausts air near the experimental apparatus and from floor level. This air flows through the fluorine storage enclosure. This assures that the cylinders remain at the appropriate temperature and guarantees that heavier gases do not settle near the floor. Should a leak occur in the fluorine storage house the gas is sucked through a large charcoal filtering system capable of handling catastrophic leaks. This assures that large quantities of fluorine do not escape in the surrounding area to be returned into the air supply system of the building.

A gas-control panel is located in the control room. This allows the filling of the various mixing and storage cylinders for the desired gas mixture and run durations. Once the mixture is prepared an automatic control and synchronization panel is armed. The run is initiated and the experiment is cycled through automatically. Various adjustable timers are used to give maximum flexibility. The experiment can be viewed from the test cell through three windows. A television camera and audio system were installed to provide continuous monitoring of the activity in the



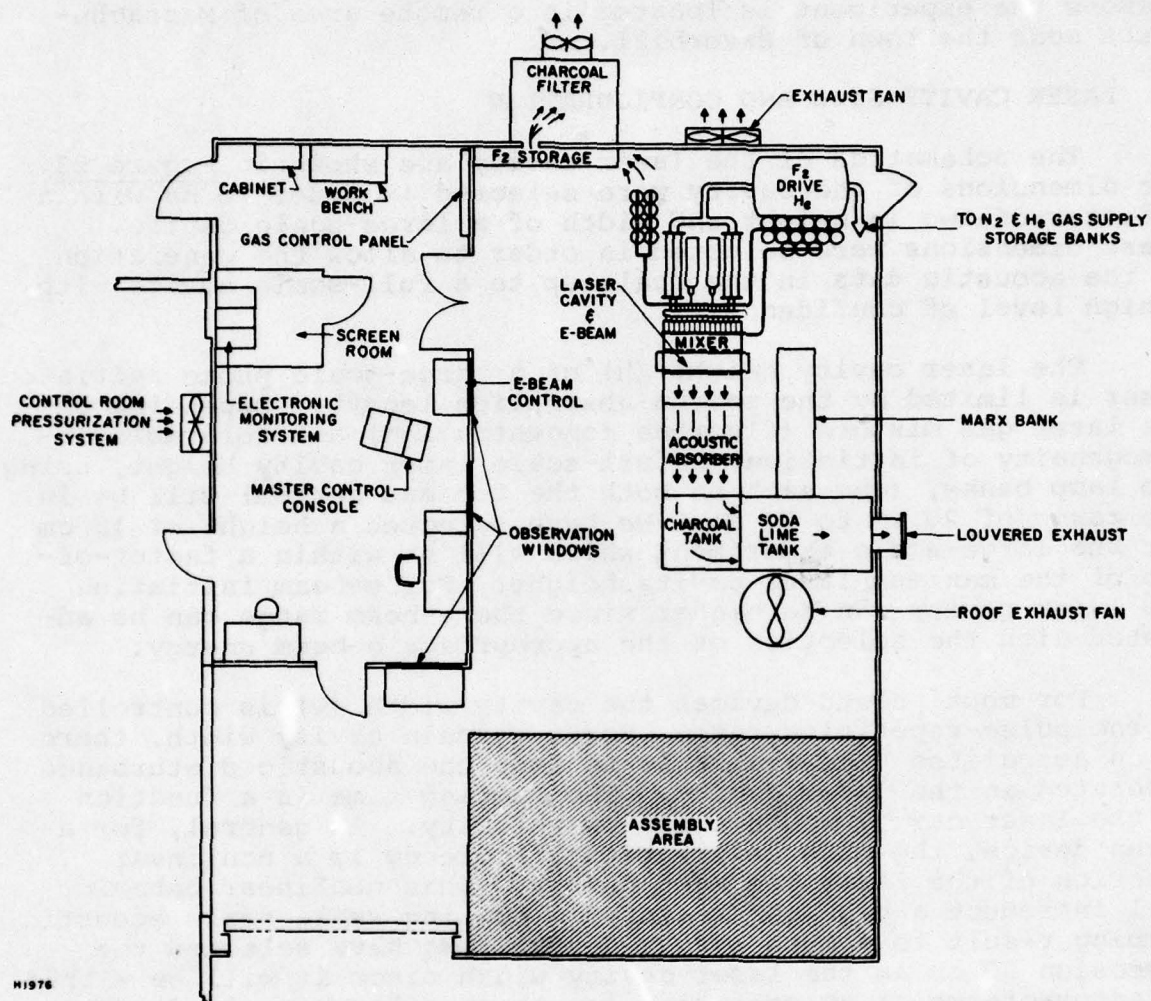


Figure 22 Schematic of Basic Experimental Layout

experimentation area from the remote guardhouse. For safety reasons the experiment is located in a remote area of Massachusetts near the town of Haverhill.

#### 4. LASER CAVITY SIZE AND CONFIGURATION

The schematics of the laser cavity are shown in Figure 23. The dimensions of the cavity were selected in order to be within a factor-of-two in height and width of a large-scale device. These dimensions were selected in order to allow the generation of the acoustic data in the scale up to a full-scale device with a high level of confidence.

The laser cavity height ( $h$ ) of a large-scale photo initiated laser is limited by the photon absorption length. Depending on the laser gas mixture (fluorine concentration) and tolerable inhomogeneity of initiation, a full-scale laser cavity height, using two lamp banks, (one each on both the top and bottom) will be in the range of 20 cm to 30 cm. We have selected a height of 15 cm for the large-scale experiment which will be within a factor-of-two of the maximum laser cavity height. For e-beam initiation the laser cavity can be higher since the e-beam range can be adjusted with the selection of the appropriate e-beam energy.

For most pulsed devices the cavity width ( $w$ ) is controlled by the pulse-repetition rate. For a certain cavity width, there is an associated time available to damp the acoustic disturbance generated in the laser cavity. The damping time is a function of the laser cavity width and flow velocity. In general, for a given device, the mass utilization efficiency is a nonlinear function of the laser gas Mach number. This nonlinear behavior will introduce a high uncertainty in scaling small scale acoustic damping result to a much larger device. We have selected the dimension 30 cm as the laser cavity width since it will be within a factor-of-two of an operating length of a large-scale device. This dimension will also yield a height to width ratio of 1:2 which is close to optimum of a photo initiated device, where the object is to minimize the initiation inhomogeneity and maximize the electrical laser efficiency.

The laser cavity length selection is based on two points. It should be larger than the height or width. Furthermore, it must be of sufficient length such that with the use of standard interferometry techniques the resolution will allow detection of  $\delta\rho/\rho < 10^{-3}$ . From a practical point-of-view, it is desirable to work with a device and an interferometer which produces data on a short turn-around time. AERL has the means to analyze interferograms by optical scanning, digitizing the data and computing the visible fringe aberration coefficients and computing the IR Strehl intensity and integrated farfield irradiance to a resolution



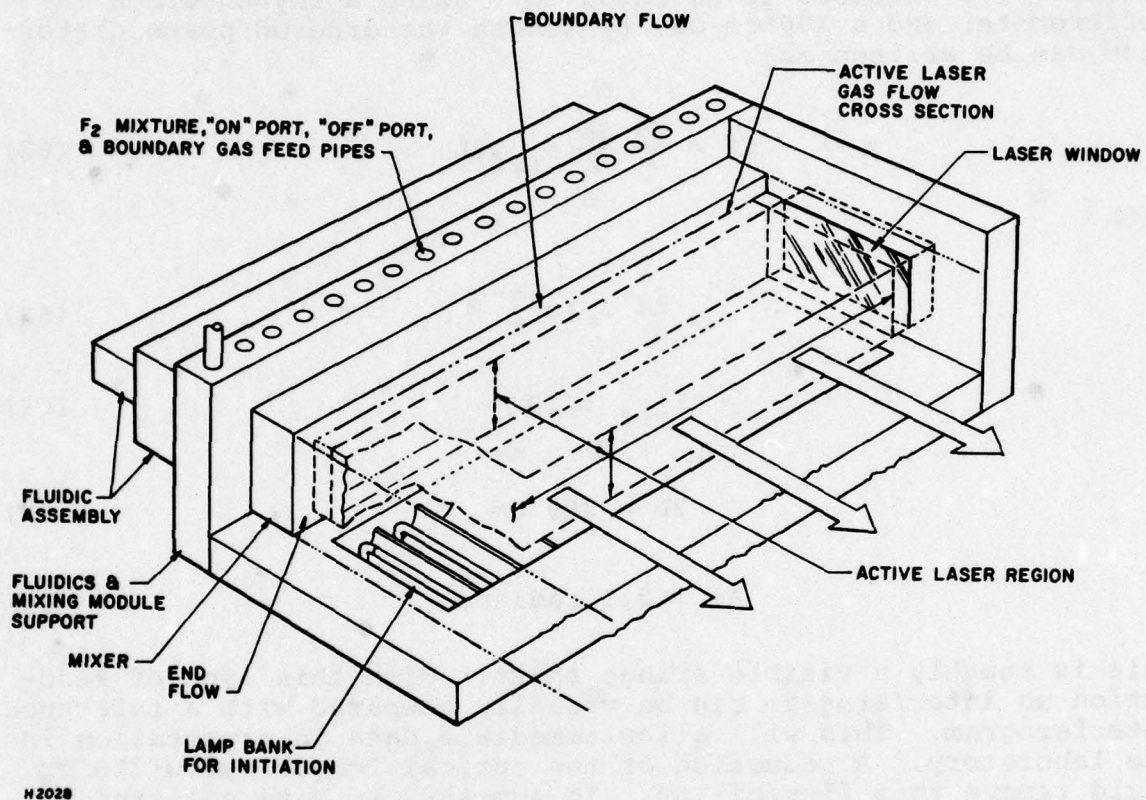


Figure 23 Schematics of Large Scale Laser



corresponding to about a 1/40 or better of a visible fringe. However, this procedure is not convenient when working on the device since it requires processing time too long to allow minor adjustments on the device. Therefore, we prefer to design the systems such that a visible fringe does correspond to the minimum  $\delta\rho/\rho$  required to be resolved. Using a Twyman-Green Interferometer and a 100 cm cavity length the ordered phase distortion can be written as:

$$\Delta\phi = \frac{2\pi}{\lambda} \frac{\delta\rho}{\rho} \beta_{\text{ref}} 2L \quad (62)$$

with

$$\frac{\delta\rho}{\rho} = 10^{-3} \quad (63)$$

$$\beta_{\text{ref}} \simeq 10^{-4} \quad (64)$$

$$2L = 200 \text{ cm} \quad (65)$$

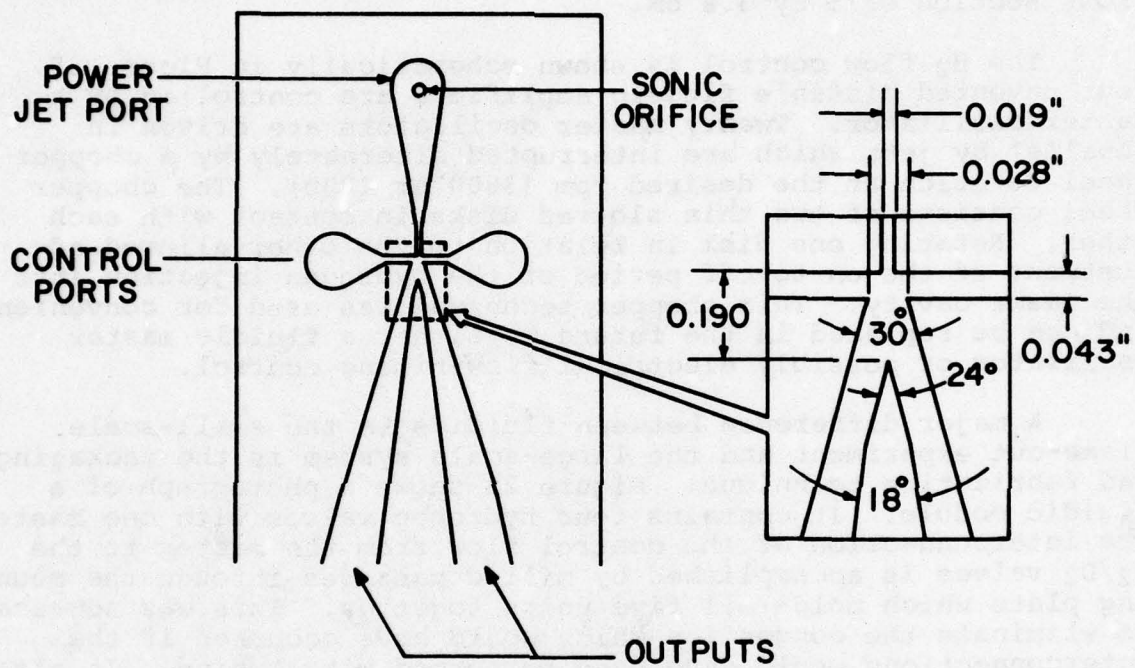
$$\Delta\phi \simeq 2.5 \text{ radians} \quad (66)$$

This is roughly a visible fringe shift. With this type of resolution an interferogram can be visually compared with a reference interferogram. This will allow immediate data interpretation in the laboratory. A reduction of the optical length below 100 cm would remove this flexibility. In summary, we have selected a laser cavity which is 15 cm in height, 30 cm in width, and 100 cm in length with an active laser medium volume of 45 l. We will now discuss the design and fabrication of the various subsystems in further detail.

## 5. FLUIDICS AMPLIFIER DESIGN

In the small scale flame-out experiment, we demonstrated<sup>(2)</sup> flame-out with mixture containing up to 30% fluorine and 8% hydrogen. Non-vented fluidic devices were designed and fabricated to control the hydrogen flow into the laser cavity. The basic configuration of the fluidic device is shown in Figure 24, which is similar in configuration to that for the small scale flame-out experiment. We designed four rows of twenty fluidic devices to control the hydrogen flow for a laser flow cross section of 15 cm by 100 cm. To control an 8% concentration of hydrogen for an active laser cavity width of 30 cm in the flow direction the fluidics must control a total of 7.2 l/pulse of hydrogen if we

## FLUIDIC VALVE - DIMENSION DETAILS



H7277

Figure 24 Master Fluidic Amplifier Design



assume a mass utilization of 50%. With 80 fluidics the requirements per fluidic is .09 l/pulse. We designed the fluidics for volumetric flows of up to 12 to 15 l/sec. Fluidics are thus capable of a maximum repetition rate of 130 to 160 pps. This appears to exceed the mixer design capability.

One fluidic amplifier provides the  $H_2/D_2$  flow for a flow cross section of 5 by 3.8 cm.

The  $H_2$  flow control is shown schematically in Figure 25. Four unvented bistable fluidic amplifiers are controlled by a master oscillator. Twenty master oscillators are driven in parallel by jets which are interrupted alternately by a chopper wheel rotation at the desired rpm (3600 or 1800). The chopper wheel consists of two thin slotted disks in contact with each other. Rotating one disk in relation to the other allowed adjustment of the on-to-off period of the hydrogen injection into the laser cavity. This chopper technique was used for convenience and can be replaced in the future by either a fluidic master oscillator or possibly electrical flow-timing control.

A major difference between fluidics in the small-scale flame-out experiment and the large-scale system is the packaging and fabrication technique. Figure 26 shows a photograph of a fluidic module. It contains four hydrogen valves with one master. The interconnection of the control flow from the master to the  $H_2/D_2$  valves is accomplished by milled passages through the mounting plate which holds all five units together. This was necessary to eliminate the congestion which would have occurred if the interconnections would have been performed with tubing. It also reduces the interconnecting length and, thus, possible switching jitter. The fluidics were fabricated mainly of Lucite with the exception of the power-jet assembly which was made of brass for fabrication and tolerance requirements. We have tested each individual unit to assure that it does meet specifications. This testing included pressure loading of the output port. We used only units which did not flip when loaded to 7.5 psi on the "ON" port and to 5 psi on the "OFF" port. The rejects were reset and retested. Differences in inside wall dimensions of  $< 0.0003$  in. and slight surface roughness were sufficient to effect performance cause rejection. The above backpressure loading should far exceed the performance requirements for the fluidic devices in service. Measurement of mixer performance, which were performed at a later time, showed a steady state backpressure of 0.1 to 0.2 psi.

We performed valve dynamic testing using hot wire diagnostics and fast pressure transducers. The test data show, a switching from full-on to full-off and vice-versa of  $< 0.4$  msec. One device was operated as a self-oscillator by feeding back part of the discharge into the control port. The oscillation frequency



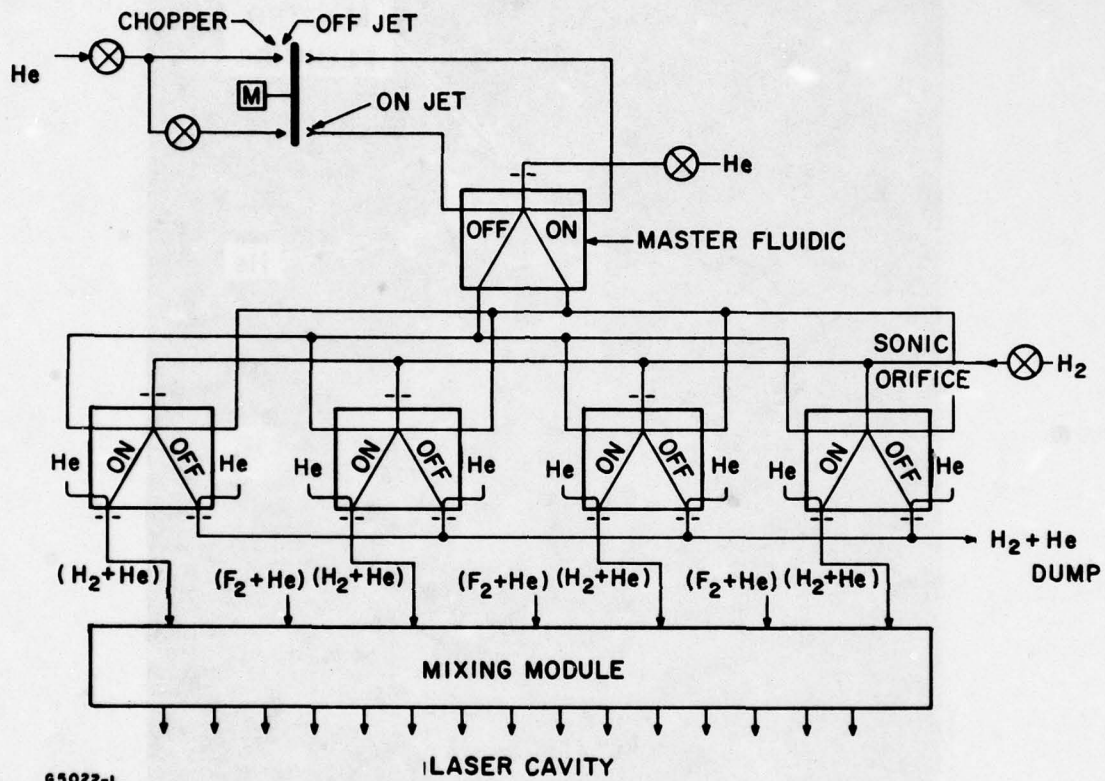
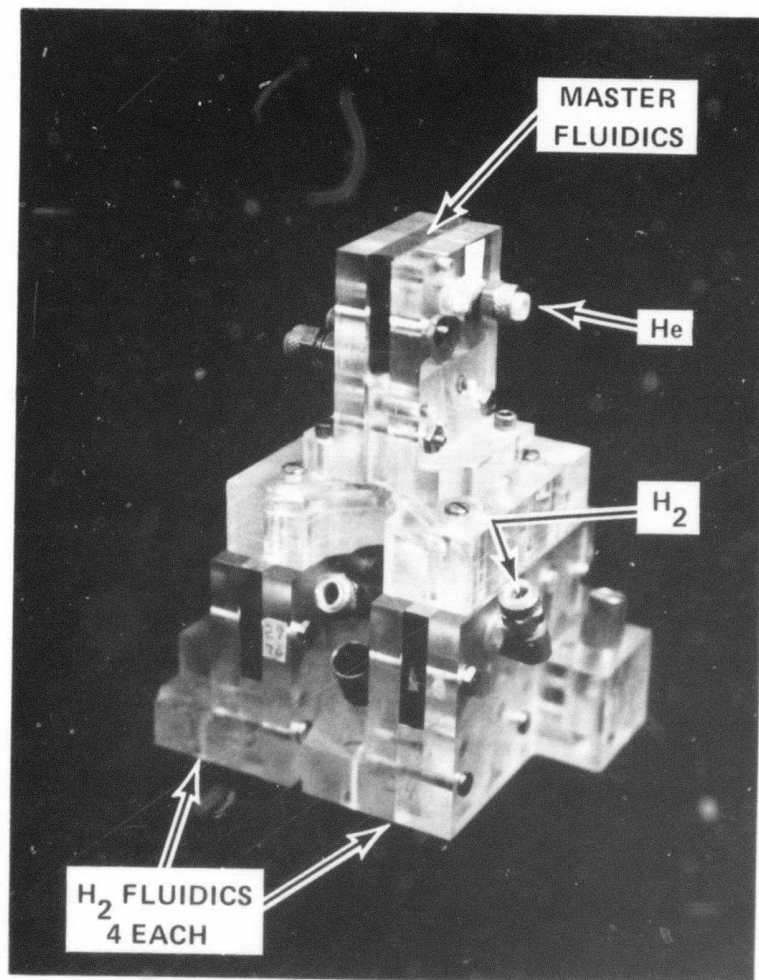


Figure 25 Fluidics Control Schematic



HI969

Figure 26      Photograph of Assembled Fluidics Module for  
Large Scale Device

is governed by the response of the device plus the acoustic transit time through the feedback line. Figure 27 shows the device oscillating at 3.3 KHz using hydrogen as the power-jet gas. In these studies no attempt was made to match the output impedance to that of the receiver. With care the waveform in Figure 27 could be significantly cleaned up. In summary, it appears that the device far exceed the typical projected pulsed-chemical laser operation requirements of 60 to 100 pps.

## 6. MIXER DESIGN AND FABRICATION

The mixer is one of the most important items of a repetitively-pulsed chemical laser system. This stems from the facts that (a) the laser gas had to be mixed at or near atmospheric pressure, (b) the small scale mixture nonuniformity must not exceed a value of the order of 1%, (c) the volume in the mixer up to the sonic gas injection point must be small in comparison to the active laser gas volume, (3) the scale size of the mixer must be such that the turbulence level generated by it will decay to a level such that a minimum optical phase front distortion is obtained in the laser cavity, (e) its construction must be practical with available manufacturing technique, and (f) finally the mixer must be completely compatible with the remaining pulse-chemical laser system.

To build up a repetitively-pulsed acoustic damping experiment it was necessary to fabricate a mixer which conforms as closely as possible to the final mixer specification. In the acoustics experiment a high mass utilization was to be demonstrated, and a good flow medium homogeneity was to be shown by optical laser interferometry.

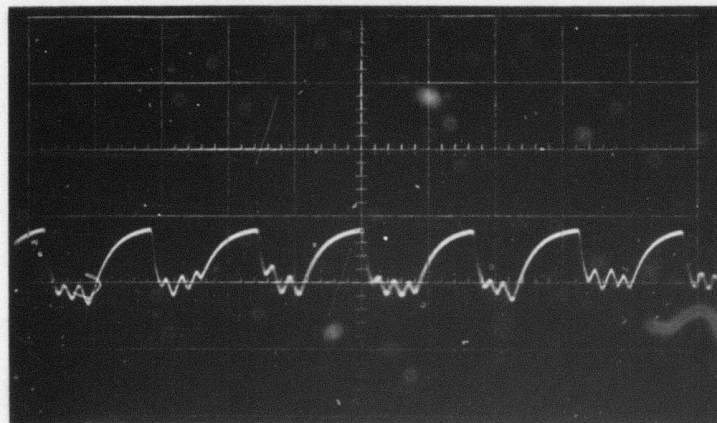
The mixer fabrication took a significant portion of the current program period, since it involved three different specialized fabrication facilities. There were several design modifications necessary to maximize the performance of the mixer, and each modification required a minimum turn around time of 3-6 weeks. Furthermore, the mixer was designed to be suitable to interface with the next generation of fluidics.

The final mixer design selected for the acoustic damping experiment is as follows. Analysis in Ref. 10 indicated that a mixing distance of about 50 L/d is required to obtain a mixture inhomogeneity of  $< 10^{-2}$ , where L is the mixing distance of a tube mixer and d is the inside tube diameter. It was concluded that the fabrication of a tube mixer with necessary compactness was impractical because it would be too costly. Therefore, we

---

(10) Hartung, K.H. and Hiby, J.W., "Comparison of Turbulence Promoters for In-Line Mixing," Paper to the 4th CHISA, Prague (1972).





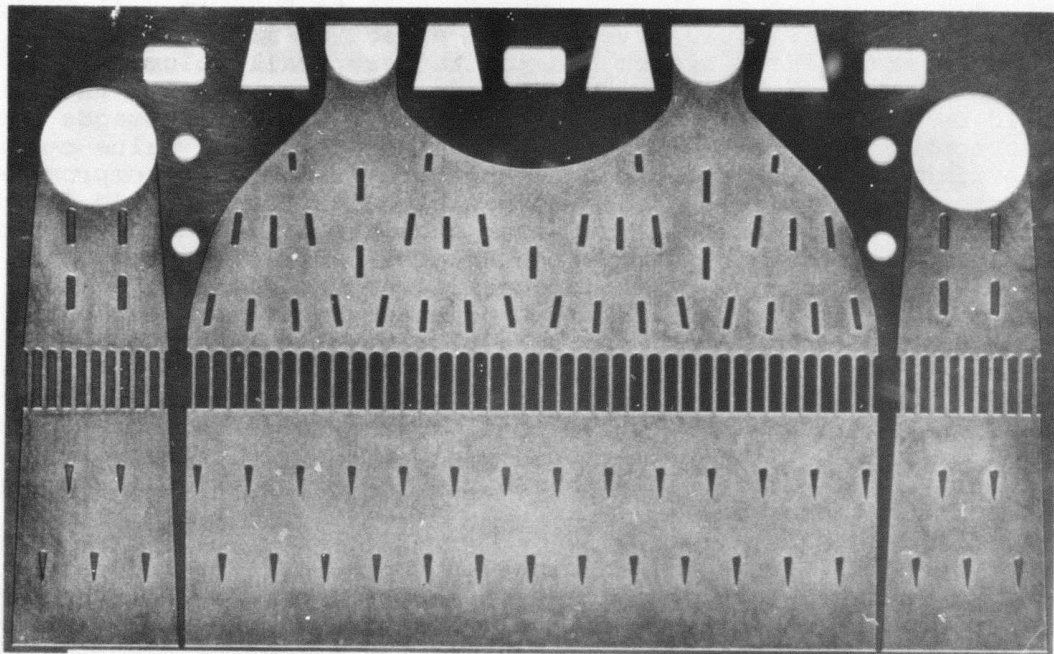
0.2 msec/div

H2640

Figure 27      Fluidics Tests at 3.3 kHz with Hydrogen

selected a plate-mixer construction since small and complicated passages, could be produced using photochemical fabrication techniques to an accuracy of 10<sup>-3</sup> in. This technique will allow us eventually to reduce mixing passage widths to the order of 3-5 mils with mixing distances of the order of 0.15 to 0.25 in. It follows that such a mixer would have minimal effect on mass utilization of the overall laser system due to its very small volume. Furthermore, the amount of hydrogen front spreading through the mixer would be insignificant. The selection of 0.055 in. passages was made to keep the cost of the initial mixer down to a value compatible with the present contract. However, it does not compromise the proof of principle and is compatible with the acoustic damping effort of this contract. The mixer consists of 20 each 5-cm thick modules. Each module is constructed of 15 sets of plates of 3 basic configurations. Mixing occurs in a 5 cm distance between the "A" and "B" plate. The mixing channel and fluorine plenum depth are obtained by etching both plates. The fluorine and boundary flow gas metering orifices are located in the "A" plates only. This approach was selected in order to obtain a suitable open area ratio and a relative small center-to-center spacing between orifices. It, furthermore, yielded a sonic orifice depth to width ratio compatible with the high tolerance requirement and fabrication techniques.

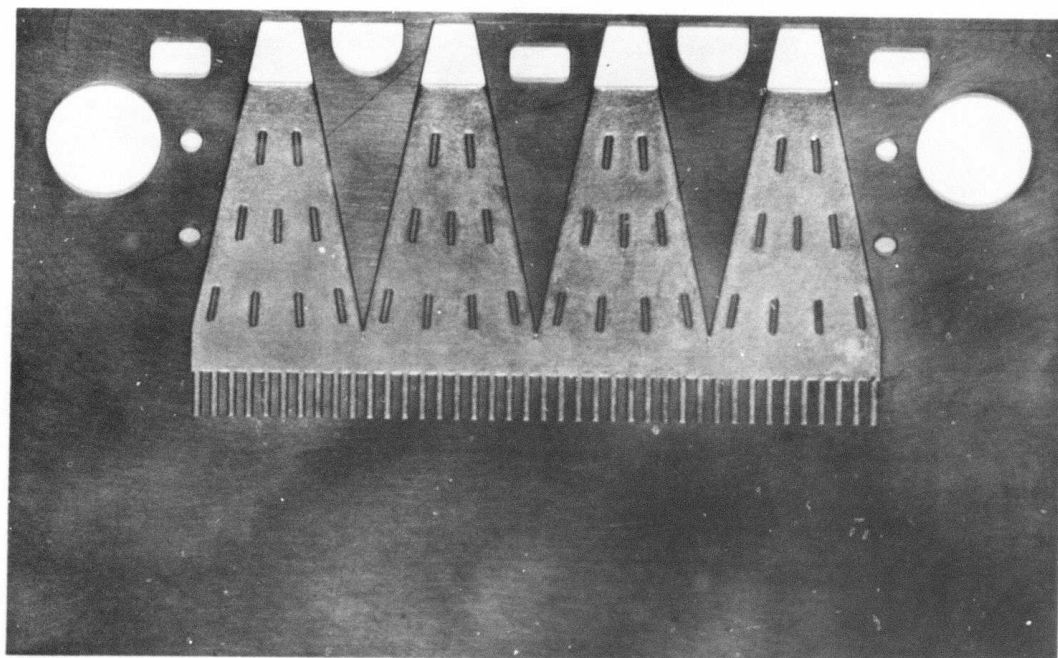
The "A" (Figure 28) fabrication tolerances were closely controlled in order to yield very high accuracy of the orifice depth, orifice width, and orifice channel smoothness. The orifices were required in order to obtain with a limited number of fluorine flow feed points (two in this case) a fluorine mixer mass flow as uniform as possible across the entire distance perpendicular to the optic axis. The sonic injection not only isolated the upstream gas flow section for acoustic pressure disturbances but also increased the initial turbulence level in the mixing region to a high level to aid the mixing process. This mixing principle has been demonstrated by the test data of Hartung and Hiby of Ref. 10. Injection ports line up with each fluorine sonic orifice at the end of a second passage which passes through the "H<sub>2</sub>" plate. This allows the hydrogen helium mixture to pass from the flow passages of the top part of the "C" (Figure 29) plates through the "B" (Figure 30) to the mixing region. The hydrogen-helium mixture is entrained by the fluorine-helium jets. The details of the fluorine control passages of the "A" plate are shown in the upper left corner of Figure 31. The depth and width is 0.015 in. and 0.045 in. respectively; the length of 0.5 in. was selected in order to assure ample bonding surface between the "A" and "B" plates to withstand fluorine mixture plenum pressures up to 90 psi. The islands upstream and downstream of the orifices are employed to maintain the spacings between plates. Similar islands are used with the "C" plate design. The large through passages on the right of Figure 31 are plenums which feed three different gas mixtures into the mixing modules. To provide a 1.5-in. wide boundary flow the sonic orifice control is similarly arranged as for the fluorine mixture.



H2632

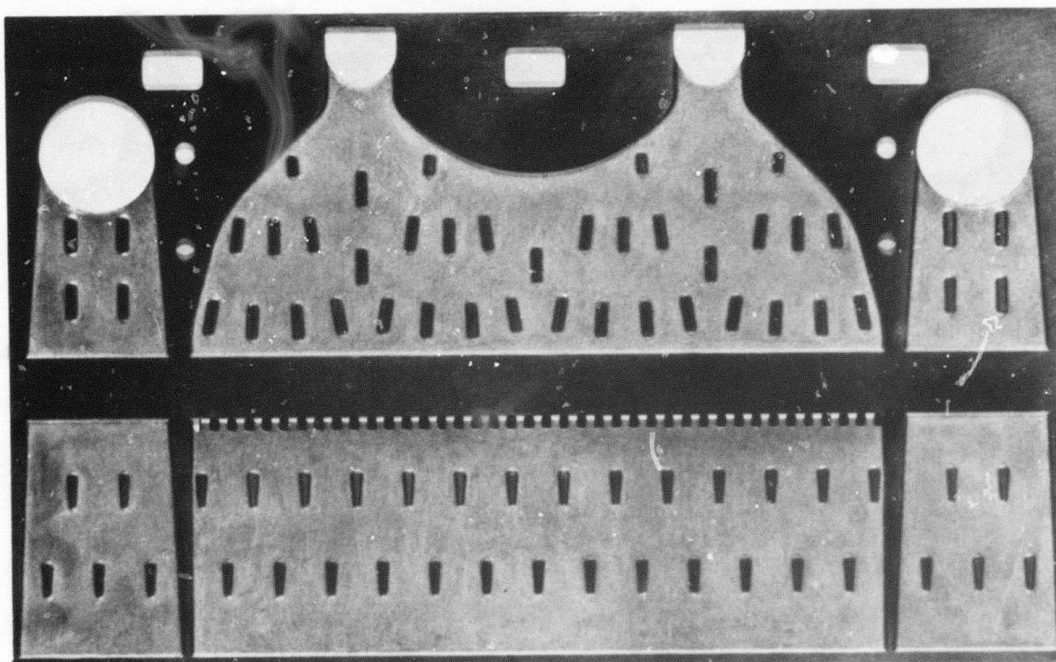
Figure 28      Photographs of the "A" Type Mixing Plate





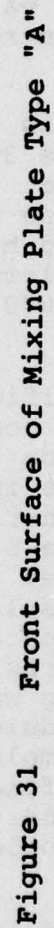
H2630

Figure 29      Photograph of the "C" Type Mixing Plate



H263I

Figure 30      Photograph of the "B" Type Mixing Plate





This can also be seen in Figure 31. The boundary flow utilizes the "A" and "B" plates. The orifices for the boundary flow are larger than those for F<sub>2</sub> + He since for a velocity matched condition the mass flow/unit area for the boundary flow is larger than for the fluorine flow. The smaller openings shown are mounting and alignment holes. To facilitate the functions of each plate the three basic plates ("A", "B", and "C") have in addition four minor variations. The mixing modules were mounted on 2-in. wide blocks which contain the means to supply the three gas mixtures to each mixing module. The gas supply to each plenum is separately controlled with calibrated sonic orifices.

The mixing module plates are fabricated from 316-type stainless steel. They are plated, assembled into 2-in. modules (Figure 32) and welded at the edge to assure precise relative positioning. The modules then were furnace brazed. The division into 2-in. wide mixing sections was performed for convenience of fabrication and handling. The selection of plates using positive and negative tolerances was such that each mixing module was held to a width of 2.040 in.  $\pm$  0.009 in.

The fluorine mixture flow through the channels of the sonic orifice passages were calculated using one-dimensional fluid flow of constant cross section. The friction coefficient was estimated from the surface appearance. On the basis of these calculations the initial dimension were selected and test plates fabricated. Minor modifications to the original dimension were performed on the basis of flow testing. A hot wire scanning technique was used to verify the design and fabrication technique. These test results indicated that optical interferometry is required, as expected, to yield the sensitivity to adequately diagnose the performance of the mixer. For this purpose a complete mixer testing was required. An interferometric test on a single 2-in. module width, with He simulating the hydrogen mixture flow and N<sub>2</sub> simulating the fluorine mixture flow (to increase a large index of refraction difference between the two in order to increase the test sensitivity) showed that within the test sensitivity the design and fabrication technique was sound.

A view of the laser cavity showing the installed mixing modules is shown in Figure 33. The mirror on the left is one of the optics elements used for the interferometry.

## 7. HEAT EXCHANGER

A two-stage acoustic suppression is employed. The first stage has the primary function of minimizing the reflection off the hot/cold gas interface. This section consists of a heat exchanger. The second stage consists of a muffler located downstream of the heat exchanger. In the design of the heat exchanger a compromise between the reduction of the temperature jump across the hot/cold gas interface and the pressure drop through the device was made.

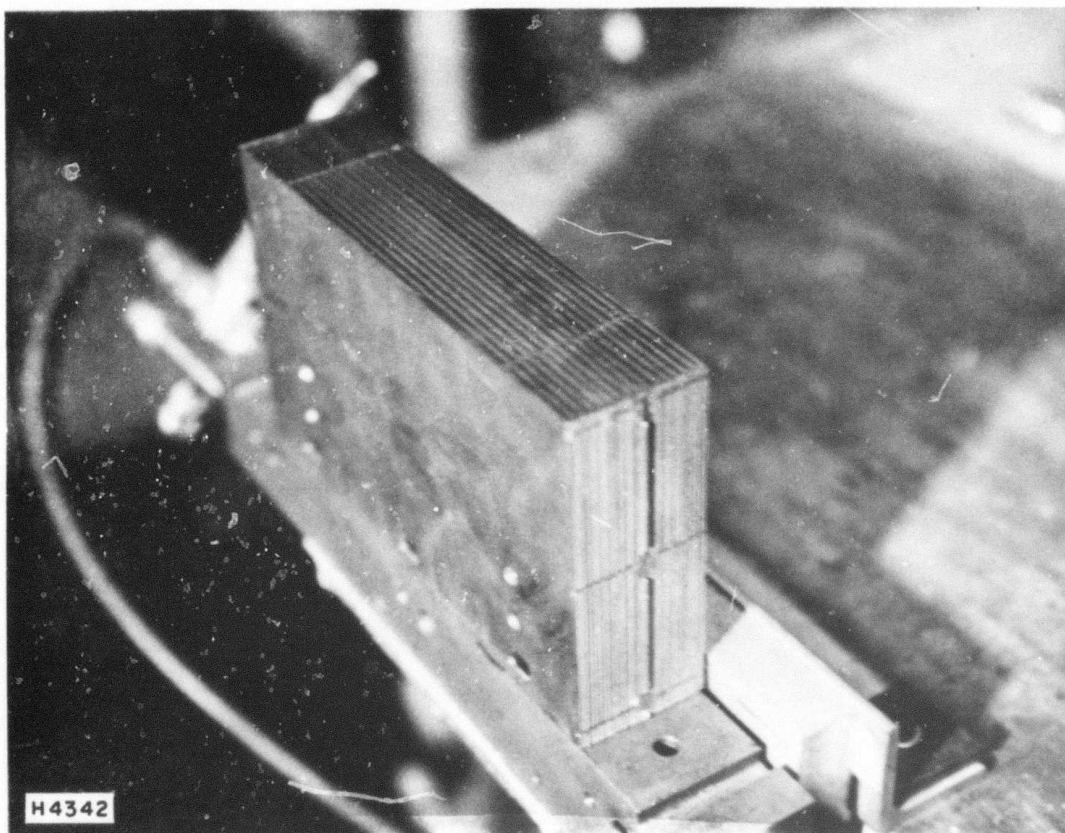


Figure 32      Photograph of 2" Mixing Module Shown Mounted on  
Test Fixture

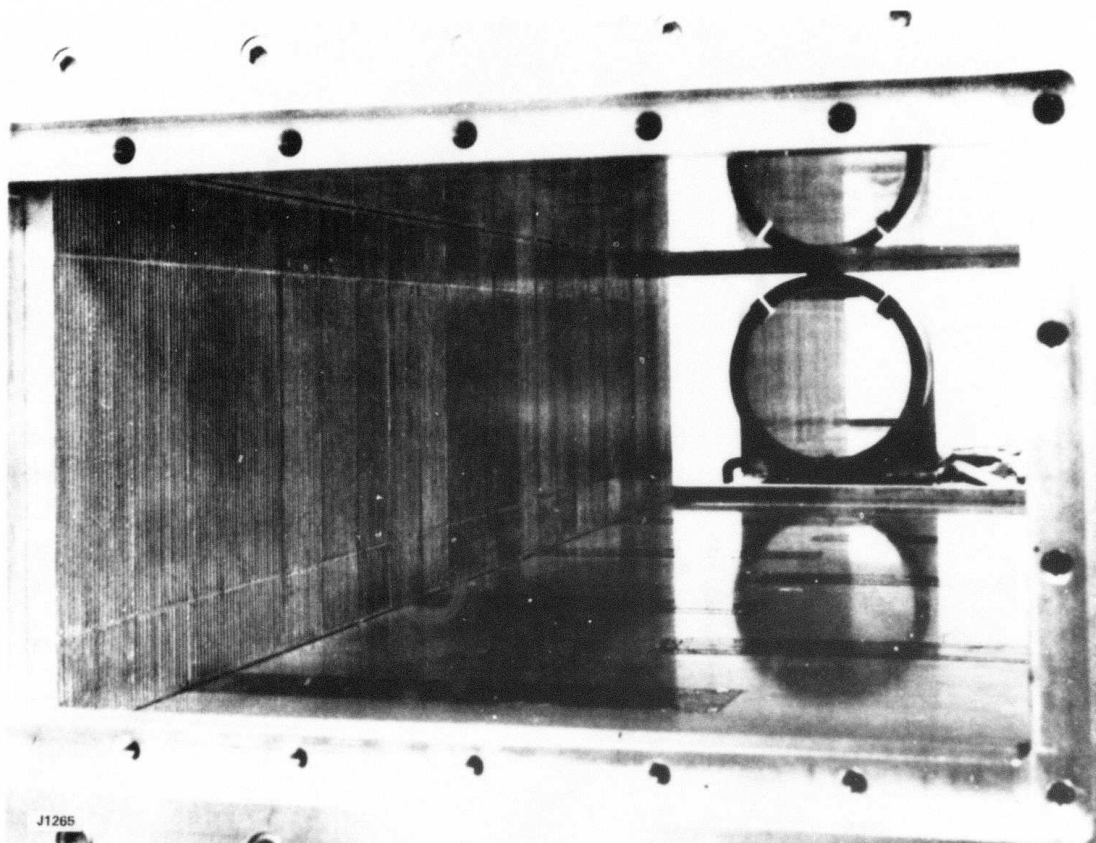


Figure 33      Photograph of Laser Cavity Showing Mixing Module  
Exit. (Flashlamp output windows are shown taped up).



To minimize the reflection of the hot/cold interface the heat exchanger was fabricated out of closely spaced stainless steel fins. According to analysis the fins will reach, after a given run duration, a nearly steady-state temperature near the mean temperature of the cold and warm gas. Heat will be conducted to the cold gas while the hot exhaust will in turn transfer an equal amount of energy to the plate. The net result will be a reduction of the temperature difference between hot and cold gases as well as that across the cold/hot gas interface. The location of the hot/cold gas interface at the time of shock propagation through the heat exchanger will be determined by the amount of heating of the hydrogen free gas slug. The heat exchanger is fabricated of closely spaced stainless steel fins. One out of 8 modules is shown in Figure 34. Gas flowing between the fins remains essentially unidirectional so that the pressure drop through the array of fins is minimal, being caused principally by wall friction effects. At the entrance the fins are staggered such that the closed area reflection occurs over a distance of 5 cm. This is illustrated in Figure 35 which shows the entrance of the heat exchanger. A similar transition over a distance of 15 cm is made at the exit of the heat exchanger (Figure 36) to minimize and spread out negative wave reflection due to an abrupt area change. The minimum length of every fin is 60 cm, while the maximum dimensions of the heat exchanger is 80 cm. The spacing of the fins are designed such that the local structural resonance frequency changes from section to section and is as high as possible. This approach was taken in order to randomize possible reflection of acoustic energy, driven by an structural vibration, over a wide range of frequency. This will cause a minimization of the effective medium inhomogeneity. The fins are fabricated out of 0.015-in. thick stainless steel separated by 0.125-in. spacers. This yields a blockage of about 11%. The spacers are 0.375 in. in diameter with an average separation of 2 in. The spacer blockage is compensated by an additional area expansion (width) of the fins to compensate for the positive reflection.

The top and bottom walls of the heat exchanger are formed by placing 0.125-in. thick bars between fins, thus making them solid spacers. These spacers are in turn fastened together forming a solid support structure for the fins. This solid spacer can be moved out such that the area of the heat exchanger is increasing as a function of the downstream distance. This will allow us to experimentally adjust the open area ratio such that the positive in depth reflection, due to friction in the heat exchanger, can be offset by increasing the open area ratio. For the initial experiment, sidewall spacers are set to increase the open area by 12% over a distance of 60 cm.

Weight of the composite heat exchanger including support structure but not including the external chamber is over 1500 lbs. The fins themselves (the primary elements influencing heat transfer and heat capacity) weigh ~ 450 lbs. Eight modules of 42 fins each are employed to facilitate assembly, and the rods are used to integrate the structure.

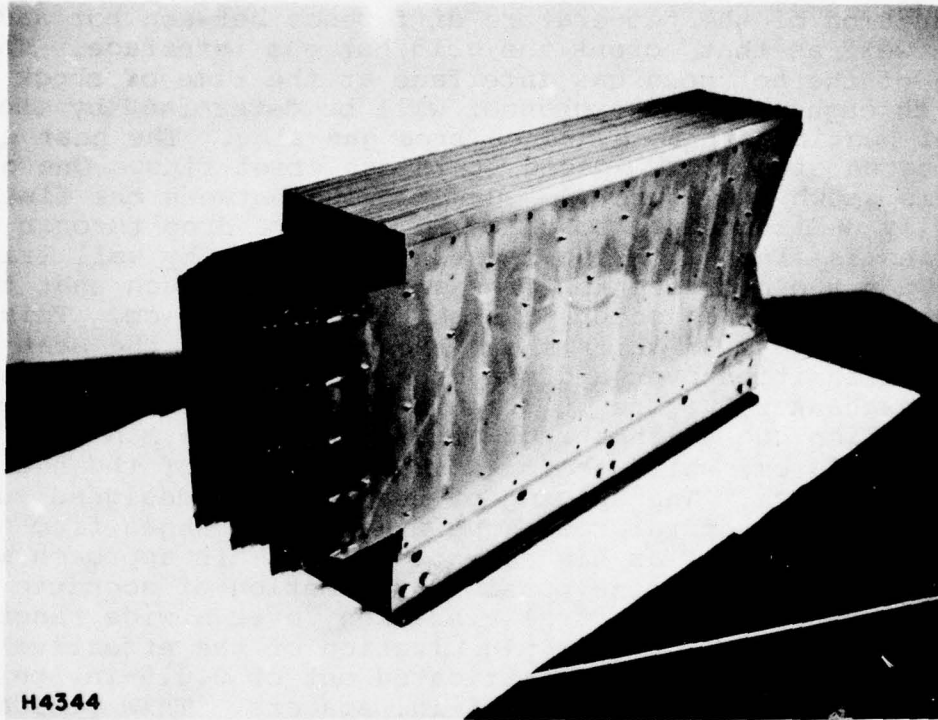


Figure 34      Photograph of One Heat Exchanger Module

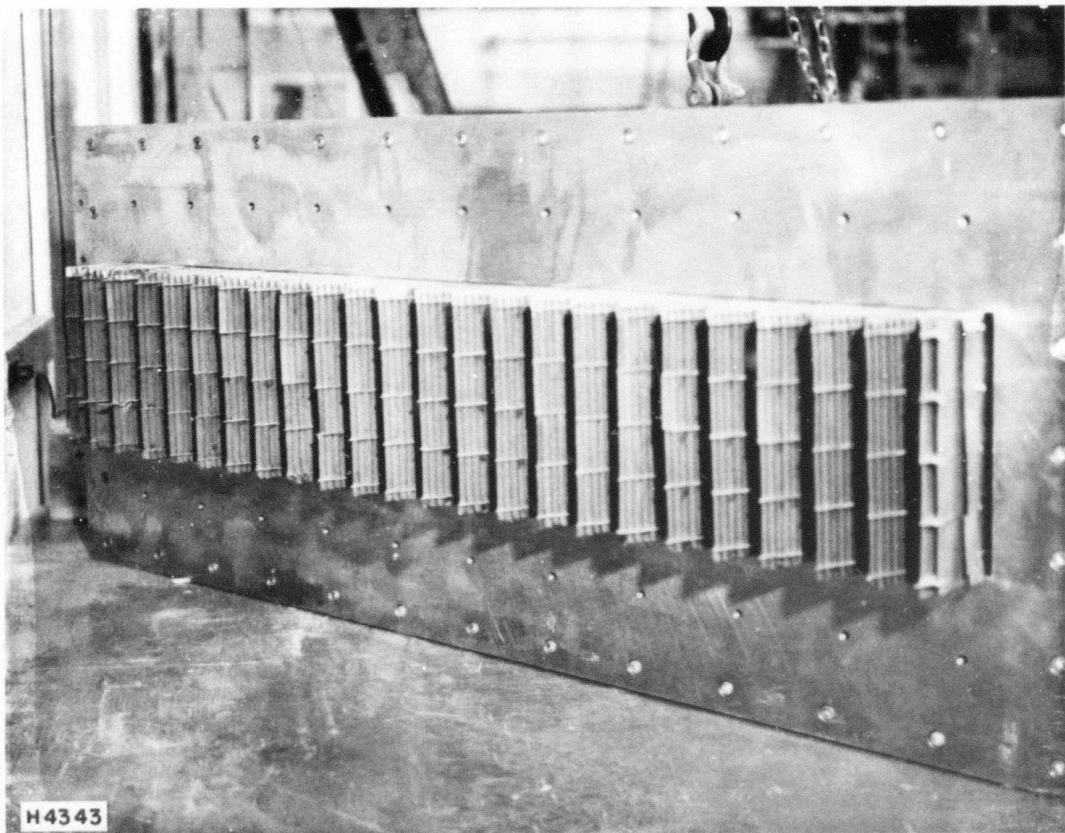


Figure 35      Photograph of Heat Exchanger Entrance



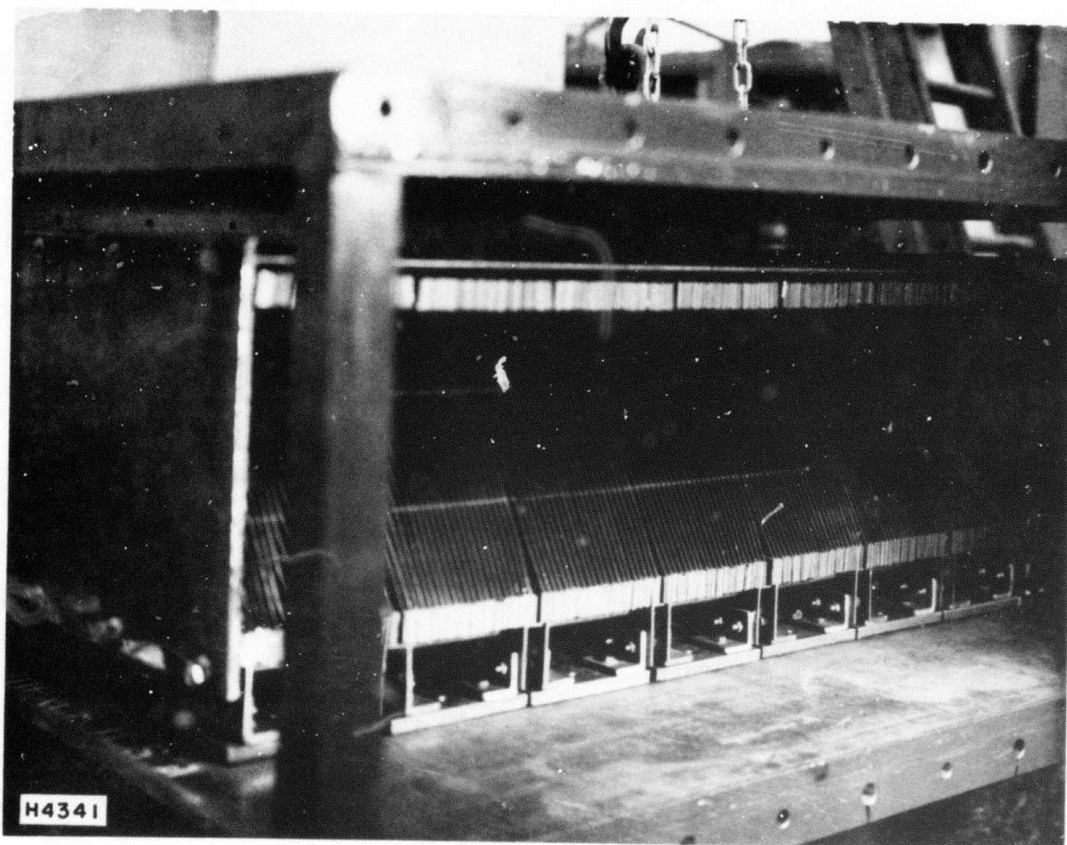


Figure 36      Photograph of Heat Exchanger Exit

The composite heat exchanger assembly is mounted to the box-like steel chamber and is attached at the lower surface only. The nose of the heat exchanger protrudes into the laser cavity to an adjustable distance of as close as 5 cm from the downstream edge of optical volume. The heat exchanger within the acoustic chamber is surrounded by an unused volume such that alternate configurations can be accommodated.

## 8. ACOUSTIC ATTENUATOR

The second stage of the acoustic suppressor functions as a muffler. It has a 210 cm long by 117 cm wide open flow channel, with parallel walls 25 cm apart. The height is slightly more than that of the laser cavity so as to interface smoothly with the downstream end of the heat exchanger.

Edge walls are solid. However the major walls - those of the top and bottom of the channel - are each of a sandwich construction (Figure 20). The inner and outer panels are of 40% open (1/4-in. dia., staggered 3/8 in. centers) 3/16-in. thick perforated steel, nickel plated 1-mil thick for corrosion protection. A coarse grade of stainless steel wool is packed between the panels, with the variables of density and thickness being controlled by amount used and spacers. The actual condition set up employed 2-in. of compressed thickness and 14 kg of stainless steel wool per wall, for a density of about 0.12 gr/cm<sup>3</sup>, which is ~1.55% of that of solid steel.

Wall panels are supported by a 36-cm deep steel grid structure. The grid structure thus forms sets of Helmholtz resonator chambers with each bank of chambers having a volume larger than its predecessor; the smallest cells were ~ 18 cm x 30 cm and the largest were 43 cm x 30 cm (all by 36 cm deep). The outermost dimensions of the resonator chambers were sealed off by steel plates. These chambers are designed such that each one may be reduced in depth in order to change the performance in frequency space. In order to make a gradual transition from the heat exchanger to the acoustic absorber, an acoustic transition section was constructed from petal shaped stainless steel sheet elements. They are fabricated from 0.015-in. thick stainless sheet metal and are riveted onto the perforated panels at their leading edges. The shape for these pieces was determined by the equation

$$y = e^{mx} - 1.$$

Width and length of the petals was 20 cm x 60 cm, so that six pieces covered the width of a wall. The two-edge pieces were trimmed as required to match the 117-cm channel width.

Construction overall was with screws where adjustments might be desired, and welding or pop rivets elsewhere.

This composite assembly was then mounted in "Acoustic Chamber #2," a box-like steel pressure vessel with inside dimensions of 114 cm by 132 cm x 183 cm long. About 25 cm of the assembly protrudes through the leading face of the chamber so as to match up with the trailing edge of the heat exchanger, in "Acoustic Chamber #1." The cantilevered section is supported by U-shaped stiffeners. As this is the section where the transition from solid to perforated walls occurs, echo chambers were not required. The predicted performance of this muffler has been covered in Section IV.3 and is shown in Figure 21.

The acoustic absorber design is such that modification can be performed. For example air can be injected into the resonator chambers. This will yield a continuous flow of cold gas through the acoustic absorber material in order to limit its temperature rise for long run durations.

The injection of room temperature gas may also be necessary since the resonators in the front section of the absorber would become shifted to higher frequencies by increased gas temperature during a longer run. This type of gas injection can be used to optimize the performance of a constructed acoustic absorber since gases with various densities can be injected to tailor the acoustic absorber absorption spectrum without time consuming mechanical changes. Once the optimum point of operation has been determined by this means a simple mechanical change can be performed such that optimum performance is obtained with little or no gas usage.

## 9. GAS SUPPLY SYSTEM

The flow system was designed for a 30-cm long laser cavity to be filled at a repetition rate of 60 pps with the lowest gas utilization efficiency of 50%. This required a laser gas flow velocity of  $3.6 \times 10^3$  cm/sec. Since the active laser volume is  $15 \times 30 \times 100$  cm the flow system has to deliver  $5.4 \times 10^3$  l/sec of gas at atmospheric pressure. This gas is made up of two gas mixtures,  $H_2 + He$  and  $F_2 + He + O_2$ , each having a volumetric flow rate of  $2.7 \times 10^3$  l/sec. The hydrogen flow, controlled by eighty nonvented bistable fluidic devices, is 432 l/sec. This gas is mixed on the "fly" with helium at a rate of  $2.27 \times 10^3$  l/sec. The fluorine mixture is premixed.

A  $He + N_2$  boundary flow gas mixture of 3 cm width is used to assure that the laser is isolated from the top and bottom walls of the laser cavity. With an additional 5-cm wide buffer gas section on both ends of the laser cavity, the laser gas is "boxed" in from all sides and is isolated completely from all solid walls



of the laser cavity. The mixture density and flow velocities of the boundary flow were chosen to minimize mixing between the boundary flow gas and cavity gas. The boundary flow width is designed for 3 cm, however, once we have experimentally determined how large the boundary flow width must be it can be reduced in order to minimize the flow requirements.

Figure 37 shows schematically the gas flow system. Two  $4.5 \times 10^5$  l atm gas storage banks supply the bulk of the laser gases, He and N<sub>2</sub>. Ultra high pure hydrogen is supplied from a standard 1A type cylinder while fluorine is supplied by three 4.9 lb cylinders. The fluorine cylinders are stored in a continuously vented steel enclosure. The venting occurs through a large charcoal filter. The required He and N<sub>2</sub> is stored externally to the experimental area in large banks.

The F<sub>2</sub> and He + O<sub>2</sub> is mixed in two cylinders which contain moving pistons and each have a volume of 40 l. These cylinders are typically operated at a pressure of 15-20 atm. This system has a potential run duration in excess of 1.0 sec. During the flow cycle the fluorine gas is forced out of the mixing cylinders by a large volume (1200 l), constant pressure nitrogen source (see schematic). The required amount of fluorine mixture (dictated by the flow velocity) is delivered at a relatively ( $\pm 10\%$ ) constant pressure which is maintained by the large N<sub>2</sub> drive source. As the piston travel comes to an end, no further fluorine is available, and the flow rate decays. Teflon seals are used to prevent leakage of the drive gas into the fluorine mixture, but as added protection against laser gas contamination, helium may be used as the drive gas. Two fast acting valves, open from full off to full on in 0.03 sec, are used to control the fluorine gas flow. The fluorine mass flow is controlled by the drive pressure and the two calibrated sonic orifices, in series with the fast acting valves.

The 1200 l fluorine drive source is isolated from the fluorine cylinders with large valves. Smaller valves also are used to selectively drive the fluorine cylinder pistons back and forth to increase mixing, prior to a run.

The hydrogen flow requirement is 432 l/sec for a 60 pps operation and a gas utilization factor of 0.5. This gas is provided by a supply system containing between 5000 and 6000 standard liters at a pressure of about 500 psi. A hydrogen storage system is used since it gives us the choice of operating with a large range of hydrogen helium mixtures. This is desirable in order to check out the system at lower hydrogen concentration, while the fluidics are operated at the designed power jet pressure. The hydrogen storage system is also used for lower repetition rate operation, such as 30 pps, where a mixture of 50% He and 50% H<sub>2</sub> is used as the fluidic power jet gas. The mass flow is controlled by the pressure in the hydrogen storage tanks in

# SCHEMATIC OF GAS SUPPLY SYSTEM

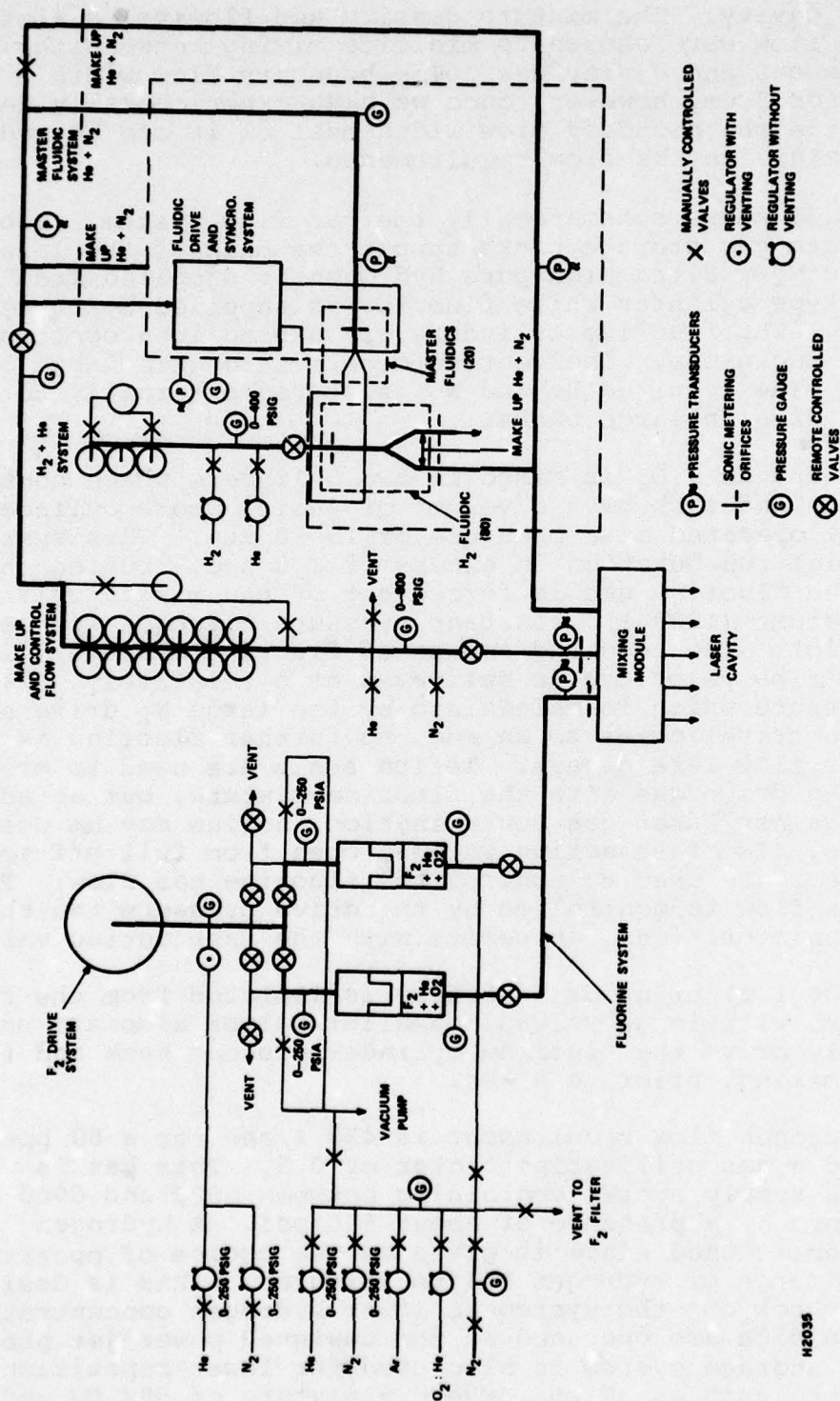


Figure 37 Schematic of Gas Supply System



conjunction with a calibrated sonic orifice. A fast acting valve (10 msec) serves as the turn-on control. The hydrogen enters a manifold at about 100 psi where it is distributed to the eighty fluidic devices. In each fluidic device a matched precision orifice is used in order to assure that each fluidic unit receives the same amount of hydrogen.

About  $2 \times 10^3$  l/sec of helium is required to be injected into the hydrogen "on" ports to complete the hydrogen mixture. The storage capacity is about  $1.5 \times 10^4$  l atm at a pressure of 500 psi. The supply pressure in conjunction with a sonic orifice is used to control the mass flow. The helium injected into the fluidic "on" port is controlled with a series of secondary orifices. A regulator is used to automatically top off the storage tanks from the large helium storage system to the operating pressure.

Helium is also injected into the fluidic "off" port. This supply system is similar to the "on" port injection systems with the exception that only about  $2 \times 10^3$  l atm of helium is stored. The flow requirements are about 103 l/sec.

The helium supply system for the master fluidic power jets is identical to the hydrogen supply system with the exception that its storage size of about  $2 \times 10^3$  l/atm. A flow requirement of about 100 l/sec is required.

The boundary gas supply storage is about  $2 \times 10^4$  l. The gas composition is a mixture of nitrogen and helium to match the density of the laser gas. The flow requirement is  $2.9 \times 10^3$  l/sec. The mass flow regulation system is similar to those as for the other flow systems. The mixture is prepared in the storage cylinders. The gas is allowed to mix by diffusion. The boundary flow is injected into the laser cavity through portions of the mixer assembly.

Figure 37 shows in a simplified diagram the flow system. Pressure transducers are placed to provide a pressure history of each gas supply system. The signals are recorded on a multi-channel strip chart recorder. Each valve can be electrically delayed with respect to the flow system start command. This allows compensation for varying valve speeds and allows preferential gas delays. Dynamic regulators are not used since regulator turn on transients would effect the experiment. Large storage for each gas insures a pressure and mass flow drop of less than 5% for a 0.5 sec run duration

Not shown in Figure 37 is the hydrogen dump line which consists of a 3-in. dia. manifold to which the eighty individual valve dump lines are connected. A 6.0 m long 3-in. dia. pipe is used to vent the hydrogen gas during the off periods to the outside. A 120 liter



accumulator is connected to the dumpline such that the pressure at the hydrogen off port can be raised by means of a throttle valve at the end of the dumpline. This was planned in order to compensate for the pressure drop through the mixer, acoustic absorber and scrubber.

#### 10. MIXTURE INITIATION

For both the flame-out and acoustic damping studies, it is sufficient to initiate the laser mixture at a level such that complete combustion occurs on a time scale shorter than an acoustic transit time through the laser cavity. Such a level of initiation can be conveniently obtained with a few flashlamps.

We had available a dye laser pulse forming network which was designed to operate two 15-cm long lamps at repetition rate up to 250 pps with a lamp energy loadings of up to 5 J/cm. This system was used to demonstrate the small scale flame-out experiments. For the acoustic damping, however, two lamps are not sufficient to uniformly initiate a 1.0-m long laser cavity such that combustion does occur simultaneously over the complete length. For this reason we installed 8 flashlamp systems which were developed under an IRAD flashlamp initiation demonstration program. This was used to trigger the mixture sufficiently uniformly but relatively weakly, such that no significant lasing does occur to effect the high quality quartz windows needed for optical interferometric diagnostics. The two repetitively triggered flashlamps form the hot/cold gas interfaces downstream in the laser acoustic absorber section. This in combination with the triggered flashlamp bank allows one to study flame-out and acoustics. The wave clearance study was performed following the triggering of the eight-bank system.

To insure that large quantities of explosive mixtures do not accumulate downstream of the laser cavity, we installed six glow plugs at the entrance of the heat exchanger. This assured the triggering of combustion for the case where the mixture was not initiated by the correct operation of the lamps.

With either the two repetitively triggered flashlamps or the six glow plugs any given number of complete laser fillings can be initiated such that the appropriate cold/hot interfaces are generated downstream in the heat exchanger and acoustic absorber. For testing the acoustic absorber system performance, the bank of eight lamps are used to initiate relatively uniformly and sufficiently strongly such that "instantaneous" combustion occurs throughout the active laser volume. The optical interferometric diagnostics follow this initiation.

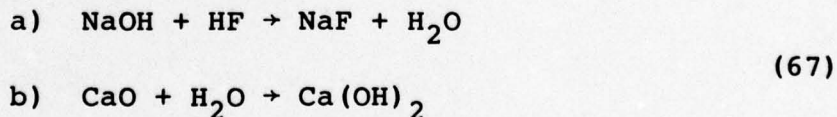
The flashlamp circuit is shown in Figure 38. Each lamp has its own capacitor (0.01  $\mu$ F) and spark gap. Sparks were originally used for the IRAD photo initiation investigation in order to reduce the inductance to a minimum for laser application. The spark gap and capacitor are mounted in a coaxial configuration and are connected to the lamps through a coaxial cable again to minimize the inductance. Figure 39 shows the components for the spark gap - capacitor assembly. The lamps are U-shaped and are mounted in an aluminum plate with continuous water cooling capability. The construction has a low inductance and results in a very short flashlamp pulse  $\leq 1 \mu$ sec as can be seen from a photo multiplier output in Figure 40. This low inductance initiation was not necessary for the acoustic damping study, but was used since it was a developed and functioning assembly from prior work. The bank of 24 flashlamp drivers is shown in Figure 41. At this time, only eight of these are used. The flashlamp windows consist of 1/4-in. thick quartz plate, mounted flush with the laser sidewalls.

#### 11. GAS SCRUBBING SYSTEM

The laser exhaust is passed through a 4-ft deep charcoal bed to burn off a large portion of the excess fluorine to form  $\text{CF}_4$ . A second 4-ft absorber containing soda lime crystals scrub the remaining fluorine and  $\text{HF}(\text{DF})$ . The scrubbed gas is then exhausted to the atmosphere. Figure 22 shows the location of the scrubber in relation to the total experiment.

This type of scrubber was selected since it allows us to operate the laser cavity at nearly atmospheric pressure. Furthermore run durations are practically unlimited. It also appeared to be the most cost effective means of scrubbing the pulsed chemical laser gas in a laboratory setting.

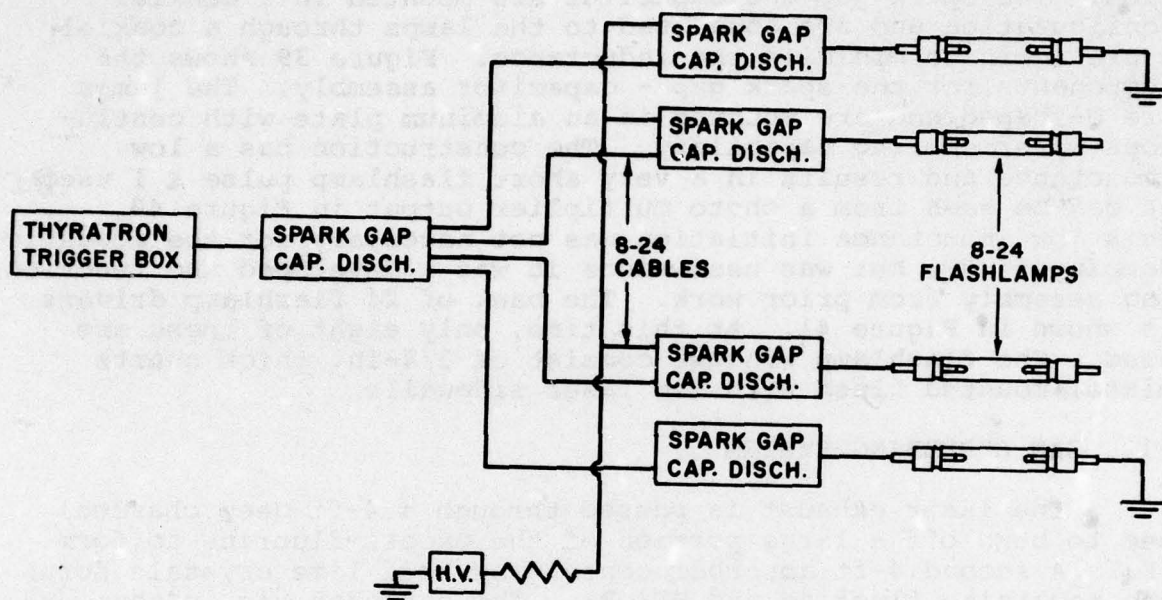
The chemical reaction of  $\text{HF}$  with soda lime forms sodium fluoride as given by



A flow test has been performed to test the soda lime absorption performance of  $\text{HF}$ . It can be best described by the exponential decay with distance.

$$[\text{HF}] = [\text{HF}]_{x=0} \text{EXP}[-x/x_0] \tag{68}$$

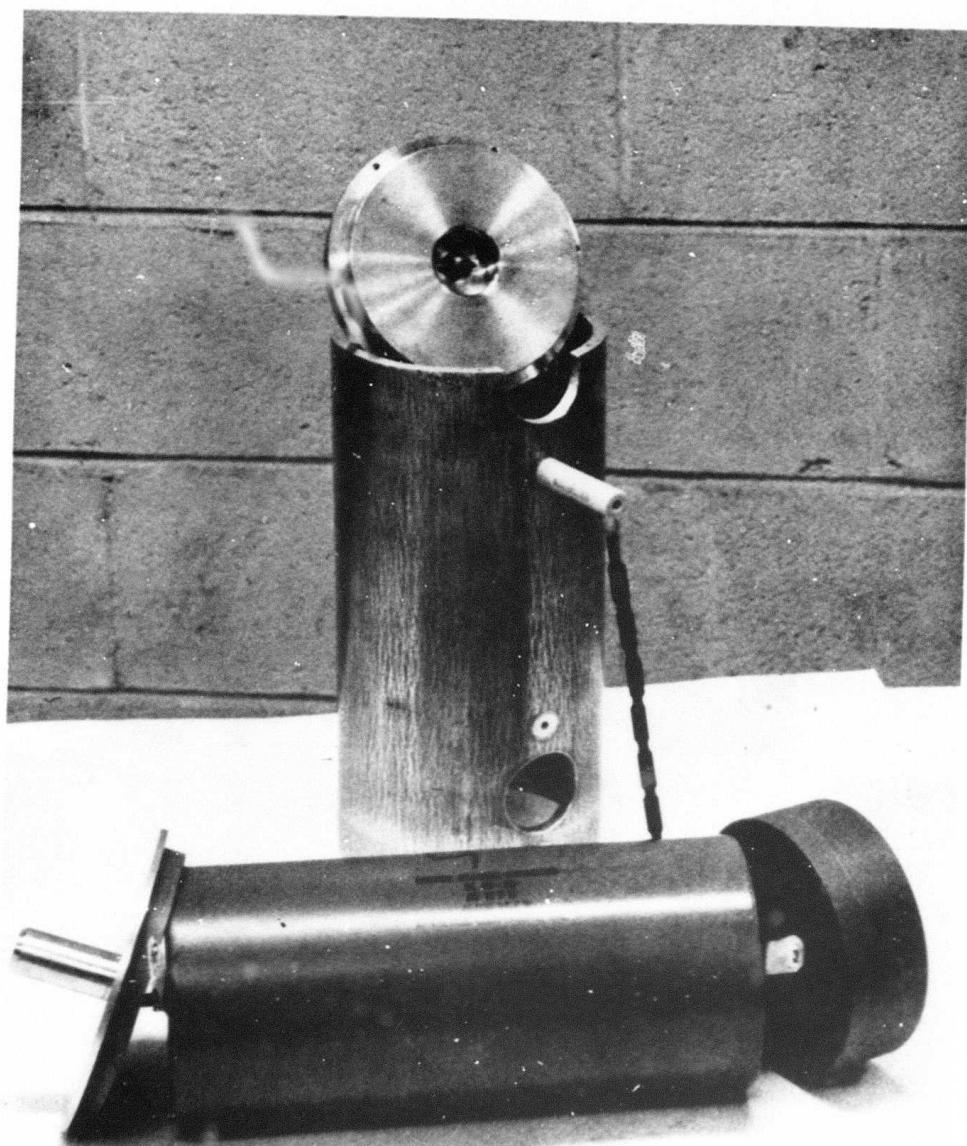




E6176

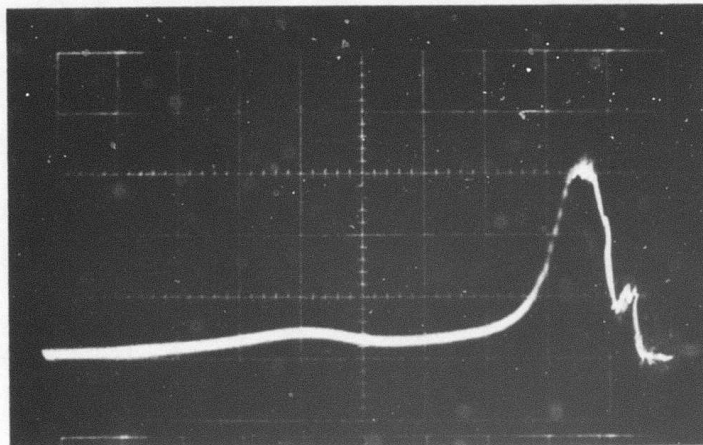
Figure 38 Schematic of Flashlamp Circuit





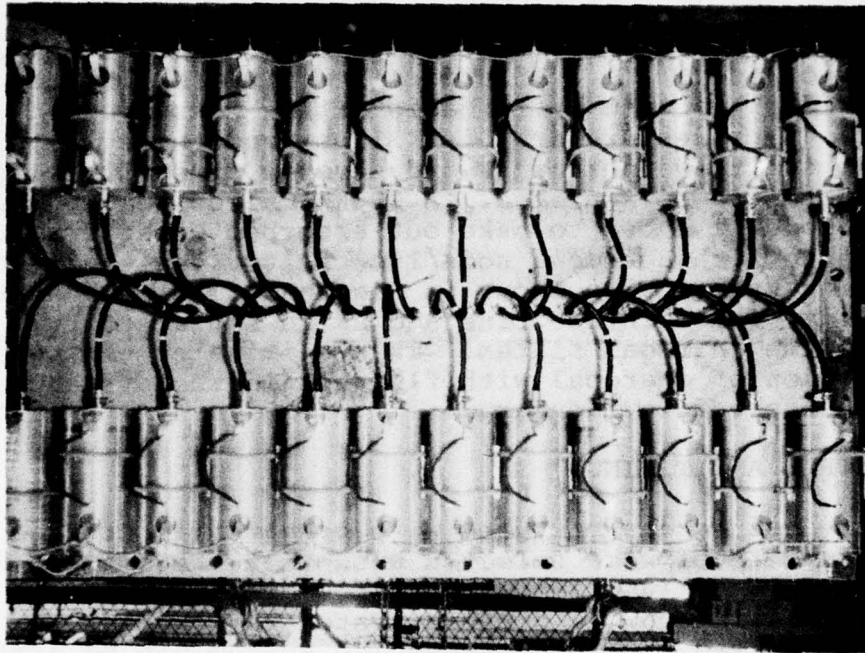
J1253

Figure 39      Photograph of Spark Gap and Capacitor Housing Components



H9286

Figure 40      Polaroid Trace of Photomultiplier Signal Measuring  
the Flashlamp Output at a Sweep Rate of  $0.5 \mu\text{sec}$   
per Division



H9285

Figure 41      Photograph Showing 24 Low Inductance Capacitors and Spark Gaps in Housing Assemblies



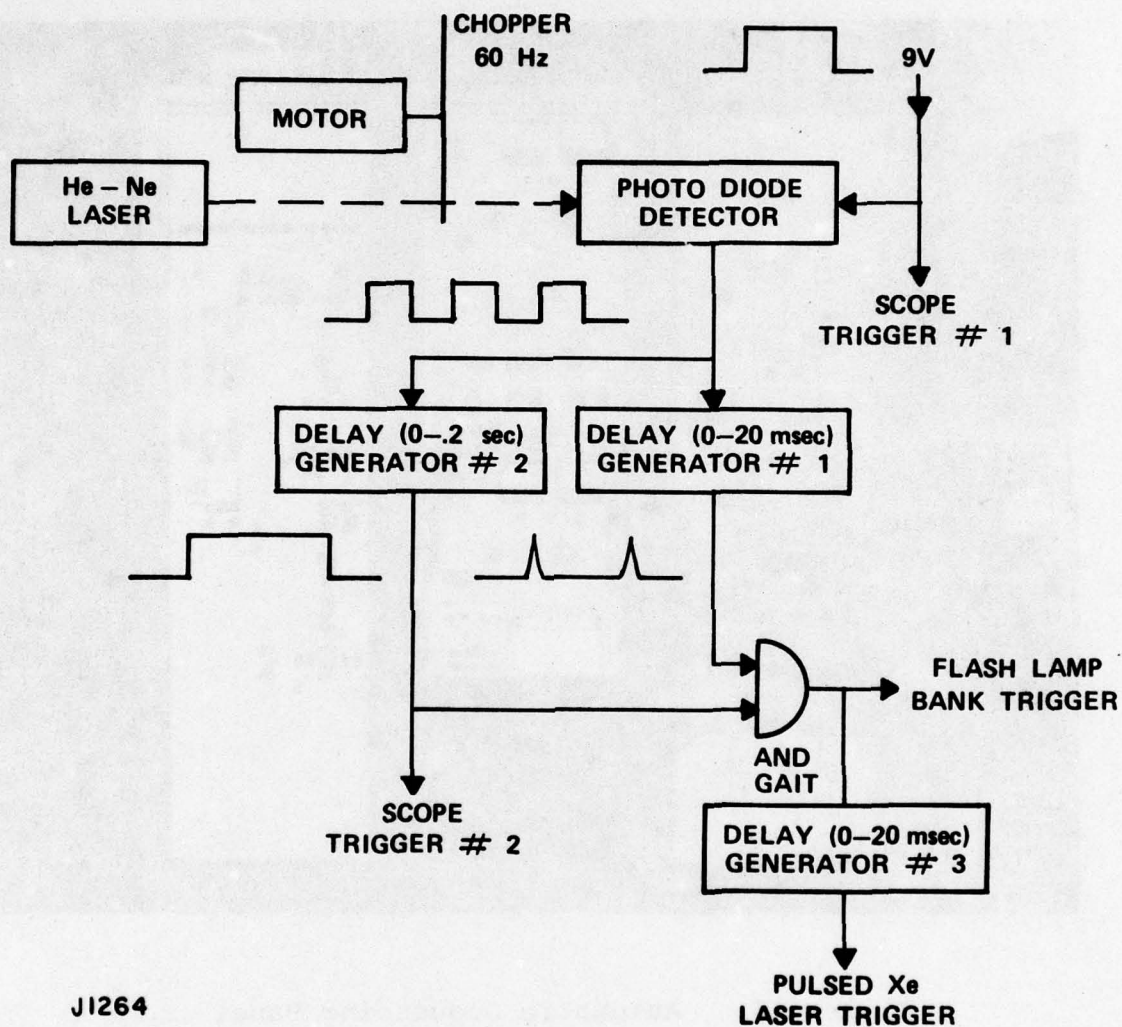
where the absorption length  $x_0$  is a strong function of the flow velocity. For a velocity of  $10^3$  cm/sec the exponential absorption length is about  $x_0 \approx 3$  cm. This indicates that in about 20 cm of absorber material the HF concentration should be down to an allowable  $10^{-4}$  value.

This scrubber system contains about a ton of charcoal and four tons of soda lime. This massive volume allows the flow to be operated on an open cycle basis with a mass flow in excess of 5 lb/sec. The pressure drop is  $< 1$  psi and the system can absorb about 20% of its weight of HF and several times its weight of  $F_2$  before it has to be replaced. A 20 kW Calrod heater was installed into the soda lime bed to bake out absorbed water from time-to-time. Tests with a second soda lime filter for the fluorine storage filtration system, also shown in Figure 22, have shown that the use of soda lime for both fluorine and HF is satisfactory. Thus we may eliminate the charcoal filter. This eliminates the possible explosive reaction of charcoal with fluorine in the presence of air as has been observed in industry.

## 12. CONTROL AND TIMING

The desired gas mixtures were prepared in storage cylinders and pressure level were selected such that the correct mass flow is obtained in conjunction with sonic metering orifice. Once this gas handling and diagnostic system is checked, the automatically controlled flow and sequencing system can be armed. This requires the closure of many interlocks for both safety and correct operating conditions. The control system consists of timing and sequencing systems to operate at selected times the remote controlled valves, flashlamps, and the diagnostics. Each gas turn on can be conveniently delayed with respect to the others. For the laser gas flow and purge system, relay delay logic is used. For the lamps and diagnostic trigger electronics, delay logic is employed. In Figure 42, the flashlamp trigger logic is shown. A chopped He-Ne laser signal is picked up by a photodiode in order to validate the time of the optical interferometric observation. The control console located in the control room is shown in Figure 43.

This chopped signal synchronizes the fluidics operation with the electronics. The photodiode in conjunction with the 6 V dc signal from the valve sequence functions as an END gate such that the first lamp trigger pulse occurs after the flow is established. The lamp triggers in relationship with the location of the hydrogen containing laser mixture position and is adjusted with the delay generator No. 1. Delay generator No. 2 serves to select the triggering of the large flashlamp bank. With this delay and the END gate, the Nth Hydrogen containing mixture is selected.



J1264

Figure 42 Electrical Schematic of Flashlamp Initiation System

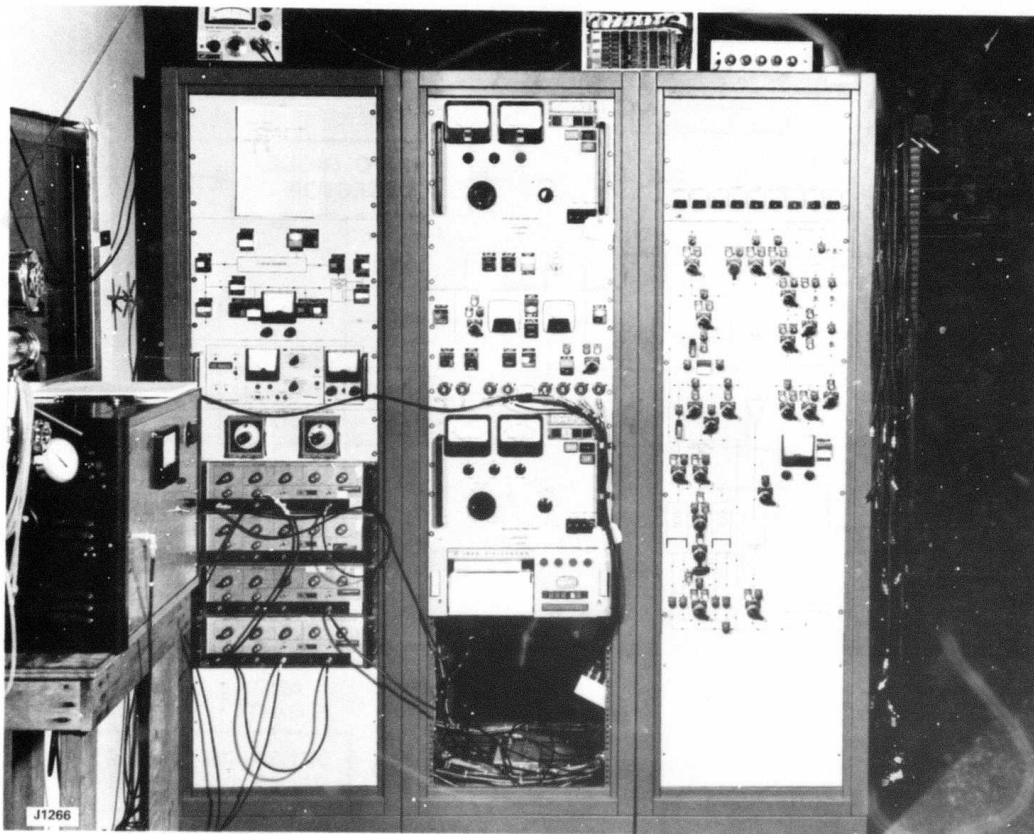


Figure 43     Automatic Sequencing Panel



Delay generator No. 3 serves to delay the pulsed Xe laser, which is used for the optical interferometric data generation, in relationship to the laser mixture initiation. The scope trigger signal No. 1 is used to record the flame-out data (fluorine absorption signal) and pressure transducer signals, while trigger No. 2 is used to assure that the pulsed Xe laser is triggered at the correct time.

### 13. DIAGNOSTICS

#### a. Interferometry

Interferometry at visible wavelength is utilized to diagnose the IR fringe aberration  $F(x,y,t'_N)$ . The one-pass IR fringe aberration  $F'(x,y,t'_N)$  is related to the measured visible fringe aberration  $V(x,y,t'_N)$  by

$$F'(x,y,t'_N) = (1/\alpha_{\text{vis}}) (\lambda_{\text{vis}}/\lambda) (\beta/\beta_{\text{vis}}) V(x,y,t'_N) \quad (69)$$

where

$\alpha_{\text{vis}}$  = number of optical passes of visible interferometer

=  $\begin{cases} 1, & \text{Mach-Zehnder interferometer} \\ 2, & \text{Twyman-Green interferometer} \end{cases}$

$\lambda_{\text{vis}}/\lambda$  = ratio of visible to IR wavelengths

$\beta_{\text{vis}}/\beta$  = ratio of visible to IR Gladstone-Dale coefficients

$V(x,y,t'_N)$  = visible fringe aberration (vis fringes)

The interferometer used for diagnostics is a Twyman-Green (two-pass) configuration rather than the Mach-Zehnder (one-pass) configuration since it gives a gain in sensitivity of a factor-of-two. The beam quality requirement when expressed in terms of measured visible fringes, reduces to

$$V_{\text{rms}} = F_{\text{rms}} \times \frac{\alpha_{\text{vis}}}{\alpha_{\text{eff}}} \times \frac{\lambda}{\lambda_{\text{vis}}} \times \frac{\beta_{\text{vis}}}{\beta} \leq 0.51 \text{ rms vis fringes} \quad (70)$$

where

$$F_{\text{rms}} \leq 7 \times 10^{-2} \text{ rms IR fringes}$$

$$\alpha_{\text{vis}} = 2.0$$

$$\alpha_{\text{eff}} = \begin{matrix} \text{effective number of passes in unstable resonator} \\ \approx 2 \end{matrix}$$

$$\lambda_{\text{vis}} = 0.526 \text{ } \mu\text{m}$$

$$\lambda = 3.8 \text{ } \mu\text{m}$$

$$\beta_{\text{vis}}/\beta \approx 1.0$$

The mean peak to valley vis fringes corresponding to 0.51 rms vis fringes is  $2\sqrt{2} \times 0.51 = 1.44$  p-p vis fringes. Therefore, if the interferometer with data reduction is capable of a resolution of at least 0.5 vis fringes, the Strehl intensity uncertainty  $\delta S = \pm 0.02$ . [ $\delta S = (\Delta V/V)^2 \Delta S = (0.5/1.44)^2 \times 0.17 = 0.02$ ]. For a beam quality design goal of  $S \leq 0.17$ ,  $\delta S = \pm 0.02$  corresponds to a Strehl intensity measurement error of 12%. The use of a one-pass interferometer, with the same vis fringe resolution capability, would result in a Strehl intensity measurement error of 48%.

A schematic of the Twyman-Green interferometer is shown in Figure 44. The interferometer utilizes a laser source whose output beam is near diffraction limited so that a spatial filter at the focus of the expander lens is not required. The expander lens and collimating lens serve to expand the beam to the test cross section of the cavity. The beam is split into two paths by the beam splitter and transmitted approximately equal distances (within the coherence length of the laser source) to the reference and return mirrors where the beams are reflected back to the beam splitter and then directed to a focusing mirror which images the planes of the reference and return mirrors onto the film plane. The reference and focusing mirrors are adjusted so that localized fringes are created in their planes. The cavity windows are designed to withstand the hostile  $F_2$  environment and a differential pressure of 6 atm which is the largest chemical laser over pressure expected on the windows. All optical elements, except the expander lens, collimating mirrors, and focusing mirror, are near-diffraction limited with a two-pass system aberration of approximately one p-p vis fringe. The optical components are supported by pedestals directly mounted to the floor. Transverse spatial temperature variations, in the optical path external to the test section, are limited to  $\sim \pm 0.25^\circ\text{C}$  by the use of shrouds if necessary, so that the fringe distortion from two passes of the air optical path is 0.5 p-p vis fringes.

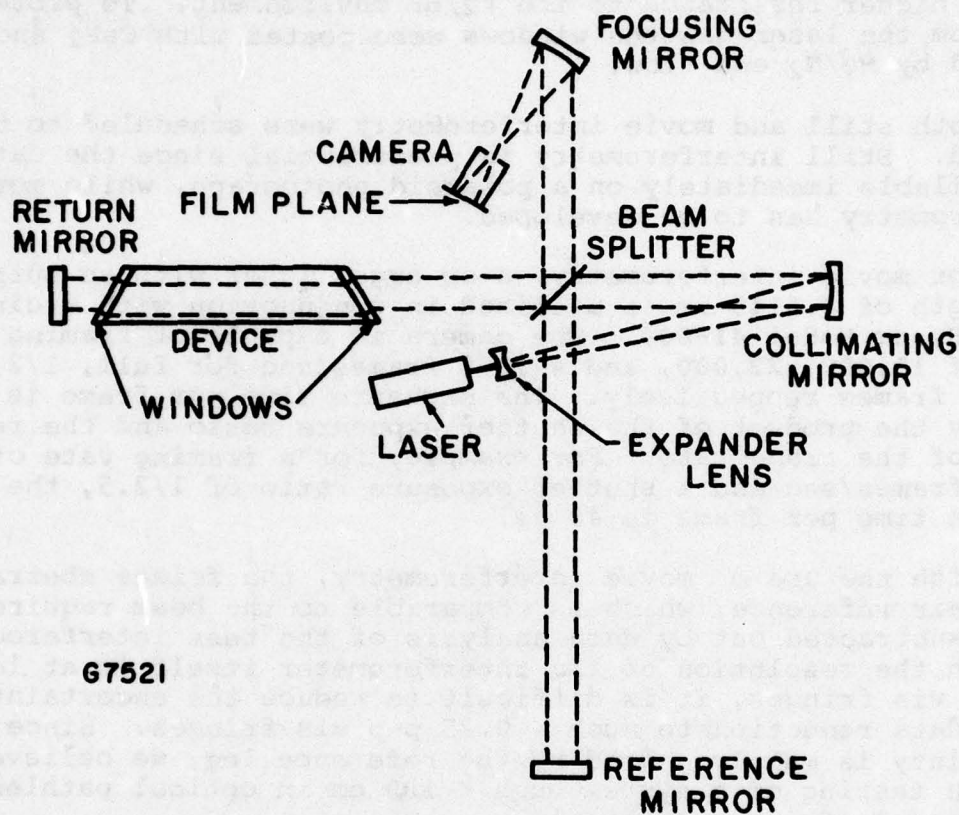


Figure 44 Schematic of Twyman-Green Interferometer



The film plane is placed at the image plane of the reference and return mirrors. All of the optics elements have a clear aperture of  $\sim 25$  cm in dia., which covers the  $15 \times 20$  cm clear opening of the windows. As windows, we used quartz. The selection of quartz over sapphire was based on cost and availability and its higher resistance to the  $F_2/HF$  environment. To protect them from the laser gas the windows were coated with  $CaF_2$  and isolated by  $He/N_2$  end flow.

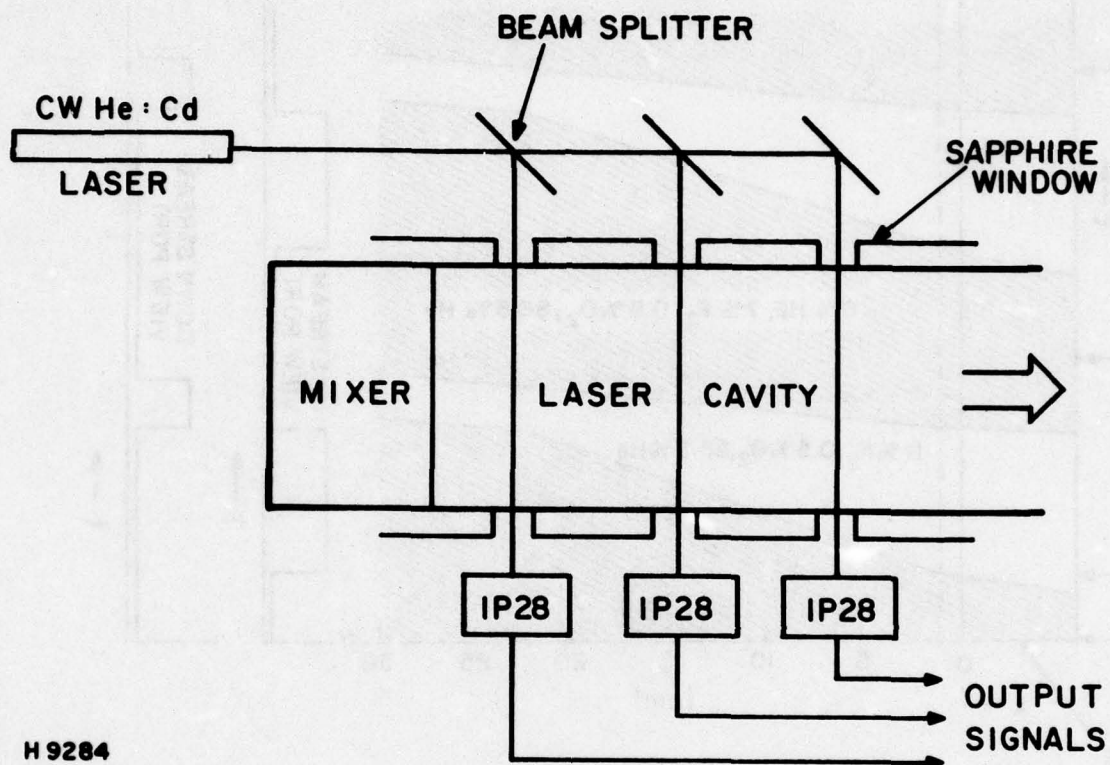
Both still and movie interferometry were scheduled to be employed. Still interferometry is preferential since the data are available immediately on a polaroid photograph, while movie interferometry has to be developed.

For movie interferometry, a cw argon laser with an output wavelength of  $0.5145 \mu m$  is utilized in conjunction with a cine camera Hycam Model 41-004. The camera is capable of framing rates of 11,000, 22,000, and 44,000 frames/sec for full,  $1/2$ , and  $1/4$  frames respectively. The exposure time per frame is given by the product of the shutter exposure ratio and the reciprocal of the frame rate. For example, for a framing rate of 10,000 frames/sec and a shutter exposure ratio of  $1/2.5$ , the exposure time per frame is  $40 \mu s$ .

With the use of movie interferometry, the fringe aberration of the air reference, which is comparable to the beam requirements, can be subtracted out by data analysis of the test interferograms. Although the resolution of the interferometer itself is at least  $0.1$  p-p vis fringes, it is difficult to reduce the uncertainties in the data reduction to much  $< 0.25$  p-p vis fringes. Since this uncertainty is mainly caused by the reference leg, we believe that the testing of a system much  $< 100$  cm in optical pathlength is not meaningful or practical.

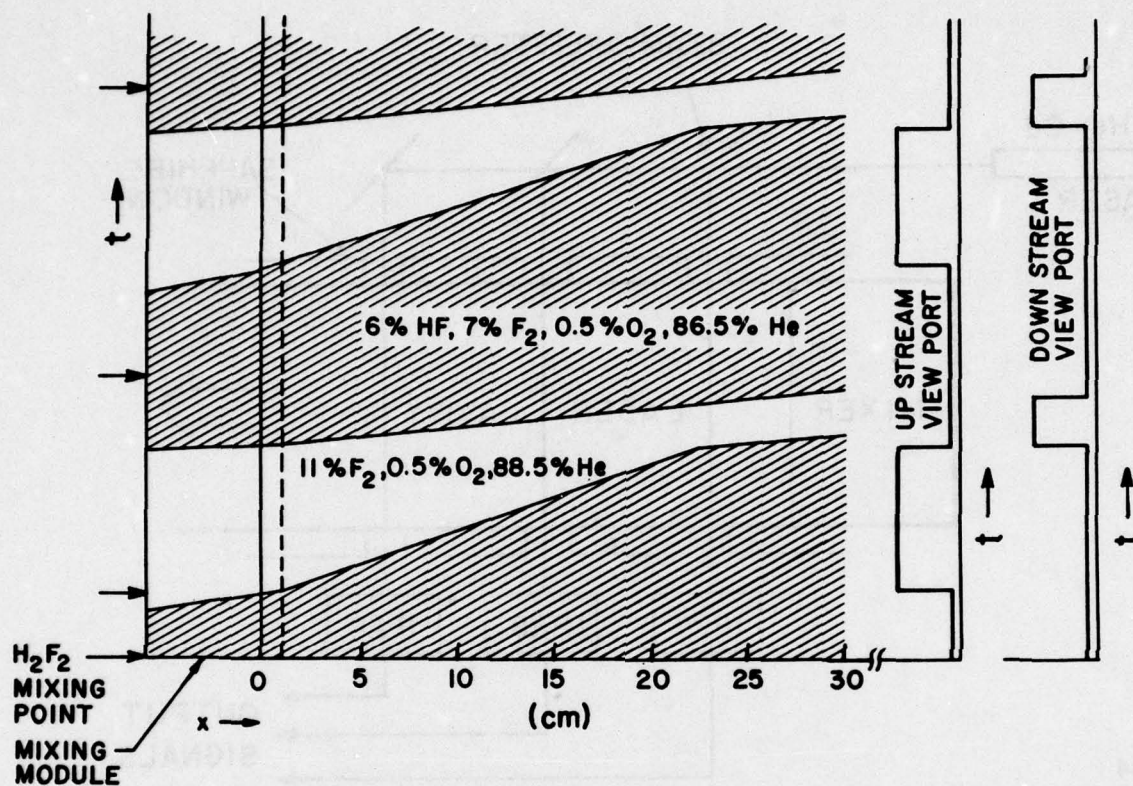
#### 14. FLAME-OUT DIAGNOSTICS

For the flame-out diagnostics,  $1.0$  MW cw feedback stabilized  $He:Cd$  laser operating at  $325$  nm is used. Figure 45 shows the schematics of the arrangement. One centimeter diameter windows, flush with the inside laser cavity surface, were employed. The transmitted light was passed through line filters and monitored by Type 1P28 photomultipliers. This technique allows determination of the  $H_2$  front arrival, since the  $F_2$  mixture is diluted by the  $H_2$  flow. Furthermore, a large and unambiguous change in the  $F_2$  results from combustion, while the remaining concentration is lowered by expansion as a result of heating. The subsequent test result shows the recorded signal for upstream and downstream observation positions. Figure 46 and Figure 47 shows the ideal X-T diagram and expected signal for both condition of flame-out and nonflame-out.



H 9284

Figure 45 Schematics of Flame-Out Diagnostics



65023

Figure 46 X-T Diagram with Flame Standing in the Mixing Module



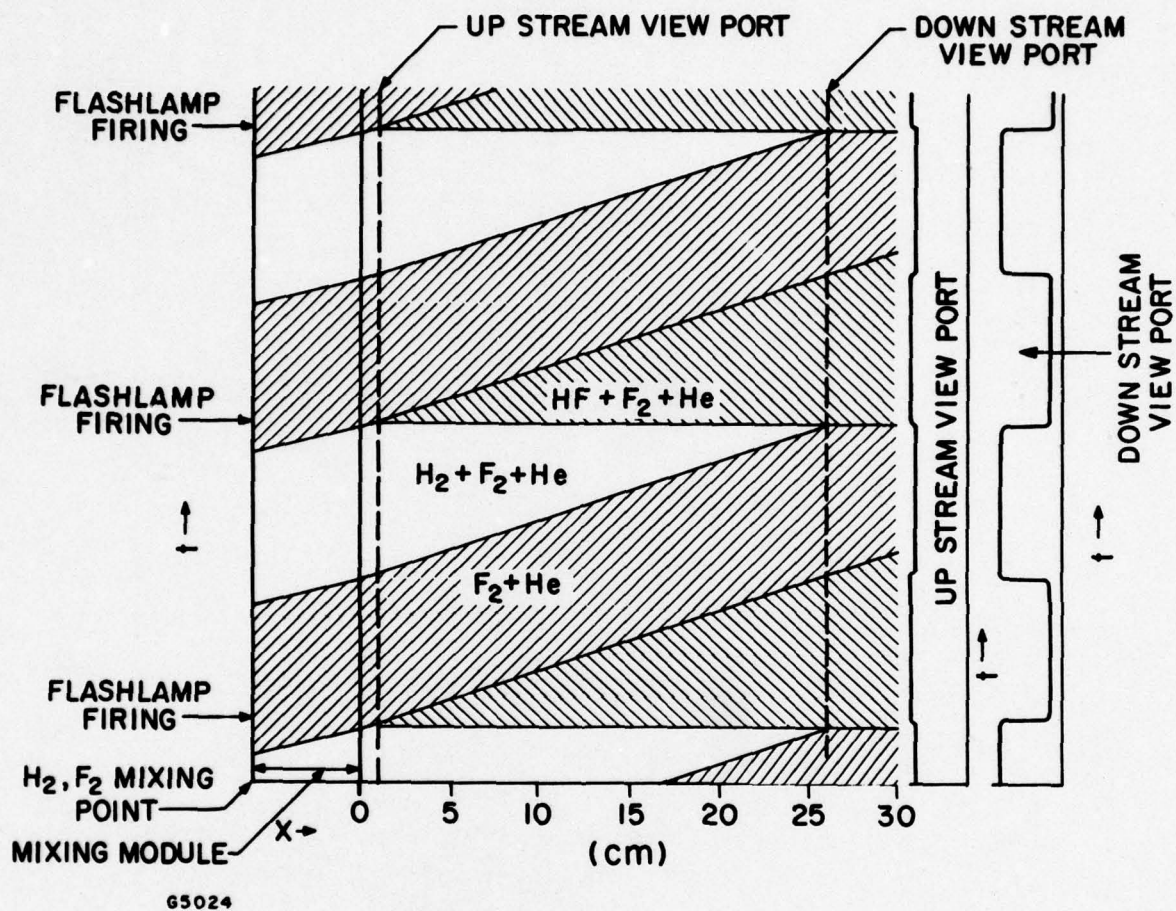


Figure 47 X-T Diagram for Flame-Out Condition

## VI. EXPERIMENTAL RESULTS

As pointed out earlier the design, testing and fabrication of the mixer took a considerable time. With the completion of the mixer a total period of six weeks remained to install the mixer and collect test data. The data given in this section identifies the requirements for adjustments and design modification. It does not reflect the performance this type of system may reach once modifications have been performed and the optimum operating parameters have been selected.

### 1. MIXER FLOW TESTS

In the earlier days of this program a small mixing module section was fabricated using conventional precision machining. Subsequent flow tests with optical interferometry on this unit indicated that the required flow uniformity may not be obtainable with standard machining. We therefore proceeded to redesign the mixer to adapt the design to the photochemical fabrication technique. Requirement for this mixer included a short mixing distance, a high flow uniformity at the injection point where the two principle gas mixtures meet and a small mixer scale size such that the wakes decay in a short distance. The reduction of the scale size will minimize the distance between the mixer exit and the active laser volume. After a significant development period the design and fabrication converged to the mixer described in Section V. We fabricated several sets of three mixing channels analyzed performance with a hot wire. Figure 48 shows hot wire scans taken downstream from and on the centerlane of the mix channel exit. The distance from the end of the mixer to the hot wire is given for each trace in millimeters. The hot wire was oriented parallel to the channel exit slit and operated in the constant temperature mode. The sensing element was a 2 mm long hot wire Type TSI 1210. The "constant temperature hot wire aerometer" was fabricated by Thermal System (TSI), Model No. 1150. For the above traces the system was operated in the non-linearized mode, since the linearization coefficients were not available for the mixtures being used. This mode of operation made the hot wire more sensitive to velocity variations since the recorded output signal is typically represented by  $\phi(V) = A_1V + A_2V^2 + A_3V^3 + A_4V^4 + \dots$  and the dominating terms is  $A_4V^4$ . The periodic dips in the recorded output are due to the wakes of the thirteen support islands in the mixing channel. The scan spans the cavity flow region. Wake decay can be identified in these traces. They indicate that at a distance of 3 cm from the mixer exit the wakes are dissipated. This was later verified by optical interferometry tests on the complete system.

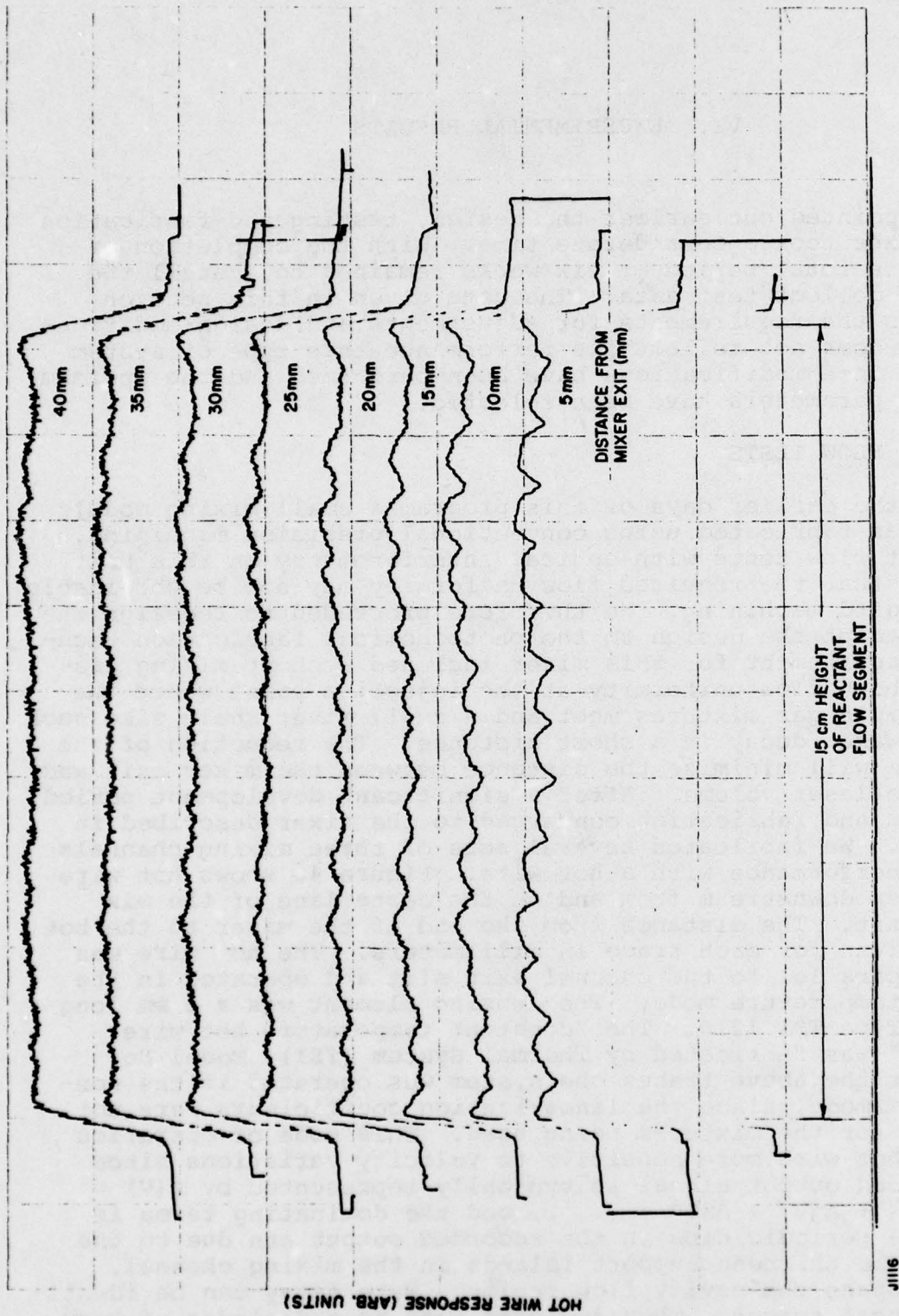


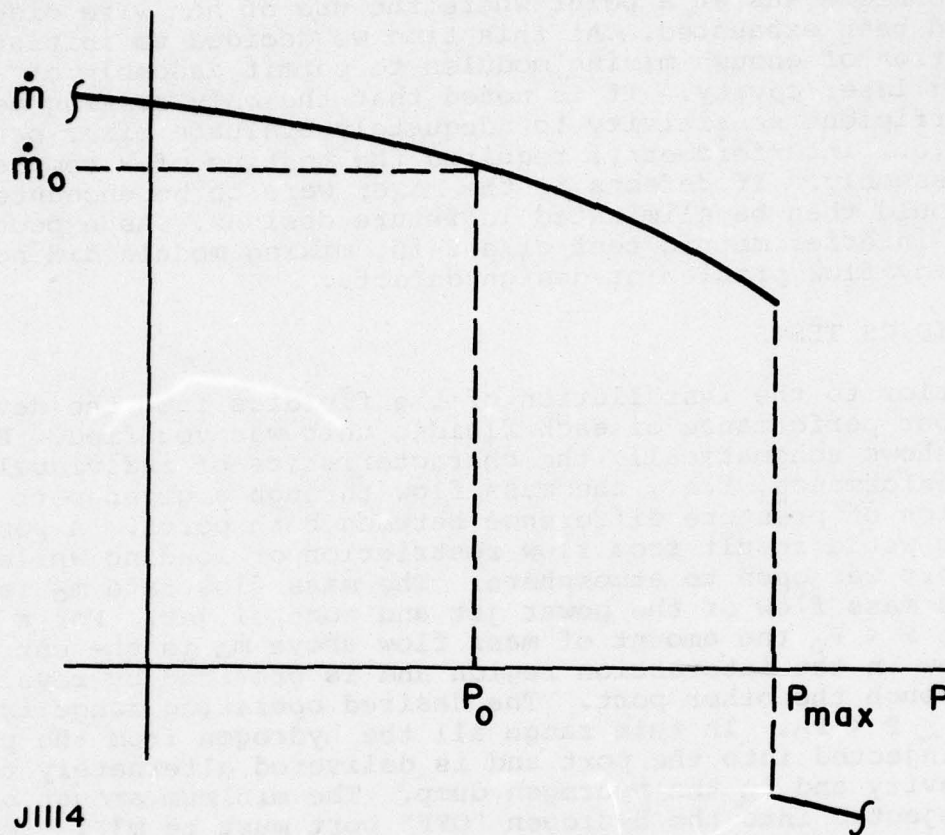
Figure 48 Hot Wire Diagnostics of Mixer



After hot wire tests of various mixing module subsections and on a 2-in. mixing module, it was concluded that the fabrication technique was at a point where the use of hot wire diagnostics had been exhausted. At this time we decided to initiate fabrication of enough mixing modules to permit assembly of a 1-m long laser cavity. It is noted that the only testing means with sufficient sensitivity to adequately evaluate mixer performance (i.e., interferometry) required the testing of a complete mixer assembly. If defects in the mixer were to be encountered these would then be eliminated in future designs. As expected, optical interferometric test of a 2-in. mixing module did not reveal any flow problem or design defects.

## 2. FLUIDICS TESTS

Prior to the installation of the fluidics into the device the proper performance of each fluidic unit was verified. Figure 49 shows schematically the characteristics of individual valve performance, i.e., the mass flow through a given port as a function of pressure difference between both ports. A positive pressure would result from flow restriction or loading while the other port was open to atmosphere. The mass flow rate  $\dot{m}_0$  is the combined mass flow of the power jet and control jet. For a backpressure  $P < P_0$  the amount of mass flow above  $\dot{m}_0$  is the entrained mass flow in the interaction region and is provided by reverse flow through the other port. The desired operating range is between  $0 \lesssim P < P_0$ . In this range all the hydrogen from the power jet is injected into the port and is delivered alternately to the laser cavity and to the hydrogen dump. The minimum amount of He to be injected into the hydrogen "OFF" port must be  $\dot{m}(P) - \dot{m}_0$ , where  $P$  is the backpressure operating point. We selected a helium OFF port injection which exceeded the maximum entrained mass flow of each fluidic unit. At a backpressure loading of  $P > P_0$  hydrogen is spilled over to the port which is not supposed to see hydrogen, while with a backpressure loading of  $P > P_{\max}$  the control jet flow becomes ineffective and the power jet detaches and reattaches on to the opposite wall. The characteristic curve (Figure 49) changes with both the power jet mass flow and the control jet mass flow. The tests of the fluidic units addressed certain features of the characteristic curves of specific interest where the dimensional settings in the interacting region. For this purpose it was important to compare  $P_{\max}$  of the ON port with that of the OFF port and to establish the value of  $P_0$ . In these measurements we connected one output port at a time to a closed container of volume  $V_0$  and measure the pressure rise as a function of time. Such traces are shown in Figure 50 where the performance of a complete fluidics pyramid with four hydrogen valves are shown. The minimum switching pressure  $P_{\max}$  of an accepted device was 7.5 psi. The performance range was from 7.5 psig to 12 psig. Both the ON port and OFF port performance is shown. The pressure



J1114

Figure 49 Schematic of Fluidics Device Characteristics



$P_0$  was obtained by switching the master fluidics such that the flow is deviated to the port not connected to the reservoir. This caused a "pump out" and these traces are also shown in Figure 50. The value of  $P_0$  fell in the range of 0.5 psi to 2 psi. To provide the correct operating pressure for the fluidics as installed in the system it was anticipated that it might be necessary to raise the OFF port operating pressure above atmosphere to compensate for the laser gas pressure drop through the mixer, laser cavity, acoustic absorber and scrubber. For this purpose a large accumulator with the correct initial pressure was installed into the hydrogen dump line with a valve to restrict the flow and increase the pressure. This gave the means of shifting the steady-state operating point of the fluidics by 2 psi to bring the steady-state pressure seen by the fluidics well within the fluidics spillover pressure loading of  $P_0$ .

The cause of the flameout difficulties covered in the next section may be illustrated in Figure 51 which records the pressure fluctuation in the hydrogen dump line plenum. This plenum receives through 80 (each 50 cm long and 0.5 in. in diameter) plastic lines, the hydrogen from the fluidics off ports. At this location a pressure variation of 3.5 psi occurs, whereas steady-state flow calculations predict a pressure rise of  $< 0.1$  psi. This transient flow condition both on the OFF port and on the ON port caused pressure differences across the fluidics substantially in excess of the design spillover pressure  $P_0 = 0.5$  to 2.0 psi. As soon as the backpressure exceeds  $P_0$ , as is evidenced from the pressure trace in Figure 51, hydrogen will spillover to the ON port during the OFF period and be injected into the laser cavity during the time when a hydrogen free slug of gas is required. The result is a mixer reignition. Some test evidence indicates that reignition does occur with a period of flow transit times from the fluidics to the mixer, with ignitions and overpressure occurring periodically and thus driving the process like an oscillator during the OFF period. This process of transient flow interacting with a high gain fluidics amplifier was not anticipated. At this point it is noteworthy to point out that the difference between the successful small scale device and this large scale system was the increased gain of the fluidics and certain details in the geometric configuration of the downstream components. At the time of this writing proposed modification to the system are under investigation. One modification would completely isolate the fluidics from its downstream environment. This applies for both the hydrogen dump flow and for the gas injected into the cavity.

### 3. FLAMEOUT TESTS

Following the completion of the mixing module fabrication and its installation, flow and flameout tests were performed. We selected initially a repetition rate of 30 pps and a hydrogen



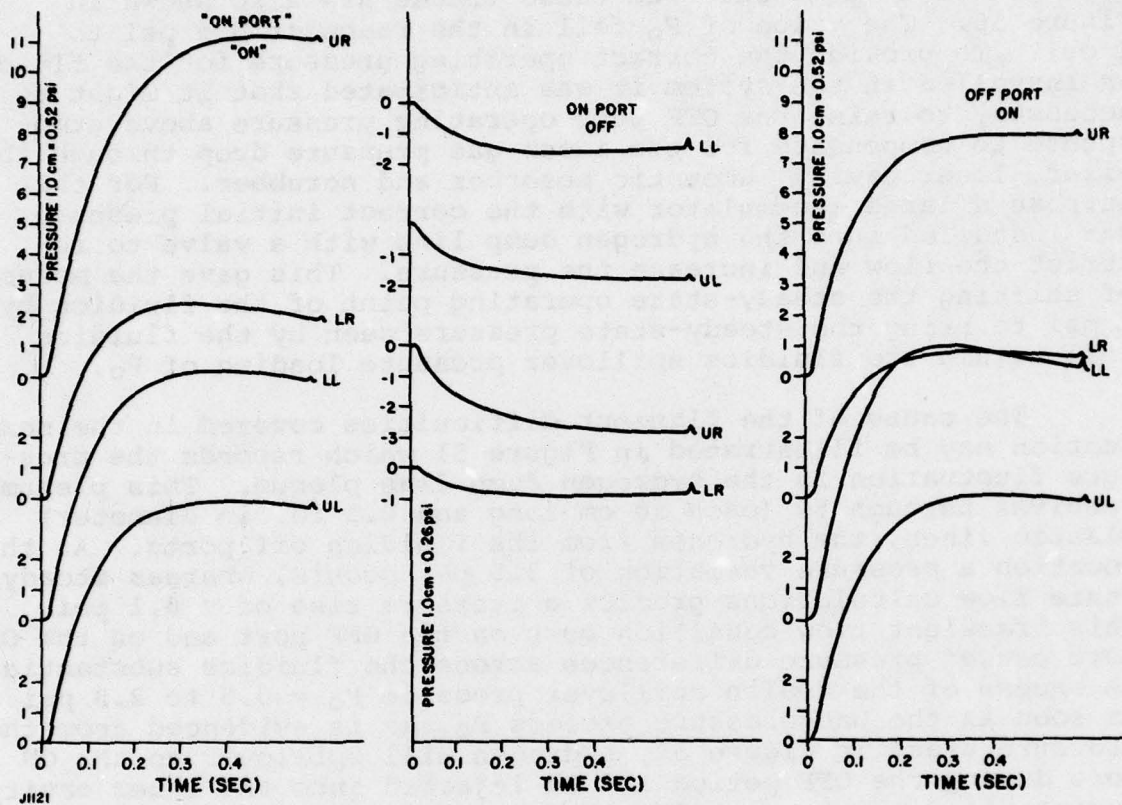


Figure 50 Fluidics Pressure Rise (Fall) vs time for Discharge (suction) to a Closed Volume

## H<sub>2</sub> DUMP LINE PRESSURE SIGNAL

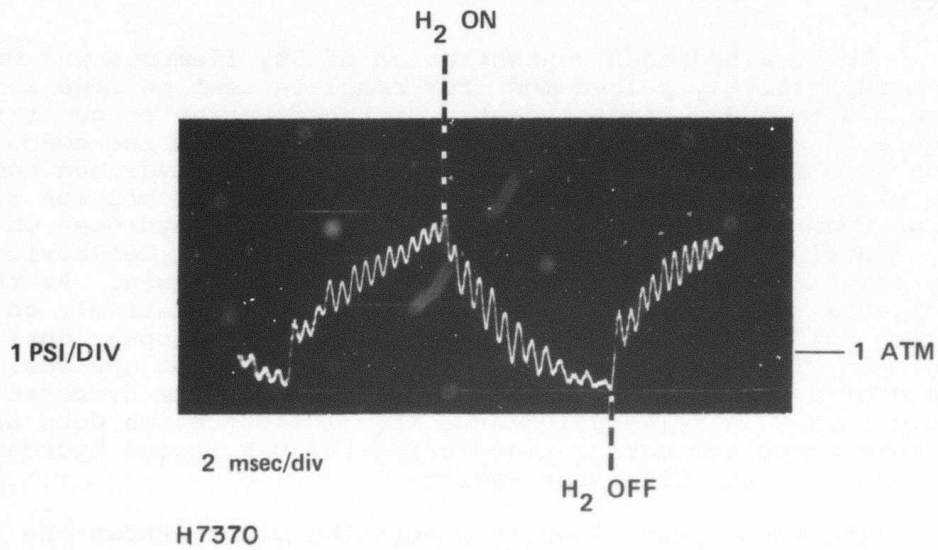


Figure 51 Hydrogen Dump Line Pressure vs Time

ON to OFF ratio of one to one. For this purpose the flow rates of all the gases were reduced by about a factor of two from that of the 60 pps design point with the exception of fluidics mass flow. Instead of a 100% hydrogen flow through the fluidics at half the volumetric flow we used a mixture of hydrogen/helium such that the Mach number through the fluidics remained about constant for optimum fluidics performance. Furthermore we used various mixtures of helium/hydrogen to operate for a given repetition rate with various hydrogen concentration in the laser cavity.

Up to a hydrogen concentration of 5%, flameout was obtained in a repetitively pulsed mode for complete test periods ranging from 0.5 to 1.0 s, independently of the fluorine concentration. Figure 52 shows the upstream and downstream fluorine concentration as a function of time for a mixture of 4% hydrogen and 10% fluorine. The upper trace shows the fluorine absorption 2.7 cm downstream from the exit of the mixer. In the hydrogen ON period, the fluorine absorption is less (negative signal deflection) since the constant fluorine flow is deluted with hydrogen. As the trace indicates the fluorine concentration remains relatively constant during this period. However, problems seem to appear during the hydrogen OFF period, when the signal is deflected upwards. Instead of a straightline, which indicates that the hydrogen flow would be OFF, a relatively large signal fluctuation does appear to take place indicating that during the OFF period hydrogen may be injected into the laser cavity.

The downstream fluorine absorption signal shows the large periodic deflection associated with the periodic combustion as expected. The downstream monitoring point is located 37 cm from the mixer exit.

With the hydrogen concentration increased to 8 percent, repeated preignition after the first initiation did occur as can be seen from the top trace in Figure 53 which is the upstream signal. Variation in the fluorine concentration in the range of 8 to 30 percent did not significantly effect the sensitivity of preignition. It was therefore necessary to diagnose the problem in order to perform modifications in the operating procedure or on the device to alleviate this problem.

A pressure transducer installed into the hydrogen dump line and laser cavity were used to monitor adjustments in the backpressure in the hydrogen dump line to the level of the cavity. The cause, in part, of the flameout problem has been related to the transient flow condition downstream of the fluidics OFF ports as illustrated in Figure 51. As can be seen the pressure fluctuation is about 3.5 psi peak to peak and exceeds the tolerable backpressure criteria of  $\approx 1.0$  psi. The large time dependent backpressure does cause hydrogen spillover to the ON port during



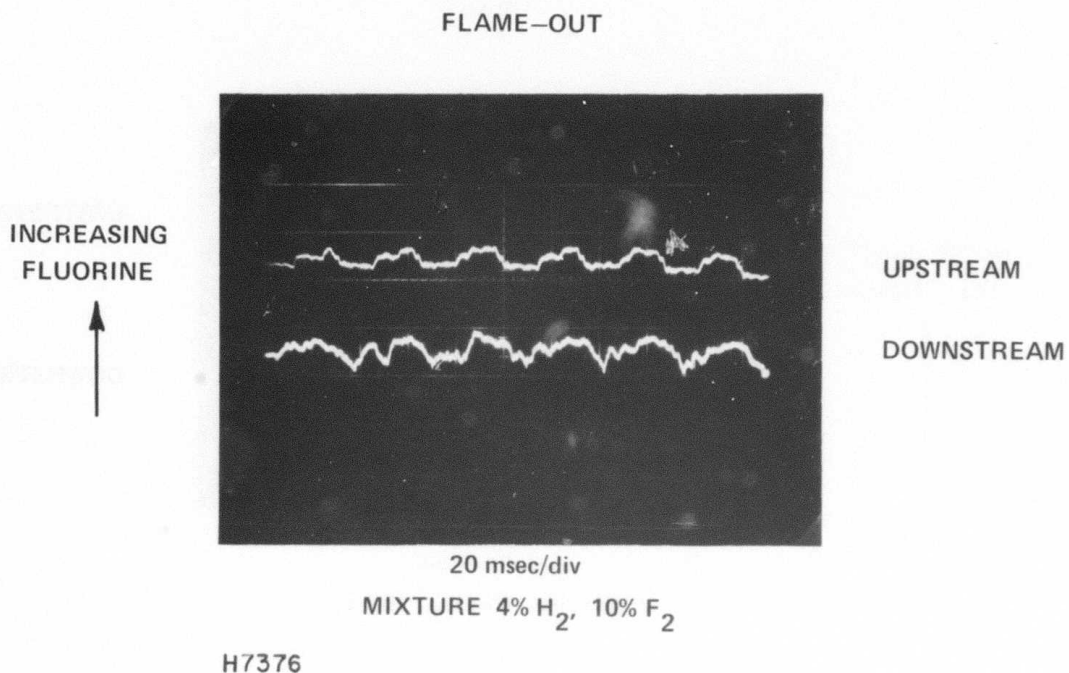


Figure 52 Fluorine Absorption Signals Indicating Successful Flame-Out

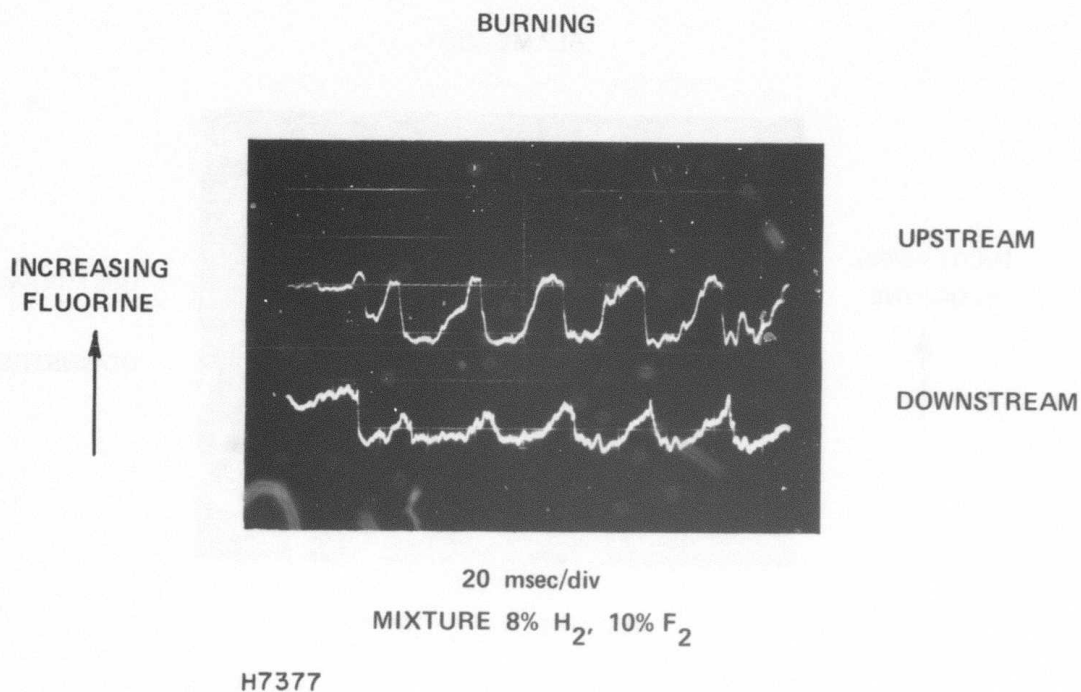


Figure 53 Fluorine Absorption Signals Indicating Pre-Ignition

the OFF period and therefore will result in flame-out problems. Detailed structure in both the laser cavity and hydrogen dump line pressure traces indicated pressure reflections of area discontinuities in both the dump lines and ON ports. Fine structure in the dump line traces are typically of the frequency associated with the round trip time through plastic tubing which connect the fluidics to the dump line plenum. Fine structure in the laser cavity traces seems to be related to the round trip time through the fluidics-mixer hydrogen path and is amplified by the energy release of chemical reaction. The investigation of the flame-out problem suggests that modifications are necessary and that close attention has to be given to the matching of impedance to both down stream ports of the transient hydrogen control device. Design efforts are now under way to correct these problems.

#### 4. ACOUSTIC DAMPING TEST

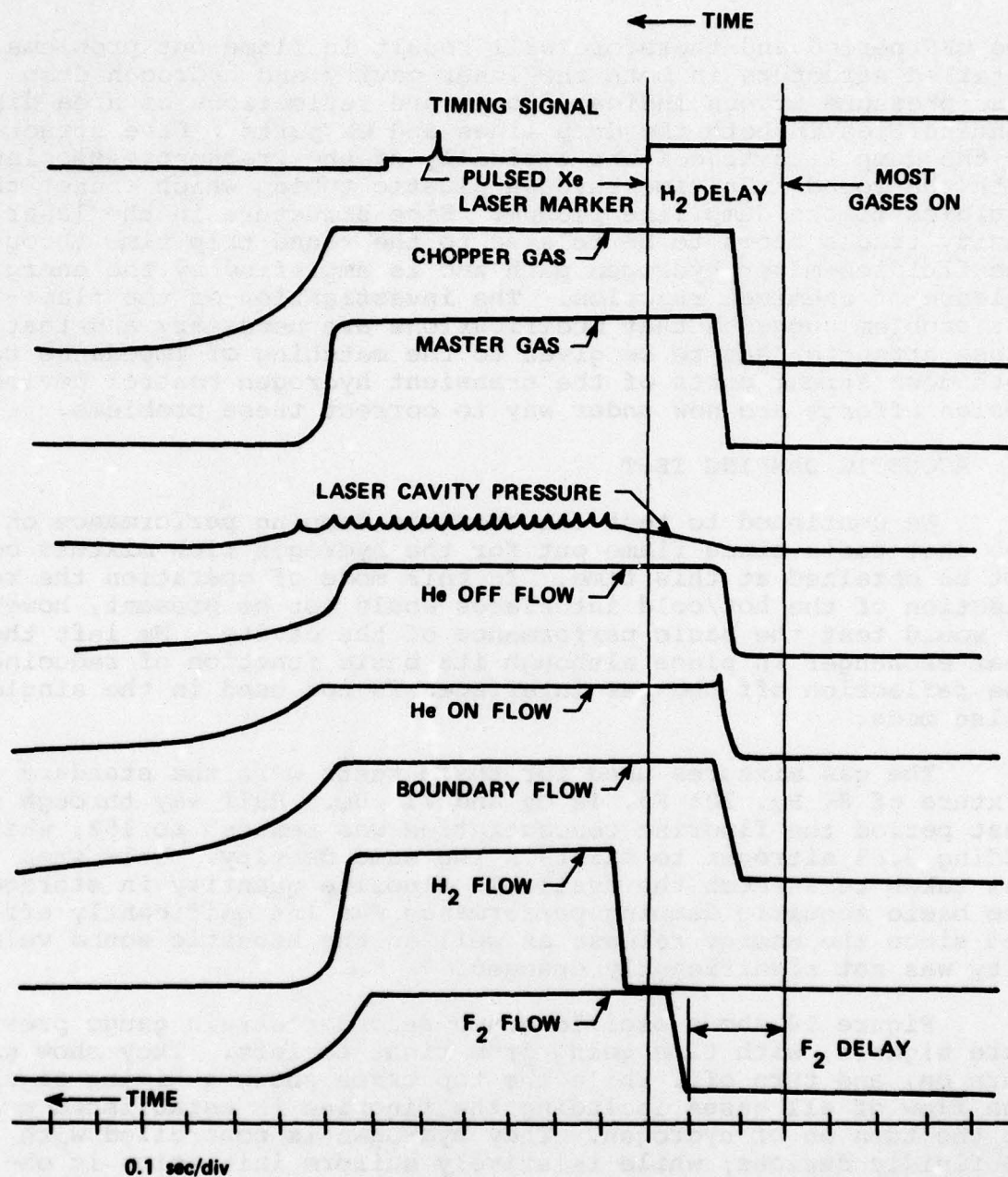
We continued to test the acoustic damping performance on a one shot basis since flame out for the hydrogen rich mixture could not be obtained at this time. In this mode of operation the reflection of the hot/cold interfaces would not be present, however, it would test the basic performance of the cavity. We left the heat exchanger in place although its basic function of reducing the reflection off the gas interfaces is not used in the single pulse mode.

The gas mixtures used for these tests were the standard mixture of 8% H<sub>2</sub>, 20% F<sub>2</sub>, 1% O<sub>2</sub> and 71% He. Half way through the test period the fluorine concentration was reduced to 15%, while adding 3.6% nitrogen to maintain the same density. This step was taken to stretch the available fluorine quantity in storage. The basic acoustic damping performance was insignificantly effected since the energy release as well as the acoustic sound velocity was not significantly changed.

Figure 54 shows oscillosgraph recorder strain gauge pressure signals, with time going from right to left. They show gas turn on, and turn off, while the top trace shows a timing signal. The flow of all gases including the fluorine is established prior to the turn on of hydrogen. The hydrogen is controlled with 80 fluidic devices; while relatively uniform initiation is obtained with flashlamps. High frequency piezoelectric pressure transducers served as the major diagnostics at this point and were recorded on oscilloscopes.

Such a recording is shown in Figure 55 where the pressure transducer was located in the central region of the laser cavity. Prior to this run room temperature nitrogen was used to fill the complete device downstream of the laser cavity. The pressure response to the initiation is qualitatively similar to the computer simulation of Figure 56, which does not include the presence of



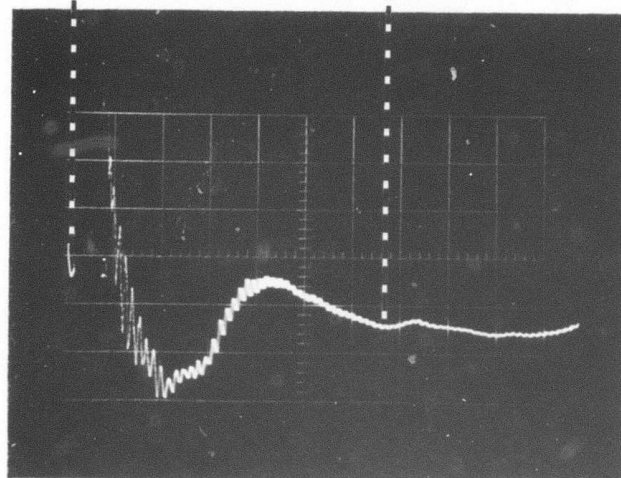


J1352

Figure 54 Oscillograph Record of System Pressures vs Time

FLASHLAMP TRIGGER

H<sub>2</sub> ON



2 msec/div

MIXTURE 8% H<sub>2</sub>, 20% F<sub>2</sub>

PRESSURE TRANSDUCES SIGNAL WITH NITROGEN  
DOWNSTREAM OF LASER CAVITY

H7367

Figure 55      Pressure Transduces Signal with Nitrogen Downstream  
of Laser Cavity

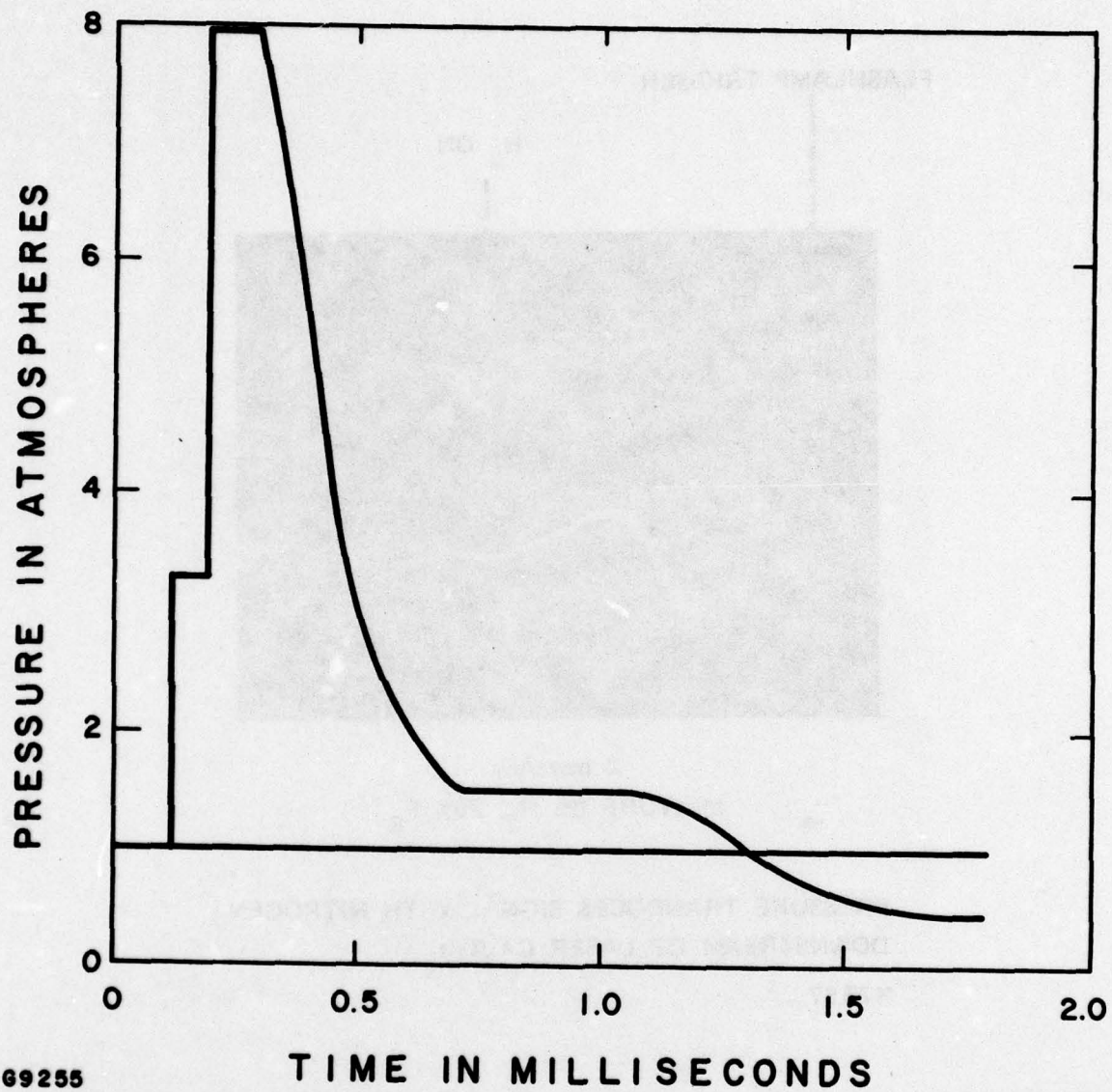


Figure 56 Computer Simulation of Cavity Pressure vs Time



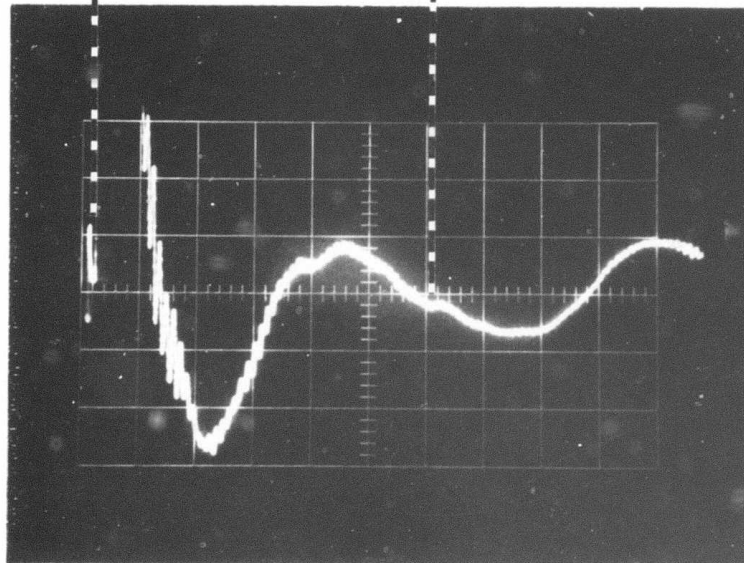
heat exchanger. In both cases the high overpressure is followed by an underpressure. However, the time of pressure undershoot is about 30% shorter in the computer simulation, and the simulation yields a greater negative pressure swing. We believe this is caused by the additional damping effect of the heat exchanger. To minimize the time for reducing the decay of the oscillation to a minimum pressure one must consider a trade off of various parameters. By increasing the resistance through the heat exchanger the undershoot may be reduced or in fact eliminated, however, the time for the initial pressure decay becomes longer. Reducing the amount of damping will reduce the time of the initial overpressure decay, however, at the expense of a greater undershoot. In any case, to find the optimum point of operation one must tune the system. Furthermore the testing must be performed in the repetitively pulsed mode in order to include the hot-cold gas interface reflection. The time remaining under this contract did not allow us to perform the necessary modifications and fully investigate this issue.

The acoustic damping performance may also vary as a function of the run duration, since the heat exchanger structure will increase in temperature as a function of operating time and the average gas temperature in the acoustic absorber will increase and shift the attenuation frequency spectrum of Figure 21. To test for the sensitivity of this effect helium was injected into the heat exchanger and acoustic absorber prior to the run instead of nitrogen. This is expected to shift the acoustic absorber spectrum to higher frequency, while reducing the effectiveness at the lower frequency end. The test result of this extreme measure is shown in Figure 57 which shows a greater undershoot and a longer ringing time. This data was included to illustrate that the hot gas downstream in the laser cavity will have a pronounced effect on the acoustic absorber operation. Although it is not expected that an accumulation of acoustic energy from previous pulses will occur in the pulse chemical laser, still, single pulse acoustic damping will not likely adequately simulate multiple pulse damping for long run durations. This would require a run duration where not only the acoustic velocity is correct, but also the structure such as the heat exchanger, acoustic absorber, etc. must reach the long run duration temperature, and it must include the presence of the hot-cold gas interfaces. It is anticipated that significantly more work is required to tune up the acoustic absorber system performance of a long duration pulsed chemical laser.

To put the preliminary test results of Figure 55 in the right perspective it must be pointed out that at the time of the maximum undershoot ( $\approx 1$  psi) the pressure disturbance remaining in the laser cavity is about one order of magnitude less than the initial overpressure in Humdinger. Since the acoustic quieting time of Humdinger was less than 2 msec, it can be assumed that not

FLASHLAMP TRIGGER

H<sub>2</sub> ON



2 msec/div

MIXTURE 8% H<sub>2</sub>, 20% F<sub>2</sub>

PRESSURE TRANSDUCES SIGNAL  
WITH HELIUM DOWNSTREAM  
OF LASER CAVITY

H7368

Figure 57 Pressure Transduces Signal with Helium Downstream  
of Laser Cavity

much more than an additional 2 msec must pass after this point before fresh gases can be injected into the cavity with adequate optical medium quality.

The smooth decay of the second overpressure suggests that with the use of a mirror tilt and a cylindrical lens the medium distortion can be nearly corrected. Higher order corrective terms may be implemented as fixed mirror corrections since the pressure pulses are repetitive in nature. However, future tests will show if shock wave reflections at the hot/cold gas interfaces are troublesome during late interpulse times. It is reasonable to assume that they are not, since two to three round trip periods will have passed prior to the next fluidics turn on.

The following data were collected using the double pass optical interferometer setup of Figure 37. These data were included to demonstrate the importance of index matched gas mixtures.

Figure 58 shows an interferogram of a 8%  $H_2$ , 10%  $F_2$ , 82% He mixture. The flow is from right to left. The fringes are setup in the vertical position. The calculated position of the hydrogen turn on point is indicated. This interferogram suggest several problems. The major issues are the four passes through the two shear layers (end flow - laser gas) and the importance of index matched gases. The following data were taken to locate the source of the problem such that corections could be performed.

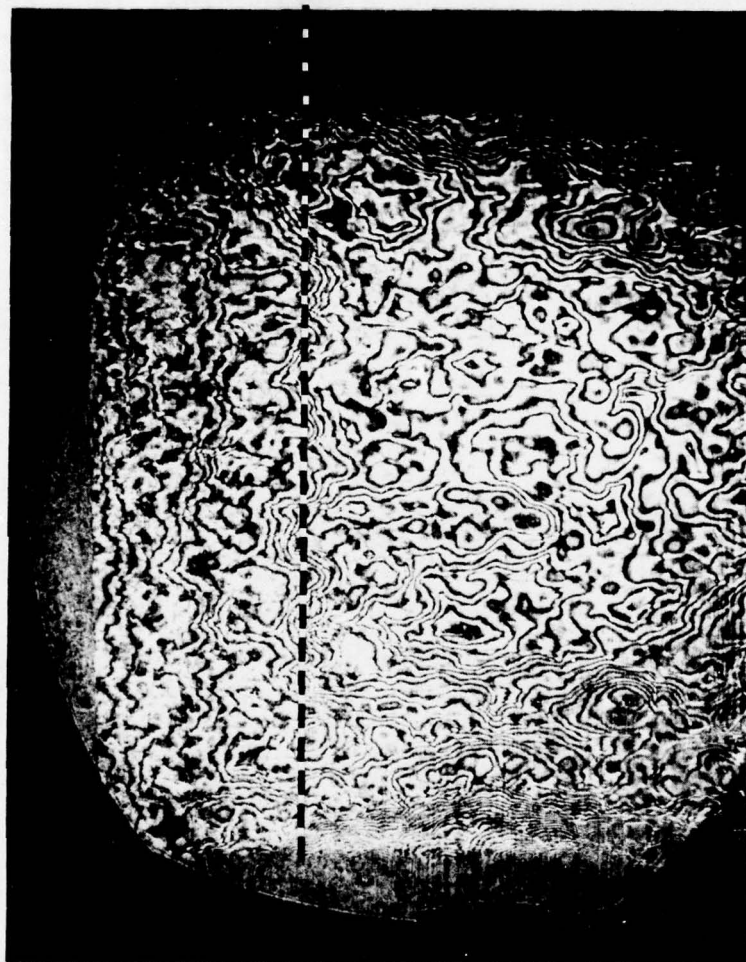
Figure 59 shows a test using He in the hydrogen mixture and  $N_2$  in the fluorine mixture. These gases and test conditions were used to exaggerate the index of refraction differences of the two main flows. For this mixture the Dale-Gladstone coefficient is  $1.68 \times 10^{-4}$  and an eleven fringe change would correspond to a 1% mixture concentration change in the laser cavity. This interferogram does indicate that the basic mixer performance is satisfactory. This figure also shows the boundary layer growth, since no attempt was made to index match the boundary gas.

To test the effect of the shear layers on medium quality He was used for the laser gas, while a mixture of 40%  $N_2$ , 60% He was used in both the end flows, 2nd the boundary flows. Figure 60 in the central region illustrates the effect of passing through four shear layers. In Figure 60 an attempt was made to get the velocity differences across the shear layers as low as possible. Finally in Figure 61 the main gas, end flow and boundary flow were index matched using a mixture of 50% He and 50%  $N_2$ . This procedure of premixing for index matched gases provides satisfactory, beam quality and it indicates the direction for future experiments.

Operation with index matched gases is possible over a wide range of fluorine mixtures. This can be seen from Figure 62 which gives the mole fraction of helium to be mixed with the hydrogen gas to yield 8%  $H_2$  over a wide range of fluorine concentration.



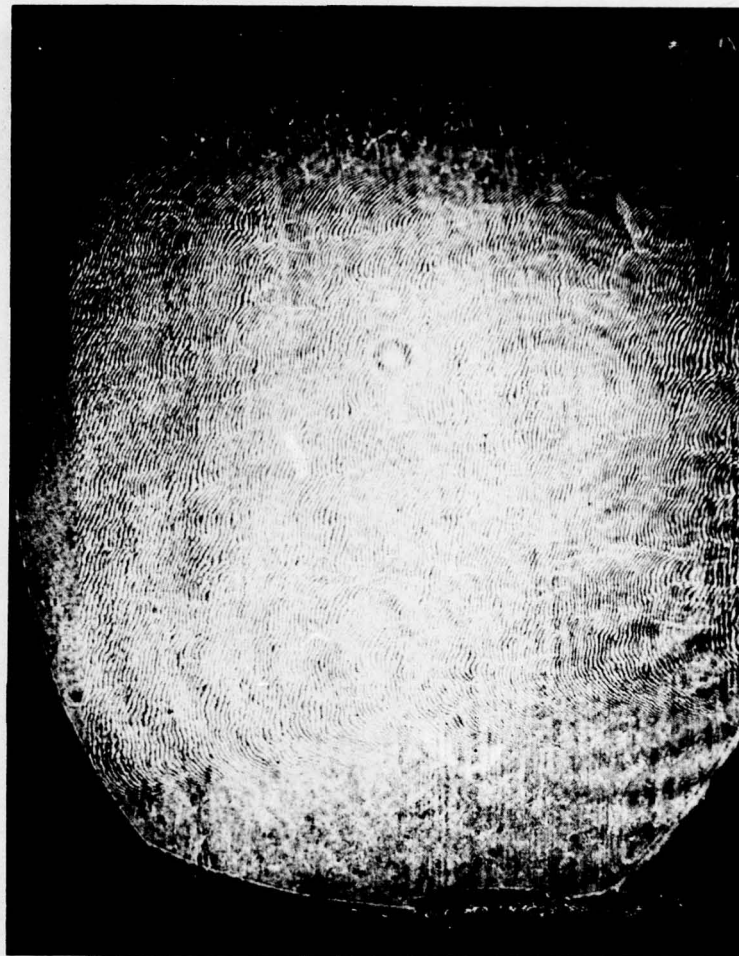
FLUIDICS TURN ON



FLOW WITH 8%  $H_2$ , 10%  $F_2$ , 82% He

H7369

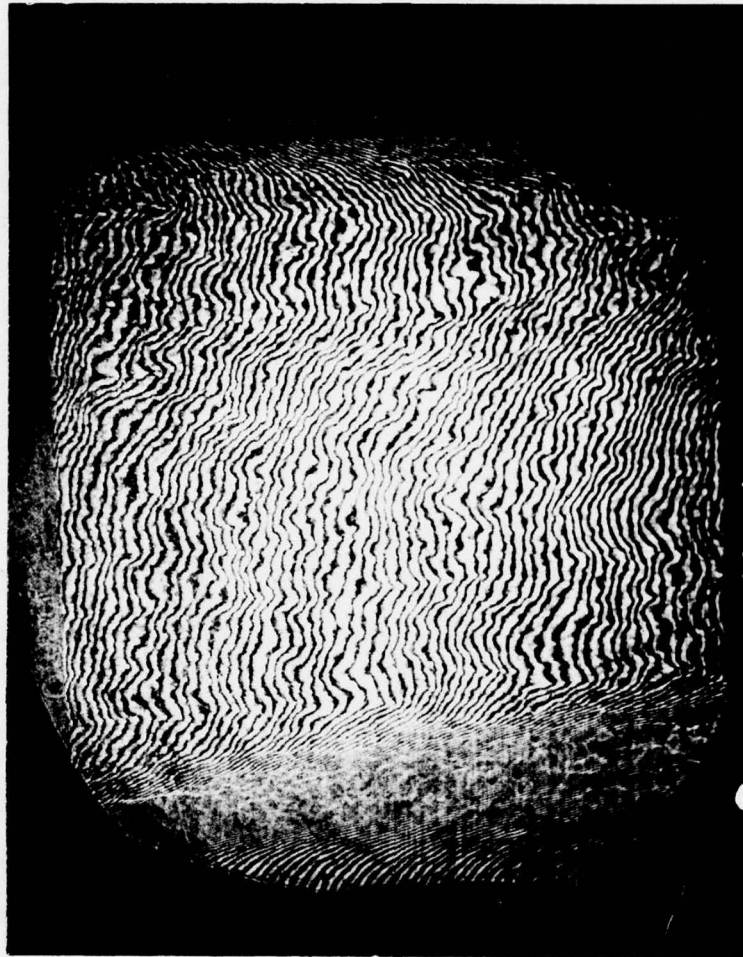
Figure 58      Flow with 8%  $H_2$ , 10%  $F_2$ , 82% He



FLOW TEST WITH He IN H<sub>2</sub> MIXTURE AND  
N<sub>2</sub> IN F<sub>2</sub> MIXTURE

H7374

Figure 59      Flow Test with He in H<sub>2</sub> Mixture and N<sub>2</sub> in F<sub>2</sub>  
Mixture

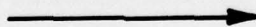
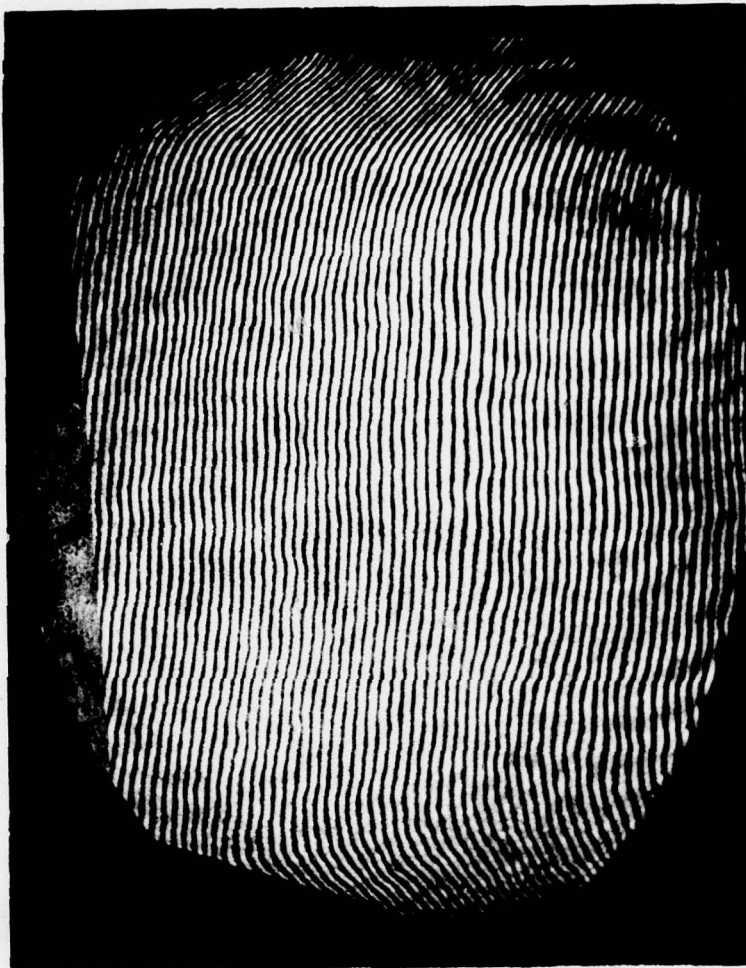


He IN F<sub>2</sub> AND H<sub>2</sub> MIX, 40% N<sub>2</sub>, 60% He MIX  
IN BOUNDARY AND END FLOW (SHOWS EFFECT  
OF END FLOW/MAIN GAS FLOW INTERFACE

H7373

Figure 60      He in F<sub>2</sub> and H<sub>2</sub> Mix, 40% N<sub>2</sub>, 60% He Mix in  
Boundary and End Flow (Shows Effect of End  
Flow/main Gas Flow Interface





FLOW WITH NEARLY MATCHED GASES

$V \approx 2 \times 10^3$  cm/sec

H7375

Figure 61 Flow with Nearly Index Matched Gases  $V \approx 2 \times 10^3$  cm/sec

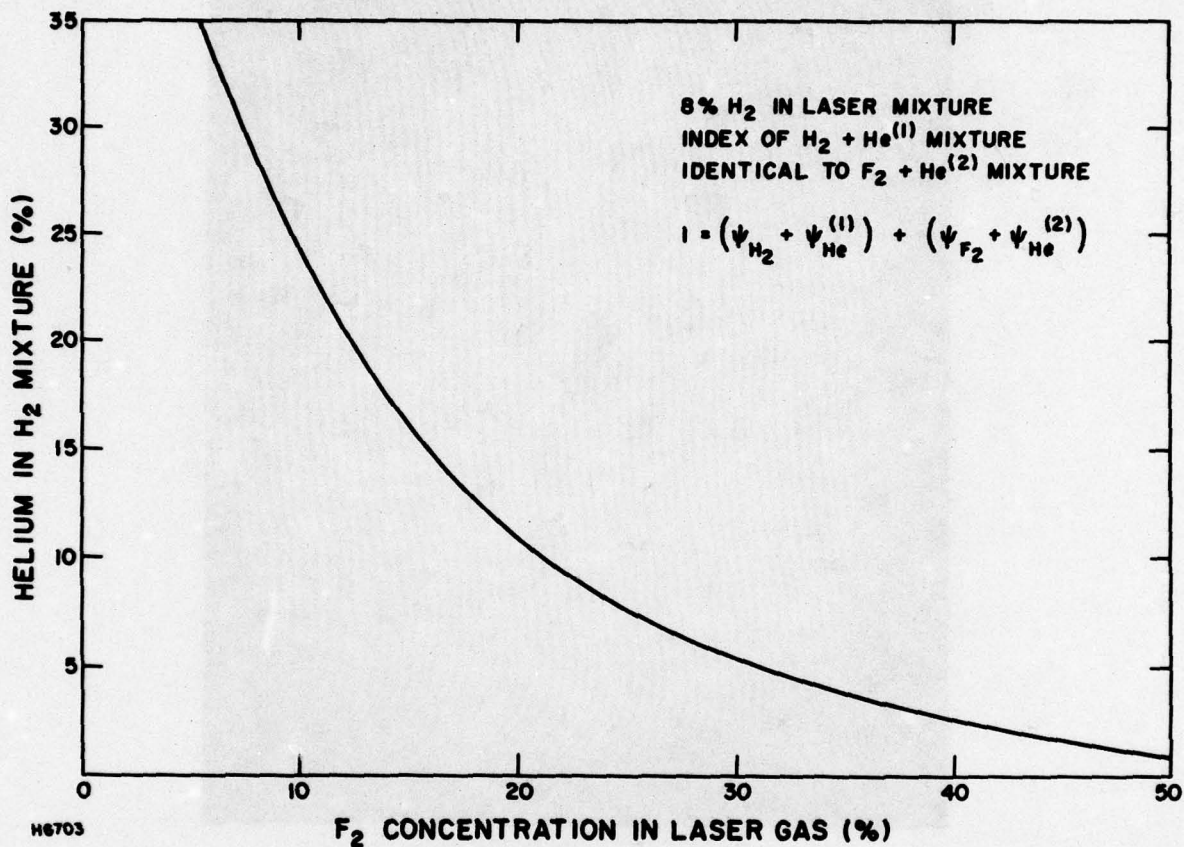


Figure 62 Fraction of He Cavity Gas in the H<sub>2</sub> + He Mixture Necessary to Match Index of Refraction of the F<sub>2</sub> + He Mixture

For instance, to obtain 8% H<sub>2</sub>, 20% F<sub>2</sub> 72% He mixture, the mole fraction of the hydrogen mixture would be about 20% having the composition of 8 parts H<sub>2</sub>, 12 parts He, while the fluorine mixture would have the composition of 20 parts F<sub>2</sub> and 60 parts He. This yields for both gases a Gladstone-Dale Coefficient of  $7.5 \times 10^{-5}$ . To match the index of refraction for both the end flow and boundary flow their mixture composition would have to be selected as 85% He, 15% N<sub>2</sub>. These numbers are consistent with the overall design concept of the pulse chemical laser. Premixing for purposes of index matching is possible with our system by operating with a He + H<sub>2</sub> mixture and F<sub>2</sub> + He mixture not equal in volumetric flow rate. Furthermore this modification is consistent with the second system modification which is required to make the hydrogen controlling fluidics completely insensitive to the pressure in the laser cavity.



## VII. CONCLUSION

The work performed under this contract was to address the remaining key technical issue of acoustic quieting for a repetitively pulsed chemical laser. For this purpose a 30 liter device, 100 cm in dimension parallel to the optical axis was constructed. The acoustic damping system consists of a heat exchanger and a muffler type absorber. A new mixer was developed using a photochemical machining technique. This mixer appears to work satisfactorily. A significant effort, cost and time had to be expended for its development. Some flame-out and acoustic damping data were collected during a six week testing period. Necessary modifications to both the fluidics system and the gas handling system were identified to insure flame-out for hydrogen rich mixtures and to provide adequate medium homogeneity for good optical beam quality. Limited acoustic damping measurements uncovered no major technological problem in obtaining the DOD objectives. However, further acoustic damping measurements are required after completion of necessary system modifications.

DISTRIBUTION LIST

Naval Research Laboratory, Code 5540, Washington, D.C. 20375 - Attn: Dr. S.K. Searles (5 copies)

Naval Sea Systems Command, PMS-405, Room 11N08, National Center #1, Washington, D.C. 20362 - Attn: Dr. D. Finkleman (1 copy)

Naval Sea Systems Command, PMS-405, Room 11N08, National Center #1, Washington, D.C. 20362 - Attn: Dr. J. Stregack (1 copy)

AFWL-ALC, Kirtland AFB, NM 87117 - Attn: Capt. Barry Crane (1 copy)

Aerospace Corporation, P.O. Box 92957, Los Angeles, CA 90009 - Attn: Dr. Walter R. Warren (1 copy)

Aerospace Corporation, P.O. Box 92957, Los Angeles, CA 90009 - Attn: Dr. Robert Hofland (1 copy)

Commanding General, U.S. Army Missile Command, DRSMI-RHAD, Redstone Arsenal, AL 35809 - Attn: Dr. Charles Cason (1 copy)

Avco Everett Research Laboratory, 2385 Revere Beach Parkway, Everett, MA 02149 - Attn: Dr. Jack Daugherty (1 copy)  
Dr. R. Limpaecher (1 copy)

TRW Systems Group Inc., One Space Park, Redondo Beach, CA, Attn: Dr. Joseph Miller (1 copy)  
Mr. R. Aprahamian (1 copy)

Boeing Aerospace Corp., P.O. Box 3999, Seattle, WA 98124 - Attn: Dr. Doyle McClure (1 copy)

Mathematical Sciences Northwest, P.O. Box 1887, Bellevue, WA 98009 - Attn: Dr. Phil Cassidy (1 copy)

Hughes Research Laboratories, 3011 Malibu Canyon Road, Malibu, CA 90265 - Attn: Dr. Gary Janney (1 copy)

United Technologies Research Laboratory, 400 Main Street, East Hartford, CT 06108 - Attn: Dr. Albert W. Angelback (1 copy)

Sandia Laboratories, P.O. Box 5800, Albuquerque, NM 87115 - Attn: Dr. J. Gerardo (1 copy)

Physical Sciences Inc., 30 Commerce Way, Woburn, MA 01801 - Attn: Dr. Raymond Taylor (1 copy)

McDonnell-Douglas Research Laboratories, Department 220, Box 516, St. Louis, MO 63166 - Attn: Dr. D.P. Ames (1 copy)

Aerodyne Research, Inc., Bedford Research Park, Crosby Drive, Bedford, MA 01730 - Attn: Dr. M. Camac (1 copy)

DODAAD 547031, Bldg. 5, Cameron Station, Alexandria, VA 22314 - Attn: Defense Documentation Center (12 copies)

Naval Research Laboratory, Code 5503, Washington, D.C. 20375 (1 copy)

Naval Research Laboratory, Code 5506, Washington, D.C. 20375 (2 copies)

Naval Research Laboratory, Code 1409, Washington, D.C. 20375 - Attn: Dr. John Kershenstein (1 copy)  
Dr. John MacCallum, Jr. (1 copy)

Rockwell International, Rocketdyne Division, 6633 Canoga Avenue, Canoga Park, CA 91304 - Attn: Dr. William Moyer (1 copy)

Garrett/AiResearch, Division 93-6 (T-42), 2525 W. 190 Street, Torrance, CA 90509 - Attn: Dr. Richard G. Miller (1 copy)

Los Alamos Scientific Laboratory, P.O. Box 1663, Los Alamos, NM 87544 - Attn: Dr. George Emanuel (1 copy)

Physics International, 2700 Merced Street, San Leandro, CA 94577 - Attn: Dr. Mark Kolpin (1 copy)

Air Force Weapons Laboratory, Kirtland Air Force Base, Albuquerque, NM 87117 - Attn: Dr. P.J. Ortwerth (1 copy)

W.J. Schafer Associates, 1901 N. Fort Myer Drive, Suite 800, Arlington, VA 22209 - Attn: Dr. Jack Hammond (1 copy)

Naval Research Laboratory, Code 6330, Washington, D.C. 20375 - Attn: Dr. J.T. Schriempf (1 copy)

Naval Research Laboratory, Code 5560, Washington, D.C. 20375 - Attn: Dr. P.B. Ulrich (1 copy)

Science Applications, Inc., 8th Floor, 2361 South Jefferson Davis Highway, Arlington, VA 22202 - Attn: Dr. Alan Phillips (1 copy)